



HAL
open science

The statistical model for unpolarized and polarized parton distributions and fragmentations: a comparison with experiments

Claude Bourrely, Franco Buccella, Jacques Soffer

► **To cite this version:**

Claude Bourrely, Franco Buccella, Jacques Soffer. The statistical model for unpolarized and polarized parton distributions and fragmentations: a comparison with experiments. 2008. hal-00267014

HAL Id: hal-00267014

<https://hal.science/hal-00267014>

Submitted on 26 Mar 2008

HAL is a multi-disciplinary open access archive for the deposit and dissemination of scientific research documents, whether they are published or not. The documents may come from teaching and research institutions in France or abroad, or from public or private research centers.

L'archive ouverte pluridisciplinaire **HAL**, est destinée au dépôt et à la diffusion de documents scientifiques de niveau recherche, publiés ou non, émanant des établissements d'enseignement et de recherche français ou étrangers, des laboratoires publics ou privés.

THE STATISTICAL MODEL FOR UNPOLARIZED AND POLARIZED PARTON DISTRIBUTIONS AND FRAGMENTATIONS: A COMPARISON WITH EXPERIMENTS

C. BOURRELY¹, F BUCCELLA² and J. SOFFER³

¹Centre de Physique Théorique (UMR 6207)¹,
CNRS Luminy case 907,
13288 Marseille cedex 9, France

²Dipartimento di Scienze Fisiche, Università di Napoli,
Via Cintia, I-80126, Napoli, Italy
INFN, Sezione di Napoli

³Department of Physics, Temple University,
Philadelphia, Pennsylvania 19122-6082, USA

Updated March 2008

Abstract

In the framework of the statistical model for parton distributions and fragmentation functions we present a comparison of the model with a large set of unpolarized and polarized experimental data, the agreement with data supports our approach.

CPT-2003/P.4561
bourrely@cpt.univ-mrs.fr
jsoffer@temple.edu

¹UMR 6207 is Unité Mixte de Recherche du CNRS and of Universités Aix-Marseille I and Aix-Marseille II and of Université du Sud Toulon-Var, laboratoire affilié à la FRU-MAM.

Contents

1	<u>Polarized Parton Distributions</u>	2
1.1	<u>Quarks</u>	2
1.2	<u>Antiquarks</u>	3
1.3	<u>Gluon</u>	4
2	<u>Parton Fragmentation Functions</u>	5
3	<u>Parton distributions and fragmentation functions</u> <u>figures</u>	7
4	<u>Unpolarized experiments</u>	42
5	<u>Polarized experiments</u>	99
	References	132
	List of figures	148

1 Polarized Parton Distributions

We give a brief review of the parton distributions functions which are described in Refs. [1-6].

1.1 Quarks

The density functions are given by ² :

$$xu^+(x) = \frac{AX_{0u}^+x^b}{\exp[(x - X_{0u}^+)/\bar{x}] + 1} + \frac{\tilde{A}x^{\tilde{b}}}{\exp[\frac{x}{\bar{x}}] + 1} \quad (1)$$

$$xu^-(x) = \frac{AX_{0u}^-x^b}{\exp[(x - X_{0u}^-)/\bar{x}] + 1} + \frac{\tilde{A}x^{\tilde{b}}}{\exp[\frac{x}{\bar{x}}] + 1} \quad (2)$$

$$xd^+(x) = \frac{AX_{0d}^+x^b}{\exp[(x - X_{0d}^+)/\bar{x}] + 1} + \frac{\tilde{A}x^{\tilde{b}}}{\exp[\frac{x}{\bar{x}}] + 1} \quad (3)$$

$$xd^-(x) = \frac{AX_{0d}^-x^b}{\exp[(x - X_{0d}^-)/\bar{x}] + 1} + \frac{\tilde{A}x^{\tilde{b}}}{\exp[\frac{x}{\bar{x}}] + 1} \quad (4)$$

$$A = 1.74938 \quad (5)$$

$$b = 0.40962 \pm 0.00438^{(*)} \quad (6)$$

$$\bar{x} = 0.09907 \pm 0.00110^{(*)} \quad (7)$$

$$X_{0u}^+ = 0.46128 \pm 0.00338^{(*)} \quad (8)$$

$$X_{0u}^- = 0.29766 \pm 0.00303^{(*)} \quad (9)$$

$$X_{0d}^+ = 0.22775 \pm 0.00294^{(*)} \quad (10)$$

$$X_{0d}^- = 0.30174 \pm 0.00239^{(*)} \quad (11)$$

$$\tilde{A} = 0.08318 \pm 0.00157 \quad (12)$$

$$\tilde{b} = -0.25347 \pm 0.00318^{(*)} \quad (13)$$

note:

The temperature \bar{x} is identical for quarks, antiquarks and gluons.

²Values marked with an asterisk are free parameters of the model. The input scale is $Q_0^2 = 4\text{GeV}^2$, and $\Lambda(\overline{MS}) = 300\text{MeV}$. The evolution is performed at NLO.

1.2 Antiquarks

The density functions are given by:

$$x\bar{u}^+(x) = \frac{\bar{A}}{X_{0u}^-} \cdot \frac{x^{\bar{b}}}{\exp[(x + X_{0u}^-)/\bar{x}] + 1} + \frac{\tilde{A}x^{\bar{b}}}{\exp[\frac{x}{\bar{x}}] + 1} \quad (14)$$

$$x\bar{u}^-(x) = \frac{\bar{A}}{X_{0u}^+} \cdot \frac{x^{\bar{b}}}{\exp[(x + X_{0u}^+)/\bar{x}] + 1} + \frac{\tilde{A}x^{\bar{b}}}{\exp[\frac{x}{\bar{x}}] + 1} \quad (15)$$

$$x\bar{d}^+(x) = \frac{\bar{A}}{X_{0d}^-} \cdot \frac{x^{\bar{b}}}{\exp[(x + X_{0d}^-)/\bar{x}] + 1} + \frac{\tilde{A}x^{\bar{b}}}{\exp[\frac{x}{\bar{x}}] + 1} \quad (16)$$

$$x\bar{d}^-(x) = \frac{\bar{A}}{X_{0d}^+} \cdot \frac{x^{\bar{b}}}{\exp[(x + X_{0d}^+)/\bar{x}] + 1} + \frac{\tilde{A}x^{\bar{b}}}{\exp[\frac{x}{\bar{x}}] + 1} \quad (17)$$

$$\bar{A} = 1.90801 \pm 0.12627^{(*)} \quad (18)$$

$$\bar{b} = 2b = 0.81924 \quad (19)$$

$$xs(x) = x\bar{s}(x) = \frac{1}{4}(x\bar{u}(x) + x\bar{d}(x))$$

$x\Delta s(x) = x\Delta\bar{s}(x) = \frac{1}{3}(x\Delta\bar{d}(x) - x\Delta\bar{u}(x))$. This assumption was removed in a new version of the model, see [6].

$$xs^h(x, Q_0^2) = \frac{AX_{0u}^+x^{b_s}}{\exp[(x - X_{0s}^h)/\bar{x}] + 1} \frac{\ln(1 + \exp[kX_{0s}^h/\bar{x}])}{\ln(1 + \exp[kX_{0u}^+/\bar{x}])} + \frac{\tilde{A}_s x^{\bar{b}}}{\exp(x/\bar{x}) + 1}, \quad (20)$$

$$x\bar{s}^h(x, Q_0^2) = \frac{\bar{A}(X_{0d}^+)^{-1}x^{2b_s}}{\exp[(x + X_{0s}^{-h})/\bar{x}] + 1} \frac{\ln(1 + \exp[-kX_{0s}^{-h}/\bar{x}])}{\ln(1 + \exp[-kX_{0d}^+/\bar{x}])} + \frac{\tilde{A}_s x^{\bar{b}}}{\exp(x/\bar{x}) + 1}. \quad (21)$$

$$\begin{aligned} A &= 1.74938, \quad \bar{A} = 1.90801, \quad X_{0u}^+ = 0.46128, \quad X_{0d}^+ = 0.22775, \\ \bar{x} &= 0.09907, \quad \tilde{b} = -0.25347, \quad k = 1.42. \end{aligned} \quad (22)$$

1.3 Gluon

$$xG(x) = \frac{A_G x^{b_G}}{\exp[x/\bar{x}] - 1} \quad (23)$$

$$A_G = 14.27535 \quad (24)$$

$$b_G = 1 + \tilde{b} = 0.74653 \quad (25)$$

$$x\Delta G(x) = 0 \quad \text{at } Q_0^2 = 4\text{GeV}^2 \quad (26)$$

Charm

The charm is set to 0 at $Q_0^2 = 4\text{GeV}^2$

2 Parton Fragmentation Functions

We propose to parametrize the fragmentation functions of the baryons octet with a statistical model as in the case of PDF.

For the quarks $q = u, s, d$ the FF are expressed as

$$D_q^B(x, Q_0^2) = \frac{A_q^B X_q^B x^b}{\exp[(x - X_q^B)/\bar{x}] + 1}, \quad (27)$$

where X_q^B is the potential corresponding to the fragmentation $q \rightarrow B$ and Q_0^2 is an initial scale, given below in Table 1. We will ignore the antiquark FF $D_{\bar{q}}^B$, which are considered to be strongly suppressed. The heavy quark FF $D_Q^B(x, Q_0^2)$ for $Q = c, b, t$, which are expected to be large only in the small x region ($x \leq 0.1$ or so), are parametrized by a diffractive term with a vanishing potential

$$D_Q^B(x, Q_0^2) = \frac{\tilde{A}_Q^B x^{\tilde{b}}}{\exp(x/\bar{x}) + 1}. \quad (28)$$

The initial scale Q_0^2 , which is flavor dependent in this case, is given below in Table 1³. This FF for $Q \rightarrow B$ depends on \tilde{b} and a normalization constant \tilde{A}_B^Q for each baryon B . For the other quarks, we make some reasonable assumptions in order to reduce the number of parameters in addition to b , the universal power of x in Eq. (27). First we have the obvious constraints, namely, $D_u^B = D_d^B$ for $B = p, \Lambda$. Moreover we assume that we need only *four* potentials, two for the proton $X_u^p = X_d^p$ and X_s^p and two for the hyperons $X_u^Y = X_d^Y$ and X_s^Y where $Y = \Lambda, \Sigma^\pm, \Xi^-$. Finally for the gluon to baryon FF $D_g^B(x, Q^2)$, which is hard to determine precisely, we take a Bose-Einstein expression with a vanishing potential

$$D_g^B(x, Q_0^2) = \frac{A_g^B x^{\tilde{b}+1}}{\exp(x/\bar{x}) - 1}. \quad (29)$$

We assume it has the same small x behavior as the heavy quarks and it is the same for all baryons. The normalization constants A_q^B , A_g^B and \tilde{A}_Q^B are determined by fitting the data.

³Due to the fact that the input scale of the t quark is above the highest energy data investigated in this work, it does not contribute to our analysis.

Table 1: Input scales Q_0 and $\Lambda(\overline{MS})$ in GeV unit.

quark	u,d,s	c	b	t
Q_0	0.632	1.4	4.5	175
$\Lambda(\overline{MS})$	0.299	0.246	0.168	0.068

Now, let us report the values of the free parameters we have obtained from the NLO fit:

$$\begin{aligned}
 X_u^p = 0.648, \quad X_s^p = 0.247, \quad X_u^\Lambda = 0.296, \quad X_s^\Lambda = 0.476 \\
 b = 0.200, \quad \tilde{b} = -0.472, \quad A_g^B = 0.051.
 \end{aligned}
 \tag{30}$$

Table 2: Values of the normalization constants of the the octet baryons FF

Baryon	q_1	q_2	$A_{q_1}^B$	$A_{q_2}^B$	A_Q^B
$p(uud)$	$u = d$	s	0.264	1.168	2.943
$\Lambda(uds)$	$u = d$	s	0.428	1.094	0.720
$\Sigma^+(uus)$	u	s	0.033	0.462	0.180
$\Sigma^-(dds)$	d	s	0.030	0.319	0.180
$\Xi^-(dss)$	d	s	0.023	0.082	0.072

3 Parton distributions and fragmentation functions **figures**

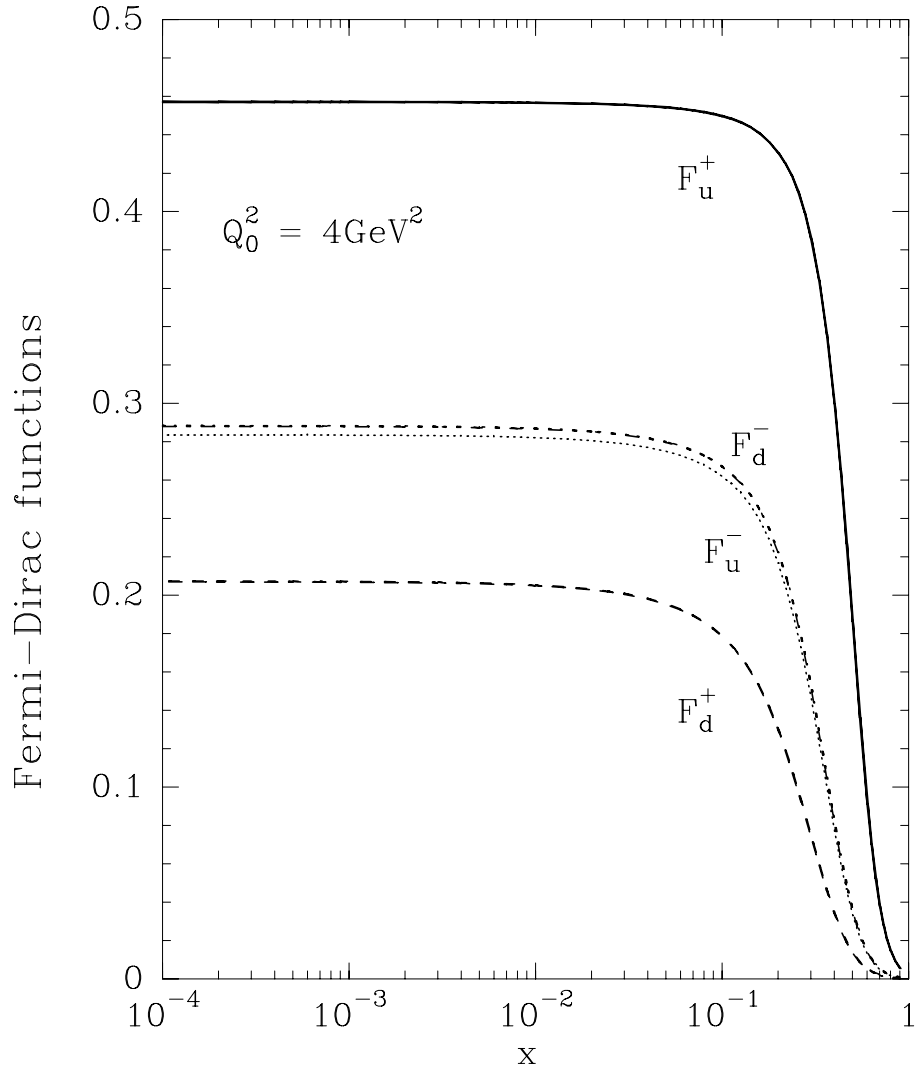


Figure 1: The Fermi-Dirac functions for quarks $F_q^h = X_{0q}^h / (\exp[(x - X_{0q}^h)/\bar{x}] + 1)$ at the input energy scale $Q_0^2 = 4\text{GeV}^2$, as a function of x .

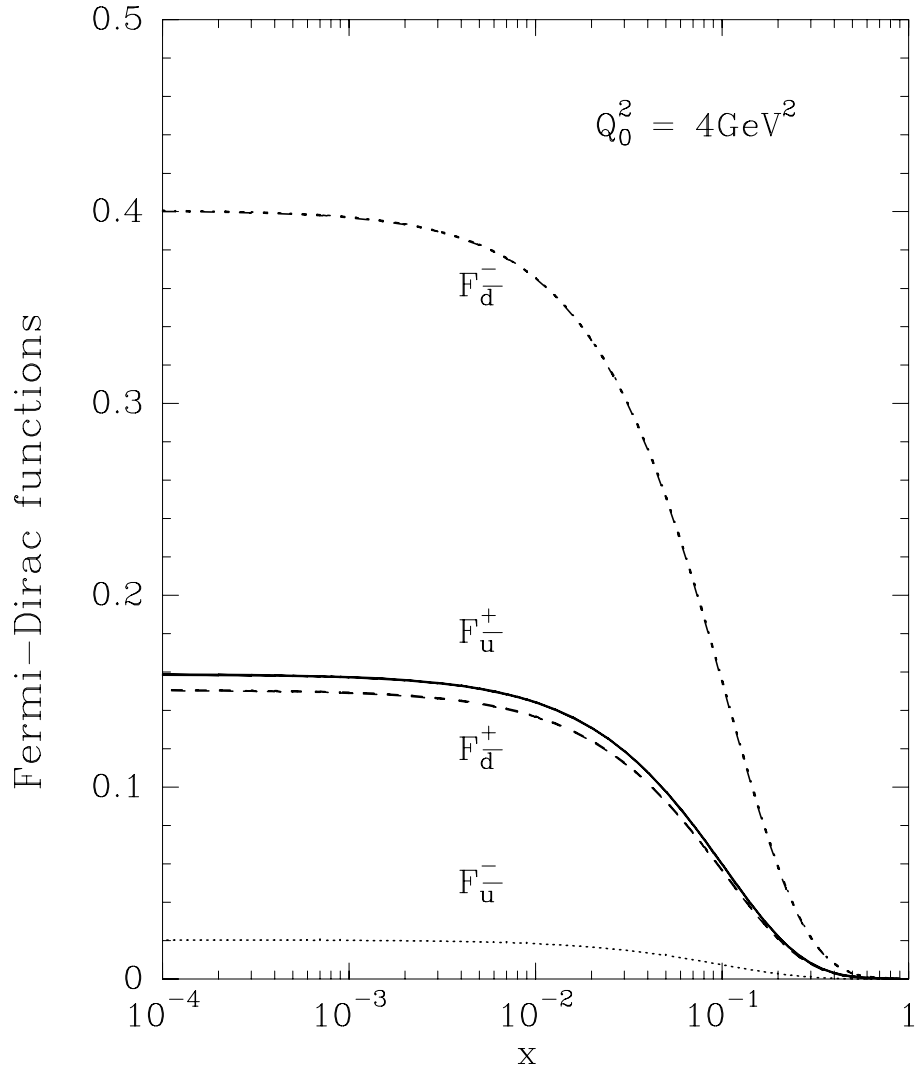


Figure 2: The Fermi-Dirac functions for antiquarks $F_{\bar{q}}^h = 1/X_{0\bar{q}}^h(\exp[(x + X_{0\bar{q}}^h)/\bar{x}] + 1)$ at the input energy scale $Q_0^2 = 4\text{GeV}^2$, as a function of x .

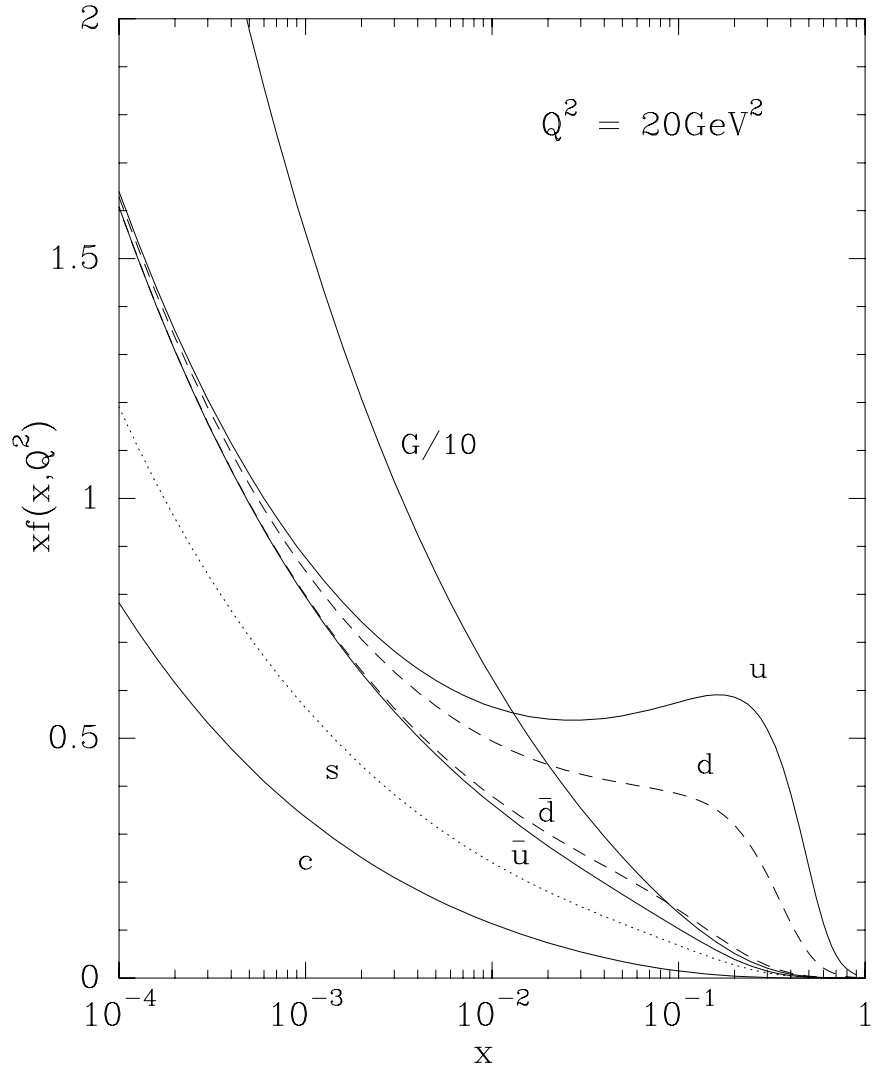


Figure 3: The different unpolarized parton distributions ($f = u, d, \bar{u}, \bar{d}, s, c$ and G) after NLO evolution, at $Q^2 = 20 \text{ GeV}^2$, as a function of x .

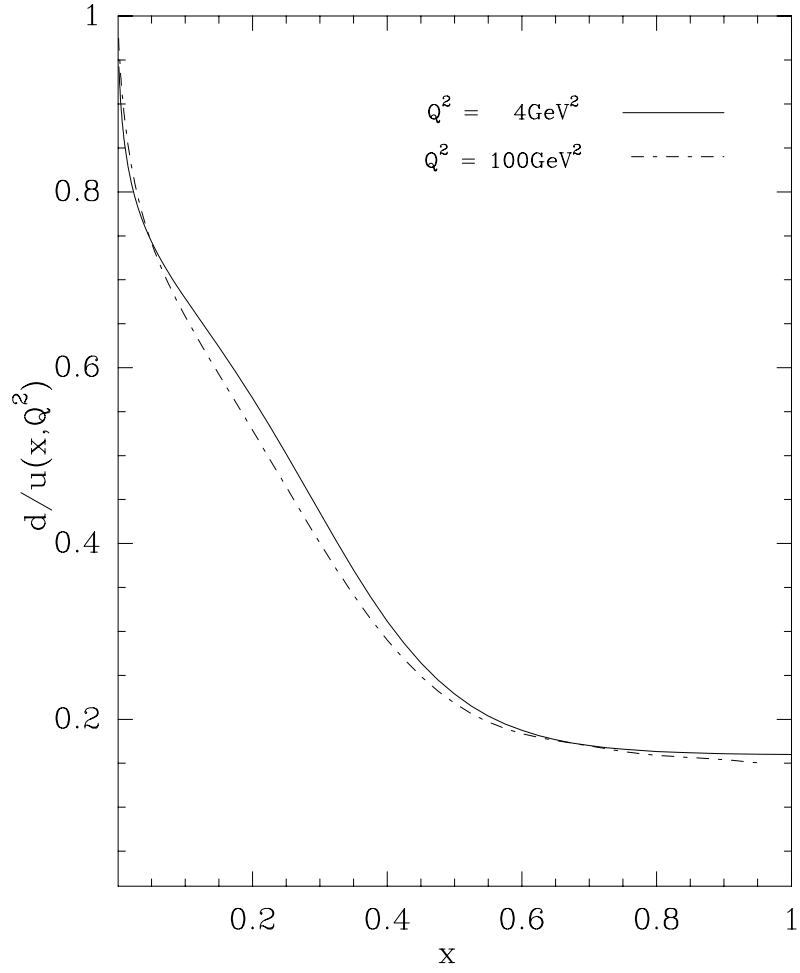


Figure 4: Variation of d/u at large x , for $Q^2 = 4, 100\text{GeV}^2$

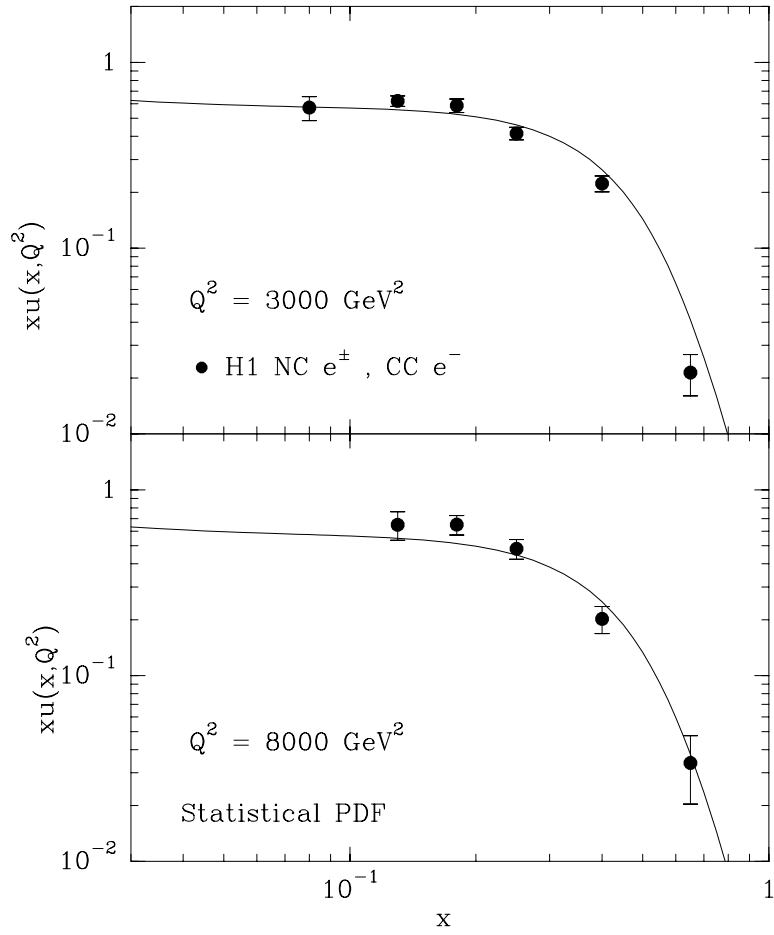


Figure 5: $xu(x, Q^2)$ as function of x for $Q^2 = 3000, 8000 \text{ GeV}^2$, data from H1 collaboration [41, 42].

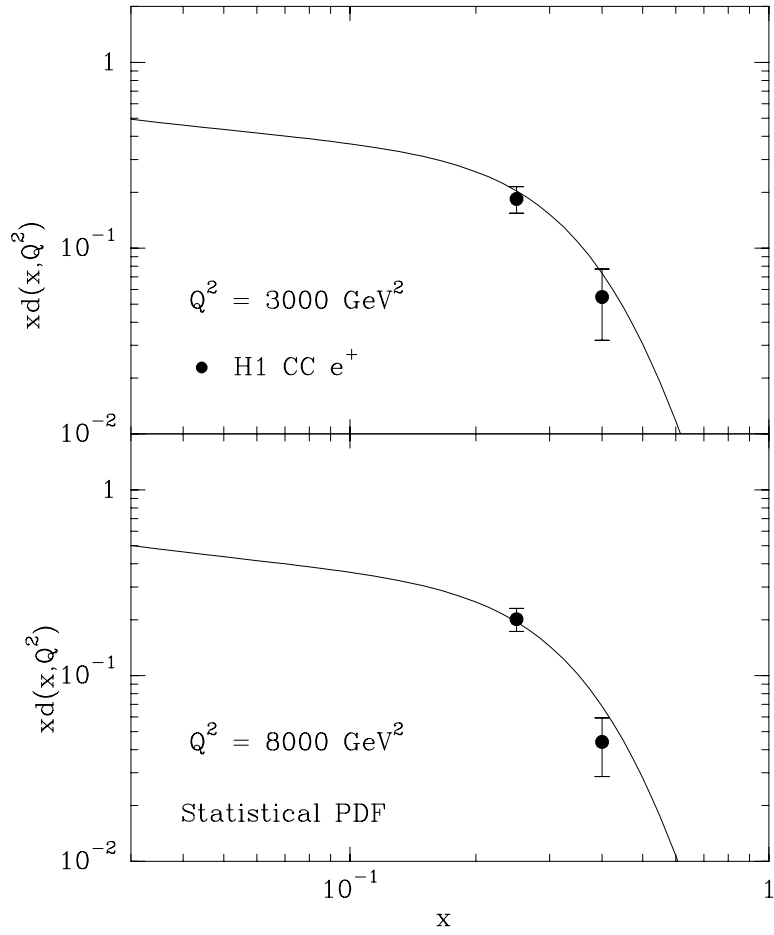


Figure 6: $xd(x, Q^2)$ as function of x for $Q^2 = 3000, 8000\text{GeV}^2$, data from H1 collaboration [41, 42].

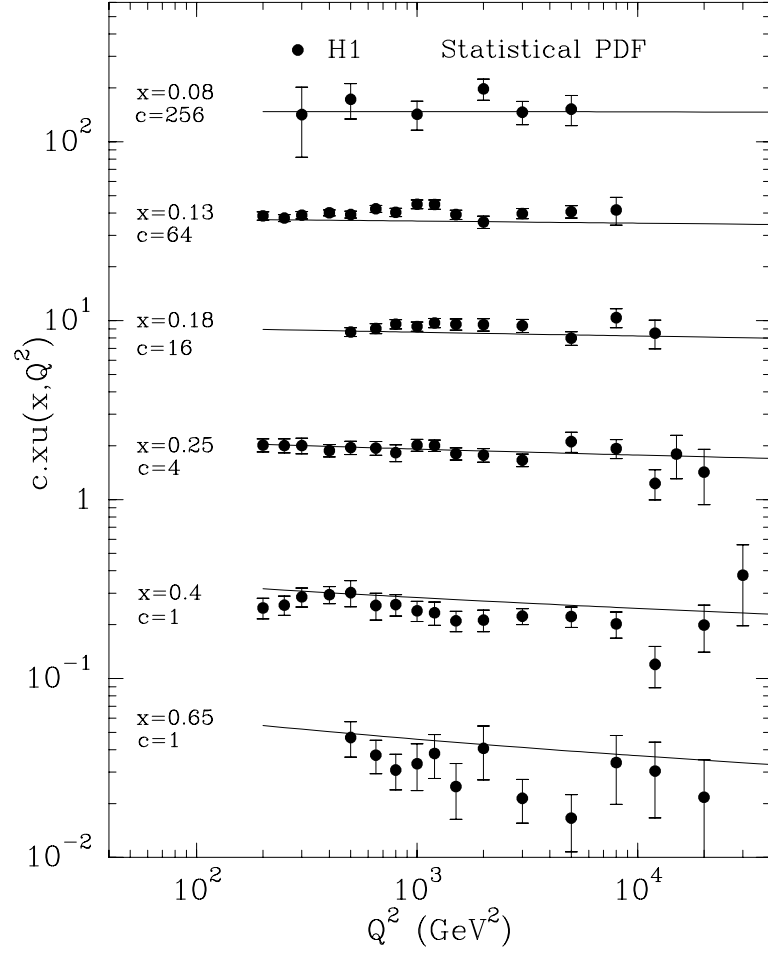


Figure 7: $c \cdot xu(x, Q^2)$ as function of Q^2 for different x bins, data from H1 collaboration [41, 42].

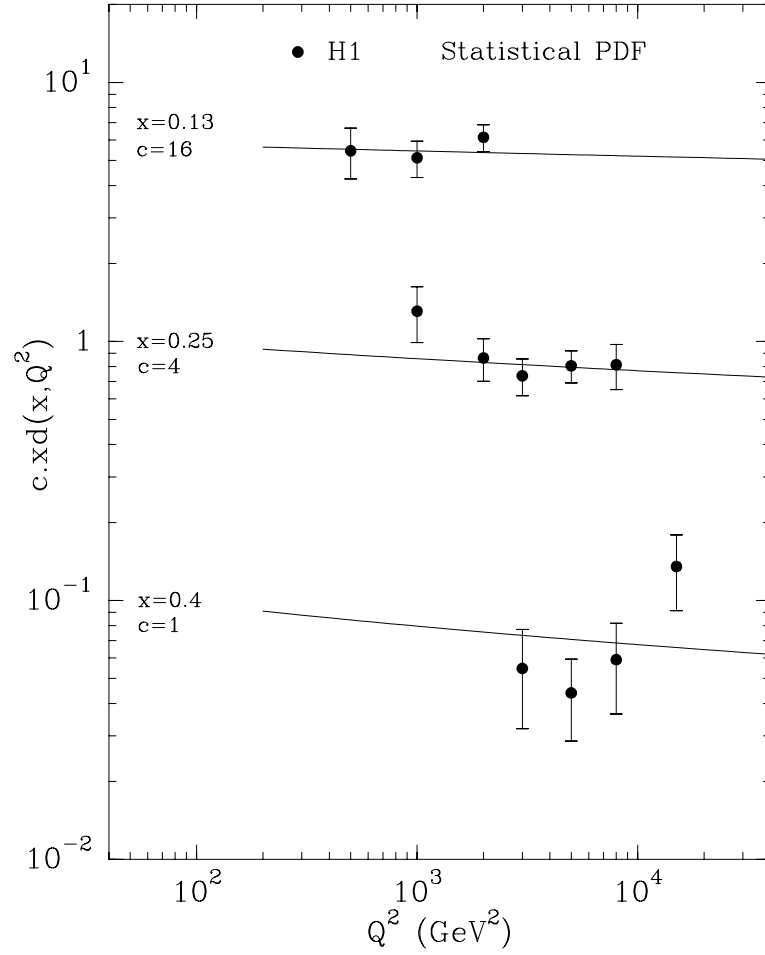


Figure 8: $c \cdot xd(x, Q^2)$ as function of Q^2 for different x bins, data from H1 collaboration [41, 42].

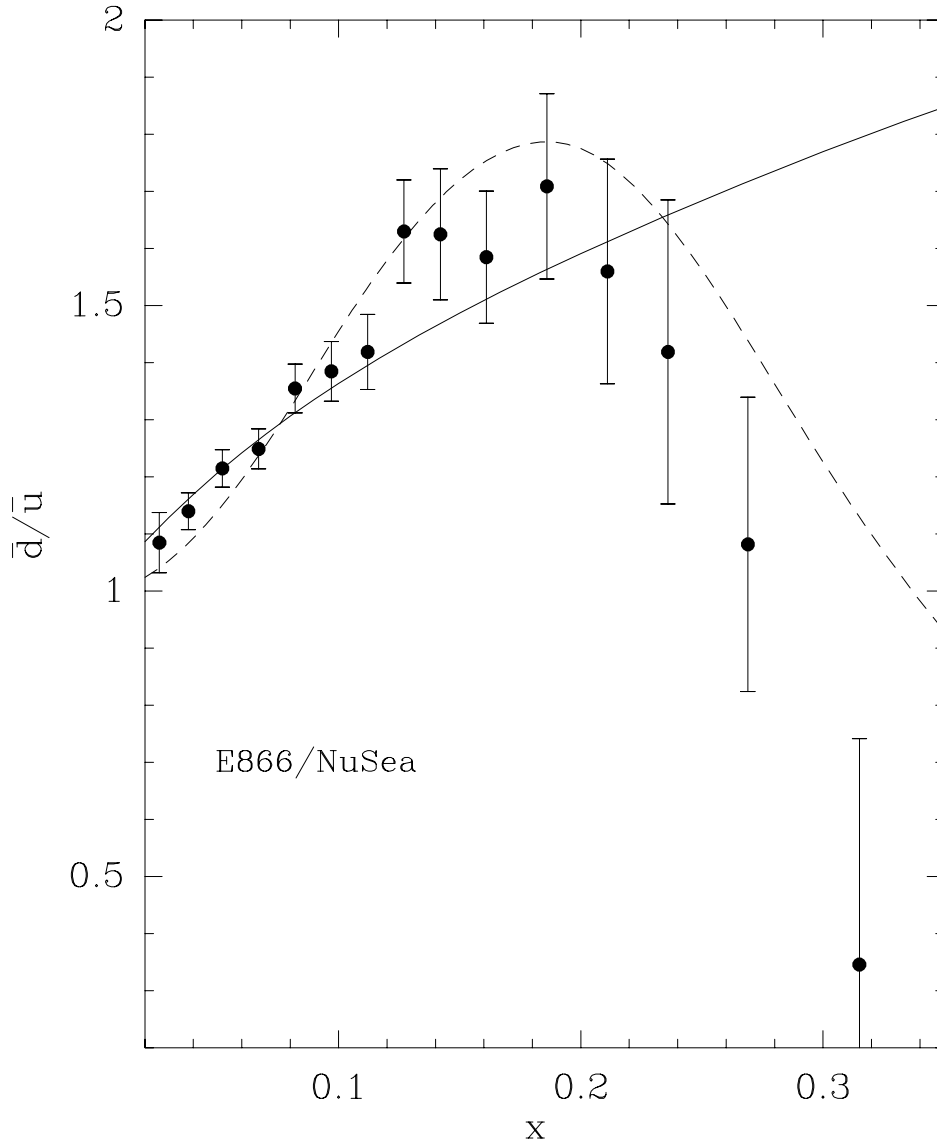


Figure 9: Comparison of the data on $\bar{d}/\bar{u}(x, Q^2)$ from E866/NuSea at $Q^2 = 54\text{GeV}^2$ [25], with the prediction of the statistical model (solid curve) and the set 1 of the parametrization proposed in Ref. [84] (dashed curve).

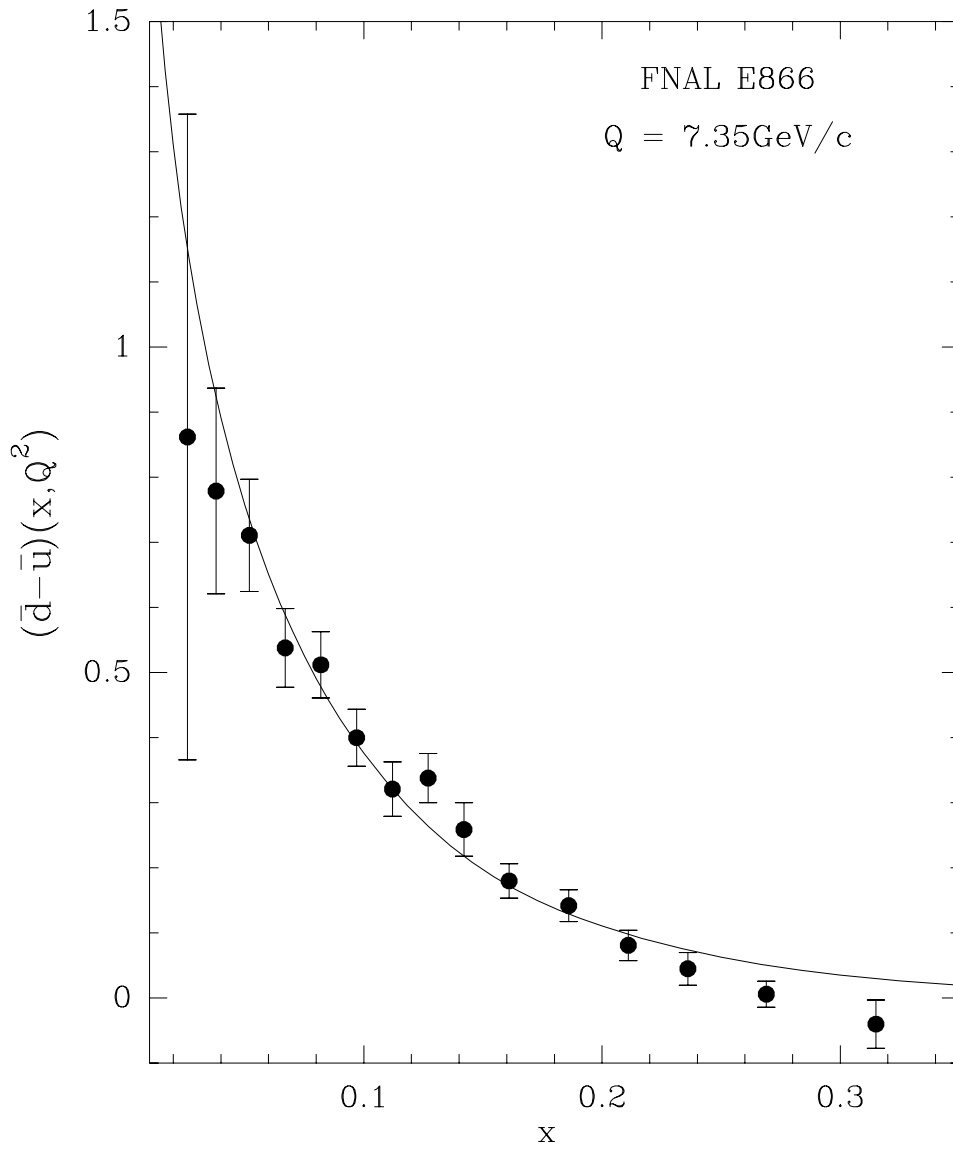


Figure 10: Difference $\bar{d} - \bar{u}$ as a function of x , $Q = 7.35 \text{ GeV}$, experimental results from FNAL-E866.

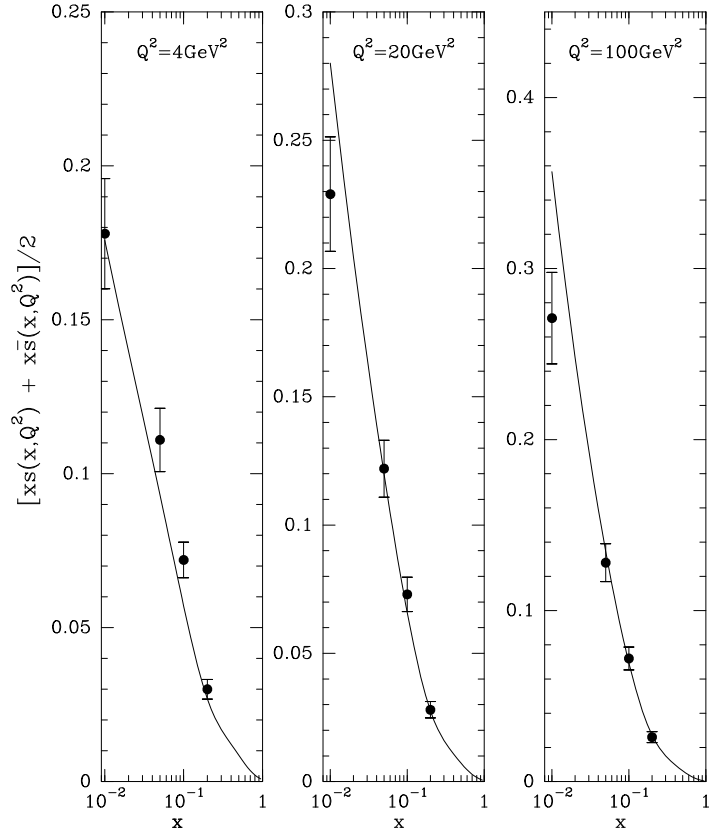


Figure 11: The strange quark distribution $x s(x, Q^2)$ determined at NLO as a function of x for different Q^2 values. Data from CCFR Collaboration [14].

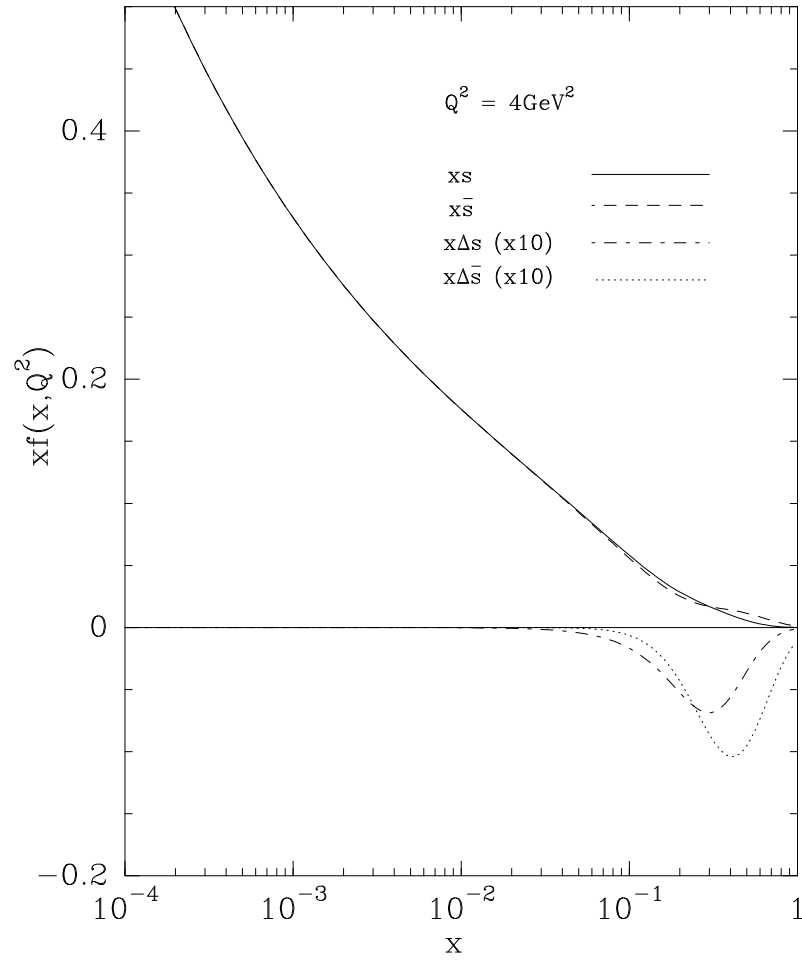


Figure 12: The unpolarized and polarized strange quark and antiquark distributions determined at NLO as a function of x for $Q^2 = 4\text{GeV}^2$.

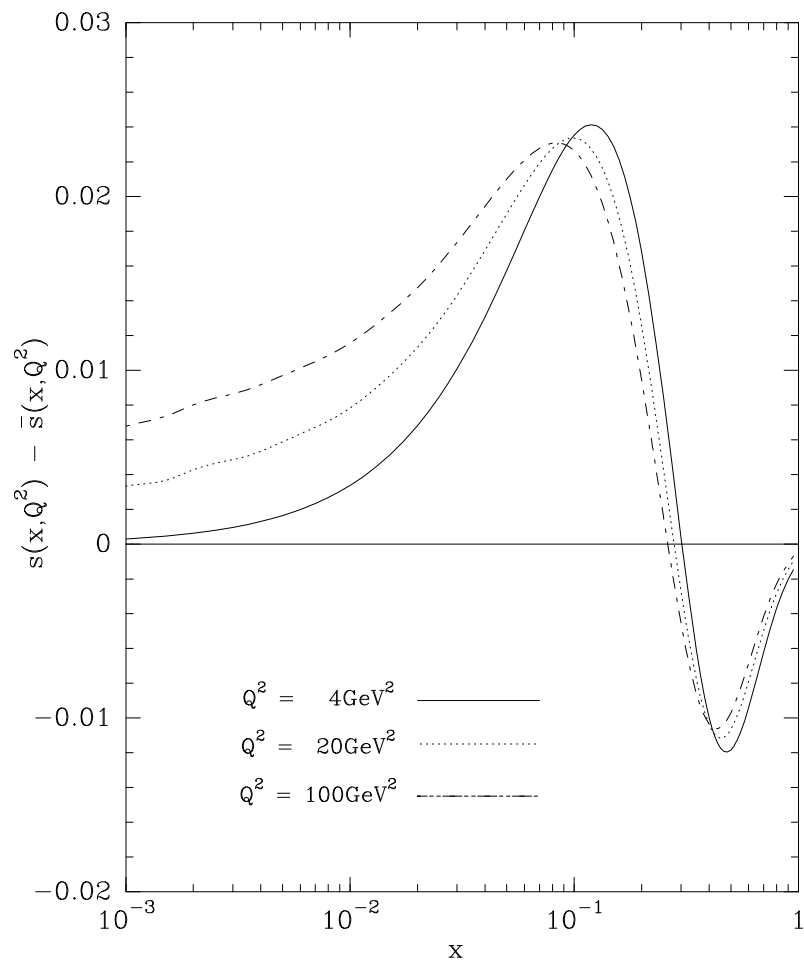


Figure 13: The difference $s - \bar{s}$ quark distributions determined at NLO as a function of x for $Q^2 = 4, 20, 100\text{GeV}^2$.

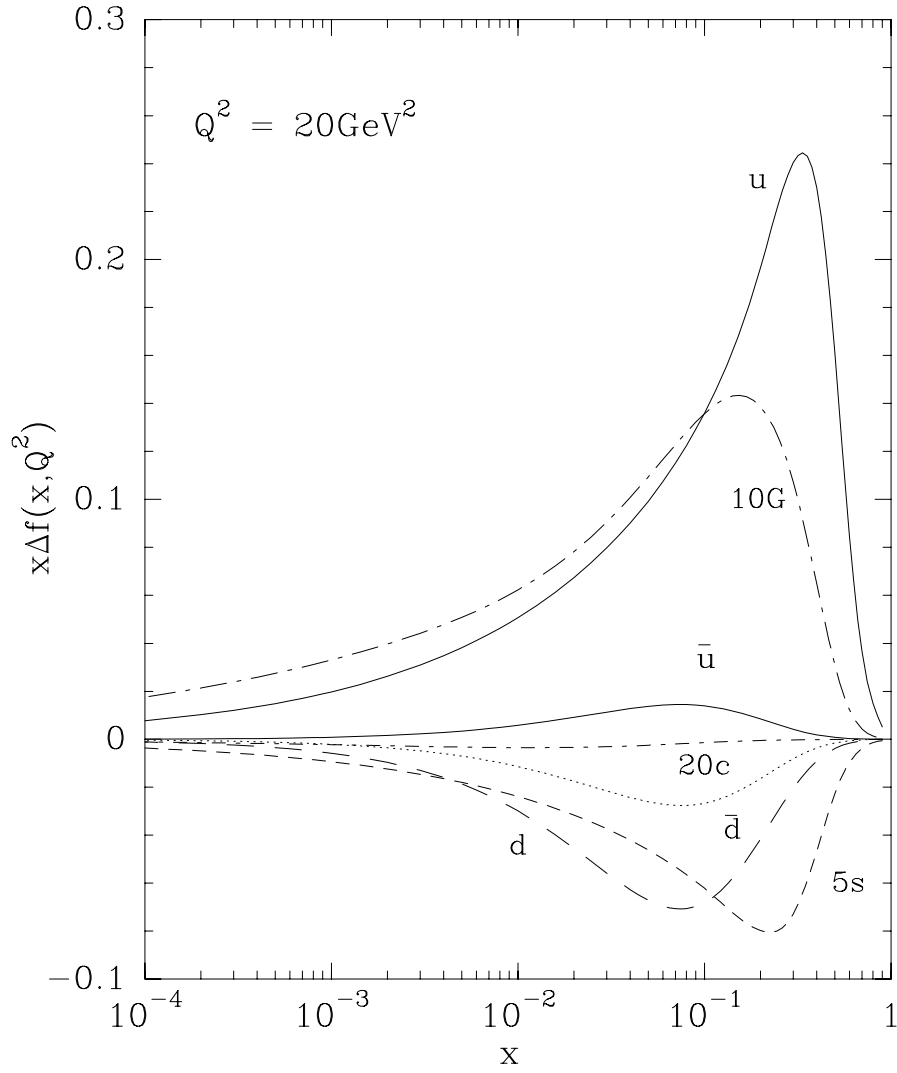


Figure 14: The different polarized parton distributions after NLO evolution, at $Q^2 = 20\text{GeV}^2$, as a function of x .

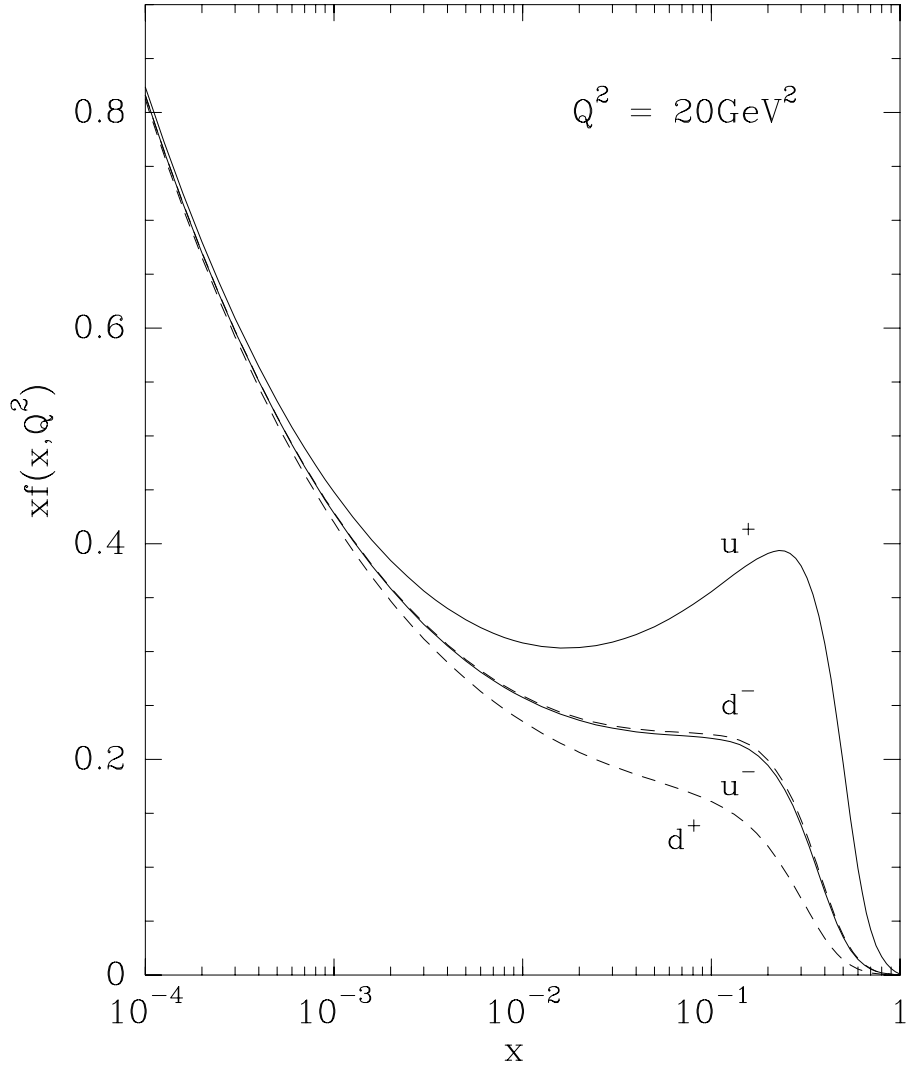


Figure 15: The different helicity components of the light quark distributions after NLO evolution, at $Q^2 = 20\text{GeV}^2$, as a function of x .

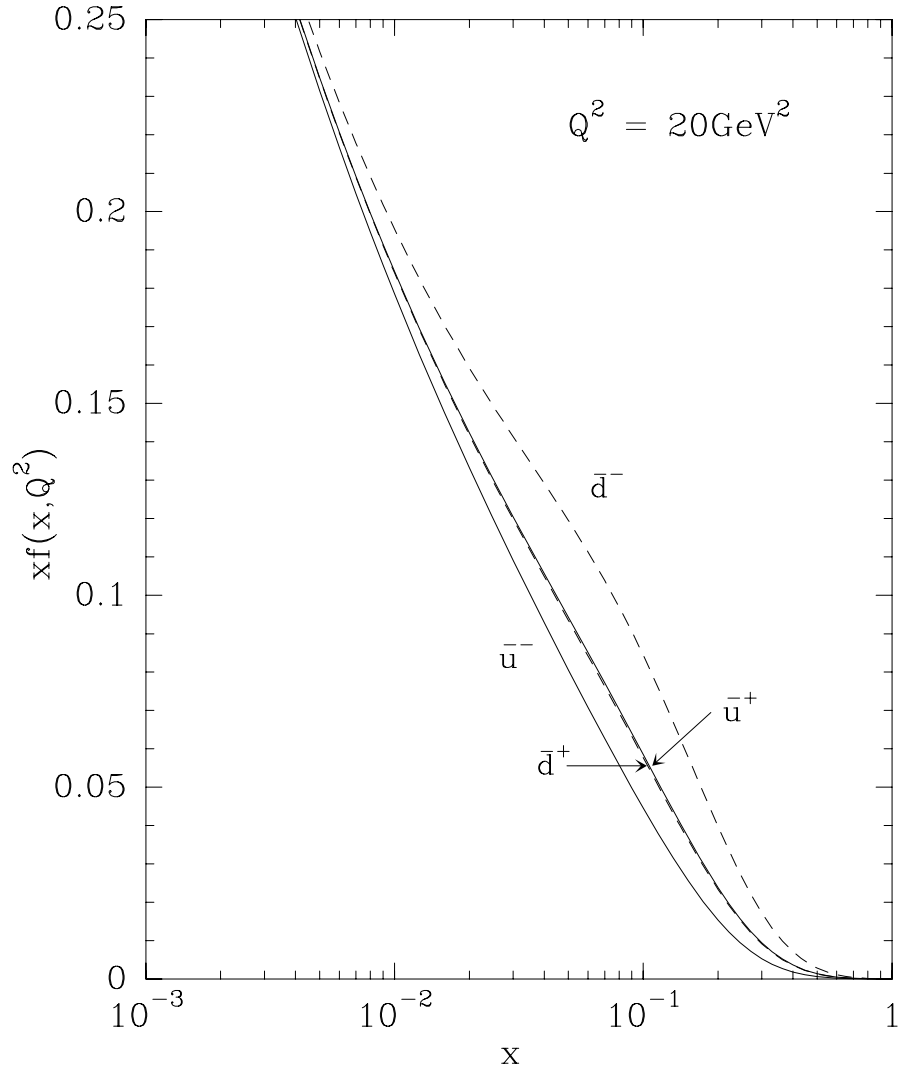


Figure 16: The different helicity components of the light antiquark distributions after NLO evolution, at $Q^2 = 20 \text{ GeV}^2$, as a function of x .

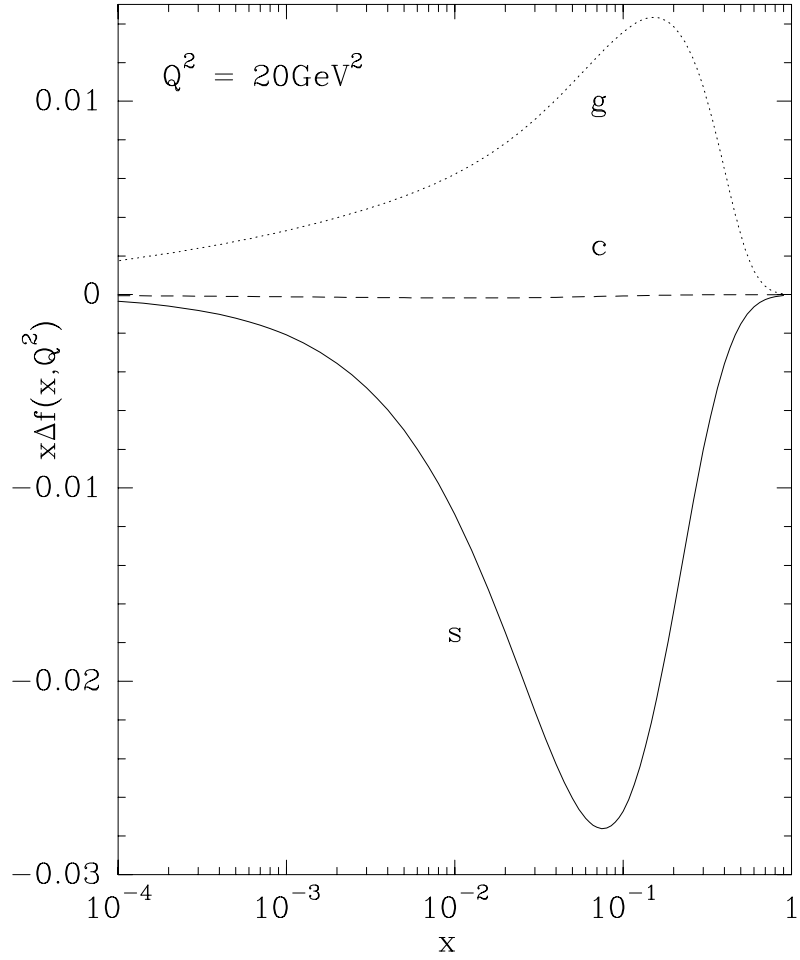


Figure 17: Details of the polarized parton distributions g , s , c , after NLO evolution, at $Q^2 = 20 \text{ GeV}^2$, as a function of x .

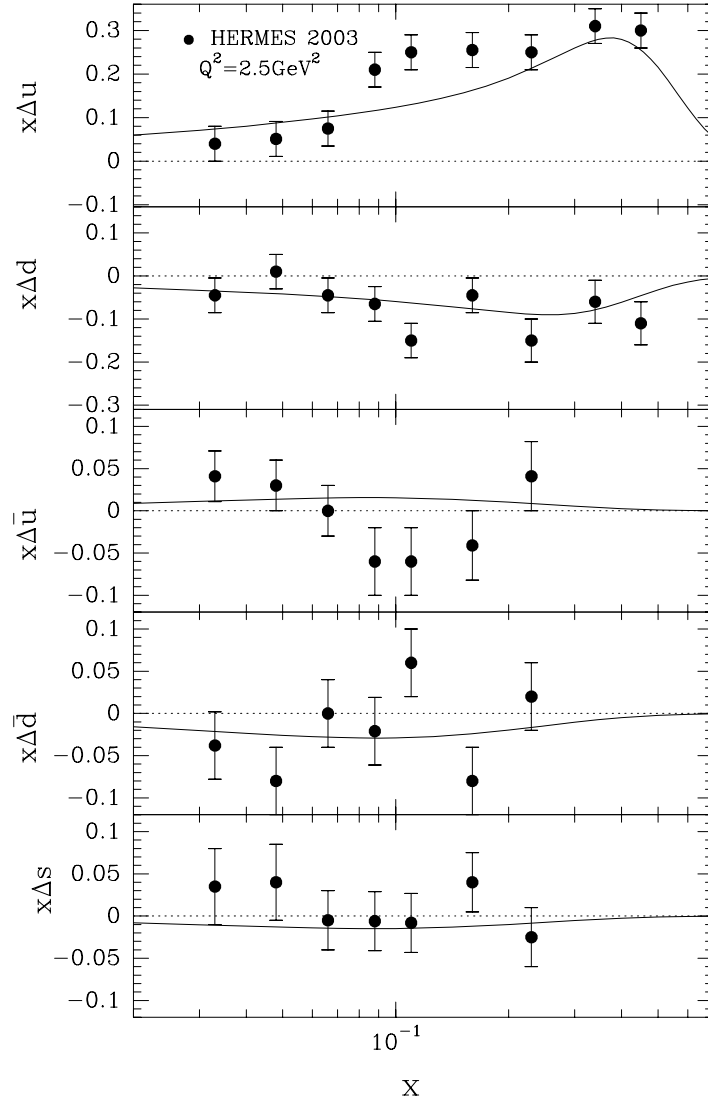


Figure 18: Quark helicity distributions at $\langle Q^2 \rangle = 2.5 \text{ GeV}^2$, as a function of x . Data from HERMES Coll. [46].

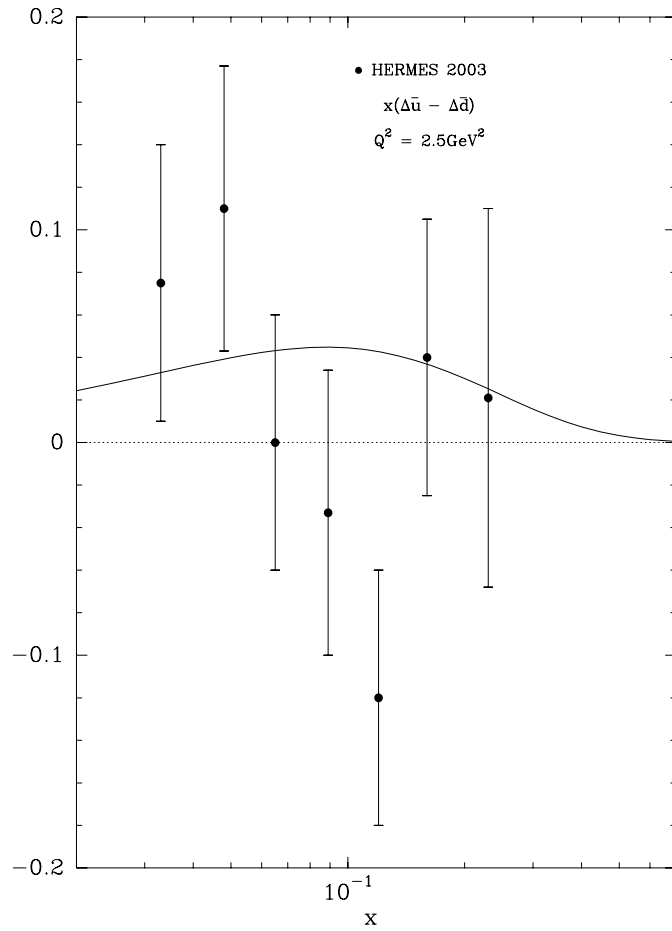


Figure 19: Flavor asymmetry $\Delta\bar{u} - \Delta\bar{d}$ of the light sea quark as a function of x , for $Q^2 = 2.5\text{GeV}^2$. Data from HERMES Coll. [46].

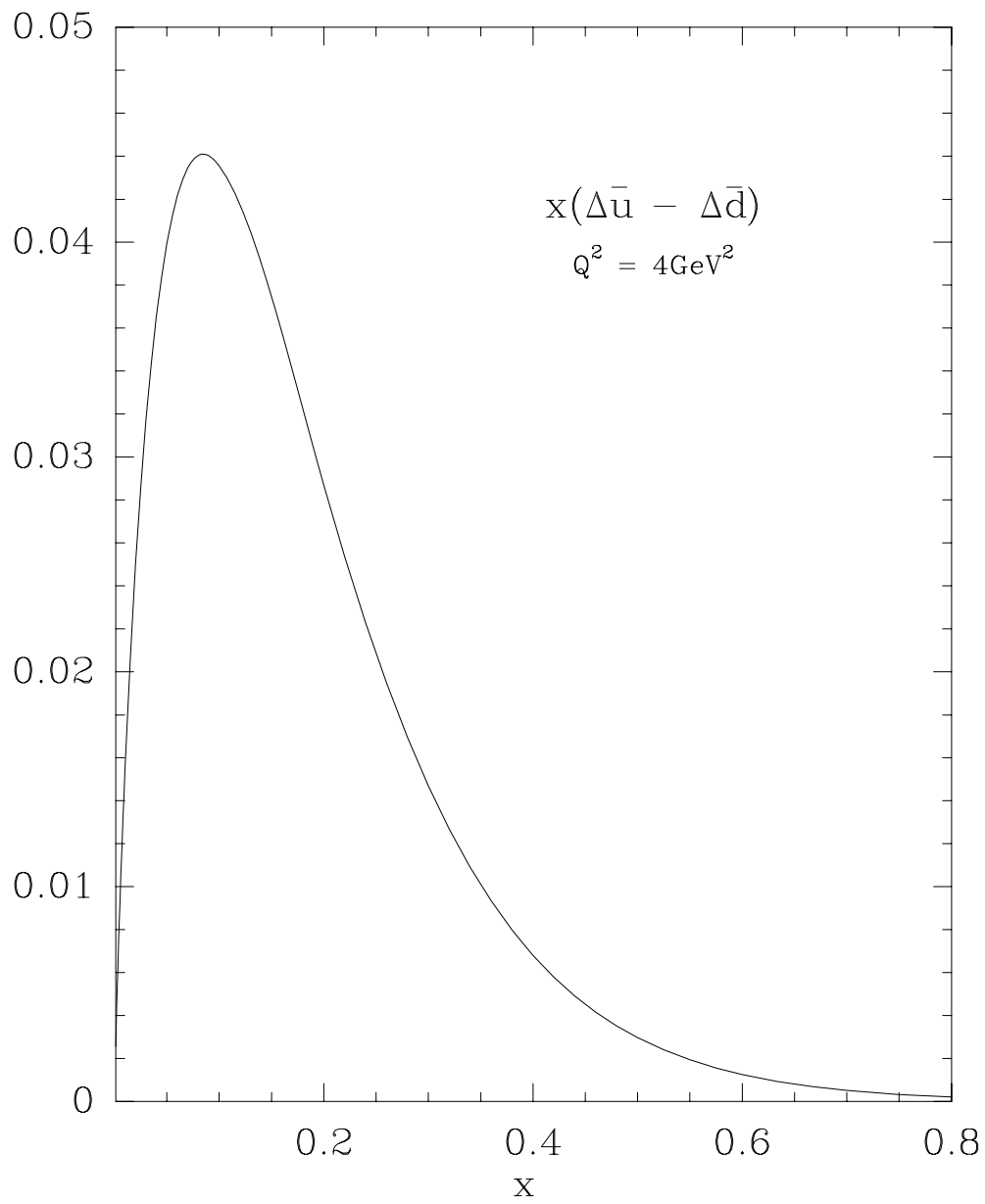


Figure 20: Flavor asymmetry $\Delta\bar{u} - \Delta\bar{d}$ of the light sea quark as a function of x , for $Q^2 = 4\text{GeV}^2$.

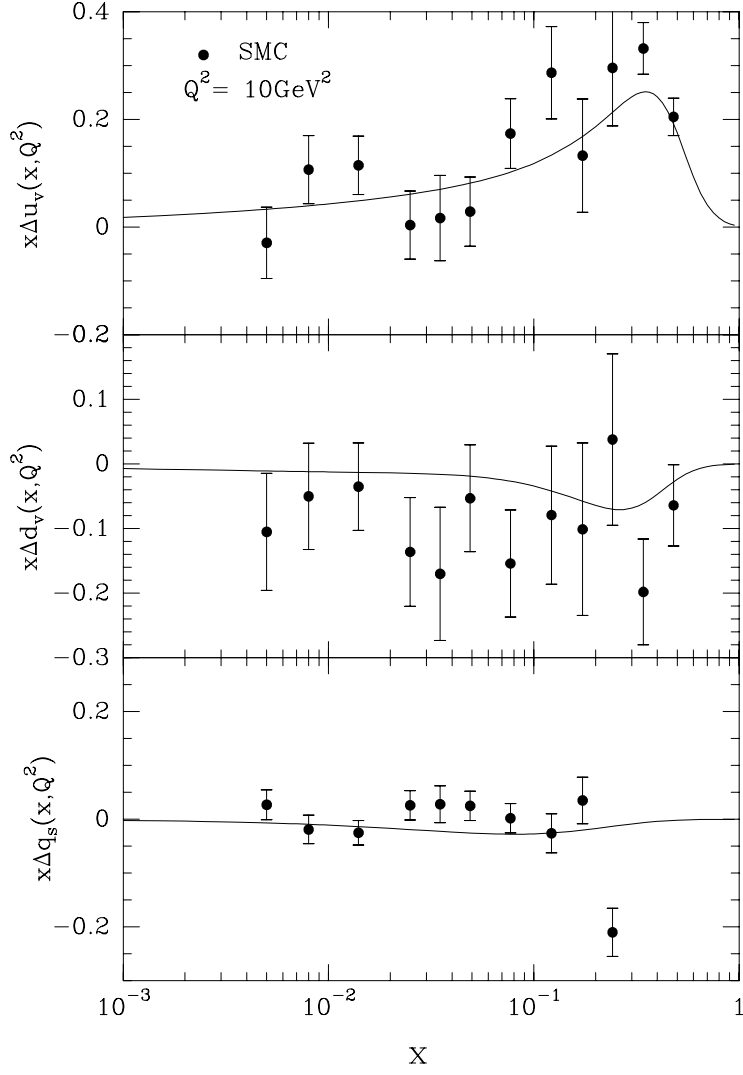


Figure 21: $x\Delta u_v$, $x\Delta d_v$, $x\Delta \bar{q}$ as function of x at fixed $Q^2 = 10 \text{ GeV}^2$, experiment SMC Coll..

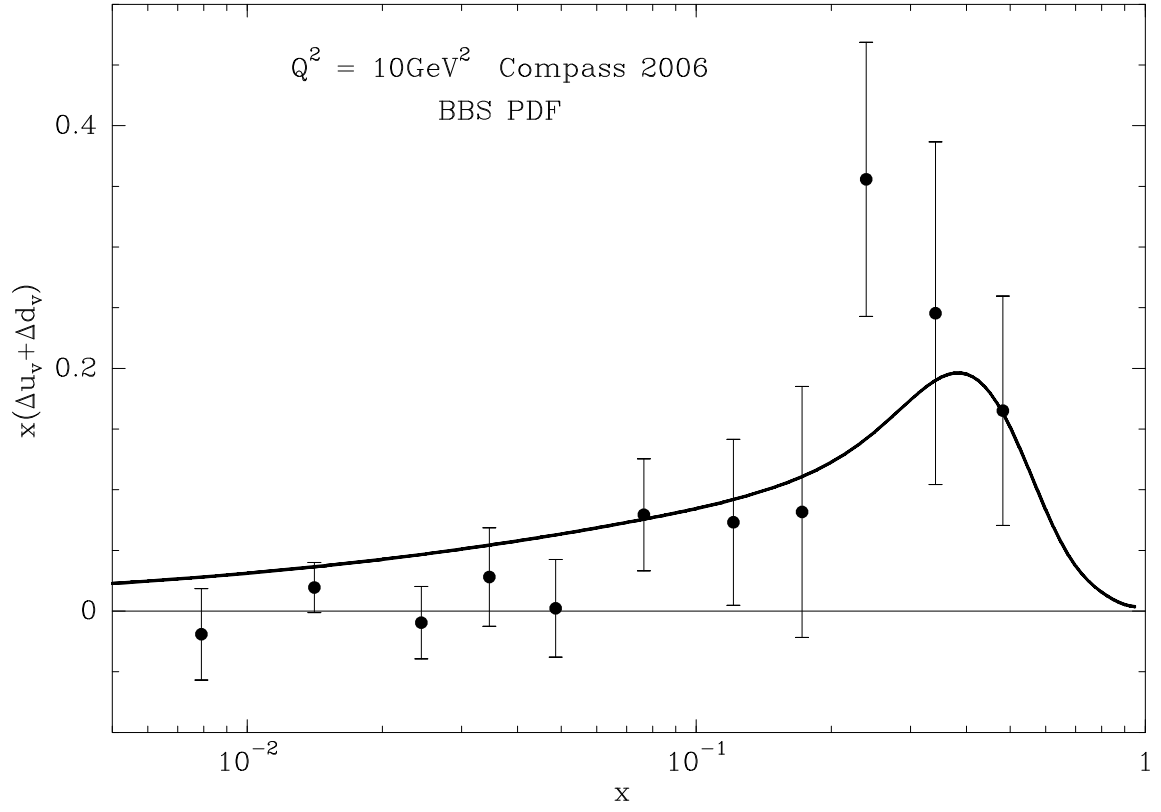


Figure 22: The sum of polarized valence quark distributions determined at NLO as a function of x for $Q^2 = 10\text{GeV}^2$, data from Compass Collaboration [109, 110].

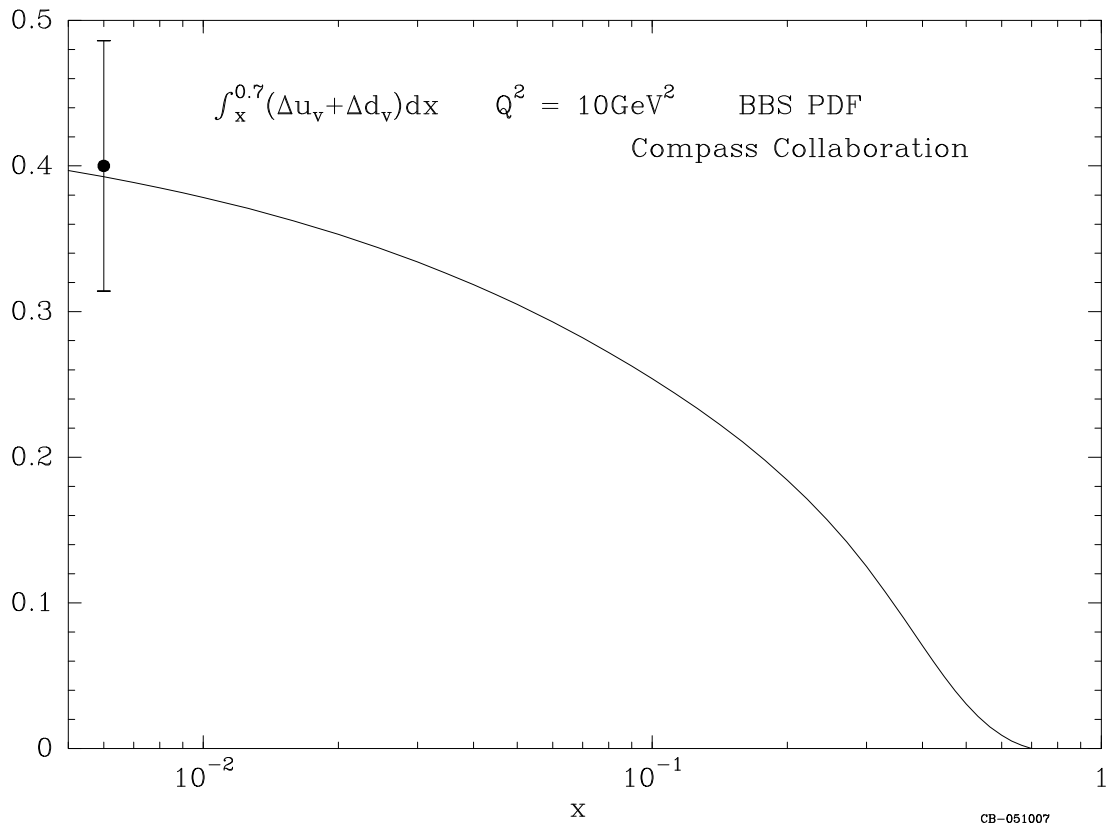


Figure 23: Prediction for the integral $\Delta u_v + \Delta d_v$ determined at NLO as a function of the lower limit x for $Q^2 = 10 \text{ GeV}^2$.

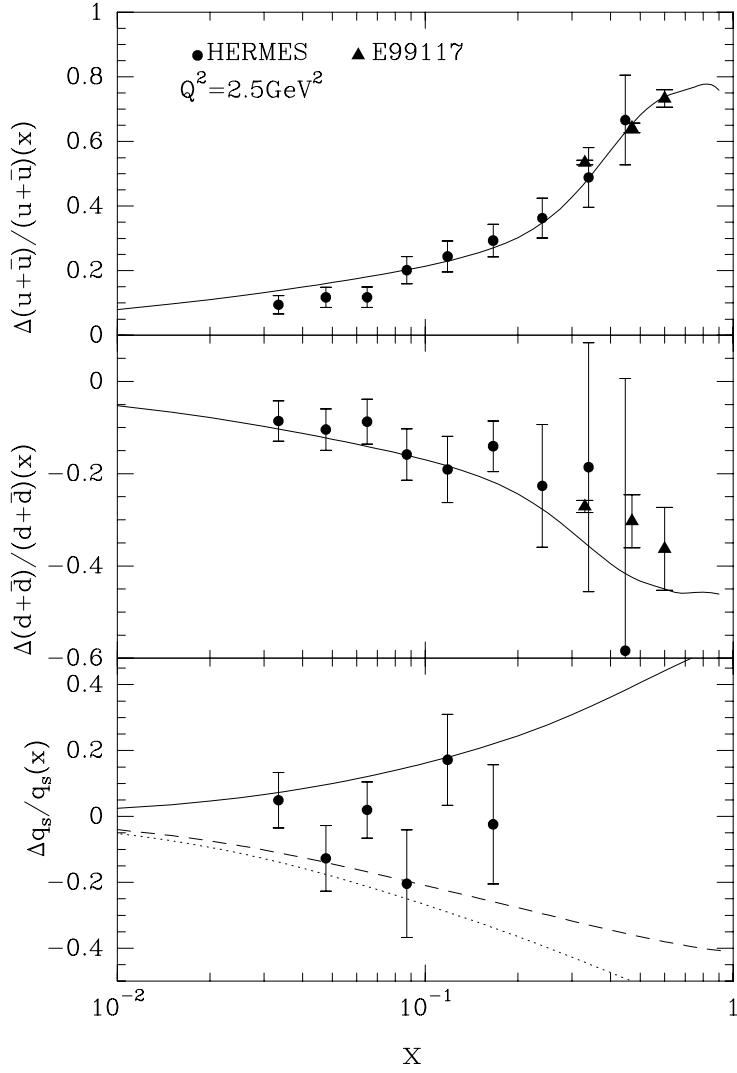


Figure 24: HERMES [44] and E99-117 [54] data on $(\Delta u + \Delta \bar{u})/(u + \bar{u})$, $(\Delta d + \Delta \bar{d})/(d + \bar{d})$, $\Delta q_s/q_s$ as function of x at fixed $Q^2 = 2.5 \text{ GeV}^2$. The curves are our model calculations. For the sea quarks $\Delta \bar{u}/\bar{u}$ (solid curve), $\Delta \bar{d}/\bar{d}$ (dashed curve) and $\Delta s/s$ (dotted curve).

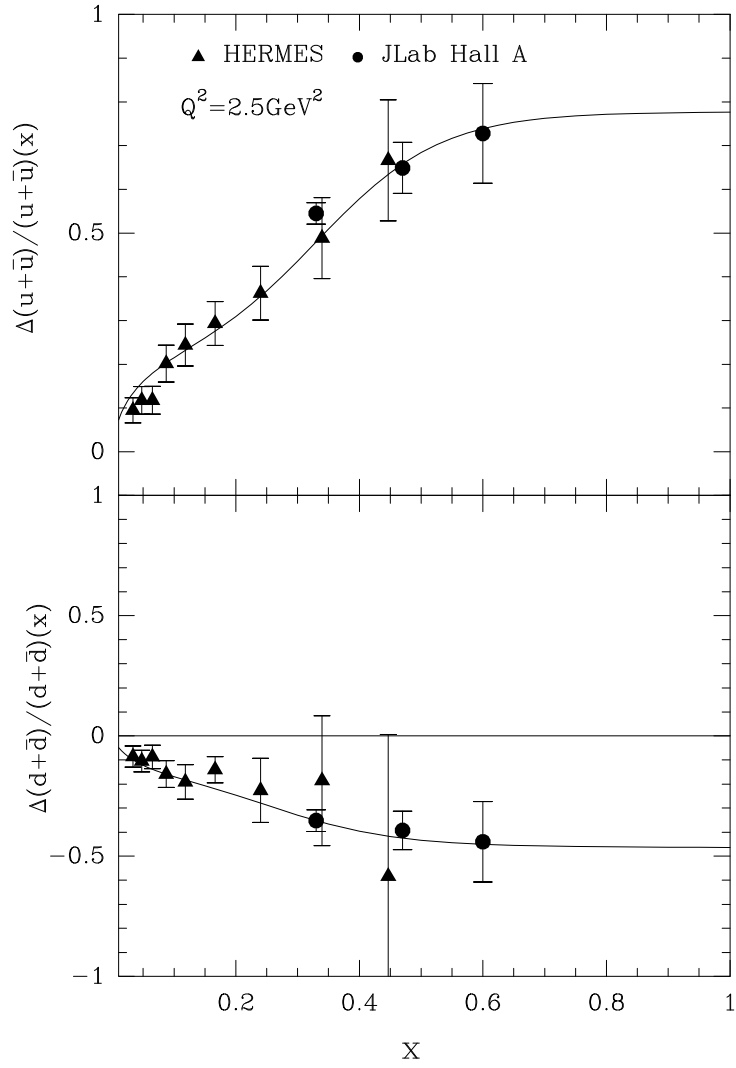


Figure 25: Ratios $(\Delta u + \Delta \bar{u})/(u + \bar{u})$ and $(\Delta d + \Delta \bar{d})/(d + \bar{d})$ as a function of x for $Q^2 = 2.5 \text{ GeV}^2$. Data from Hermes [44] and JLab experiments [45].

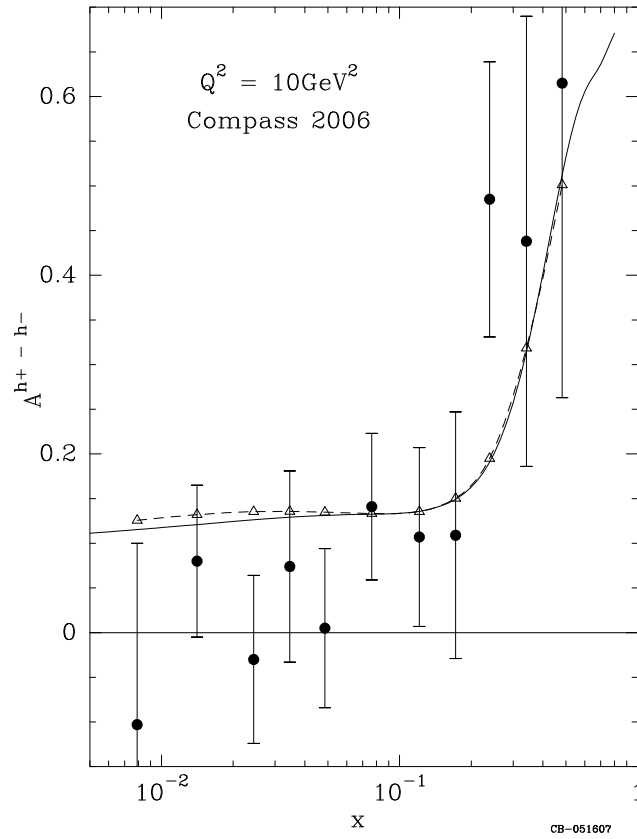


Figure 26: Prediction of BBS PDF for the difference asymmetry $A^{h^+ - h^-}$ determined at NLO as a function of x for $Q^2 = 10 \text{ GeV}^2$, data from Compass Collaboration.

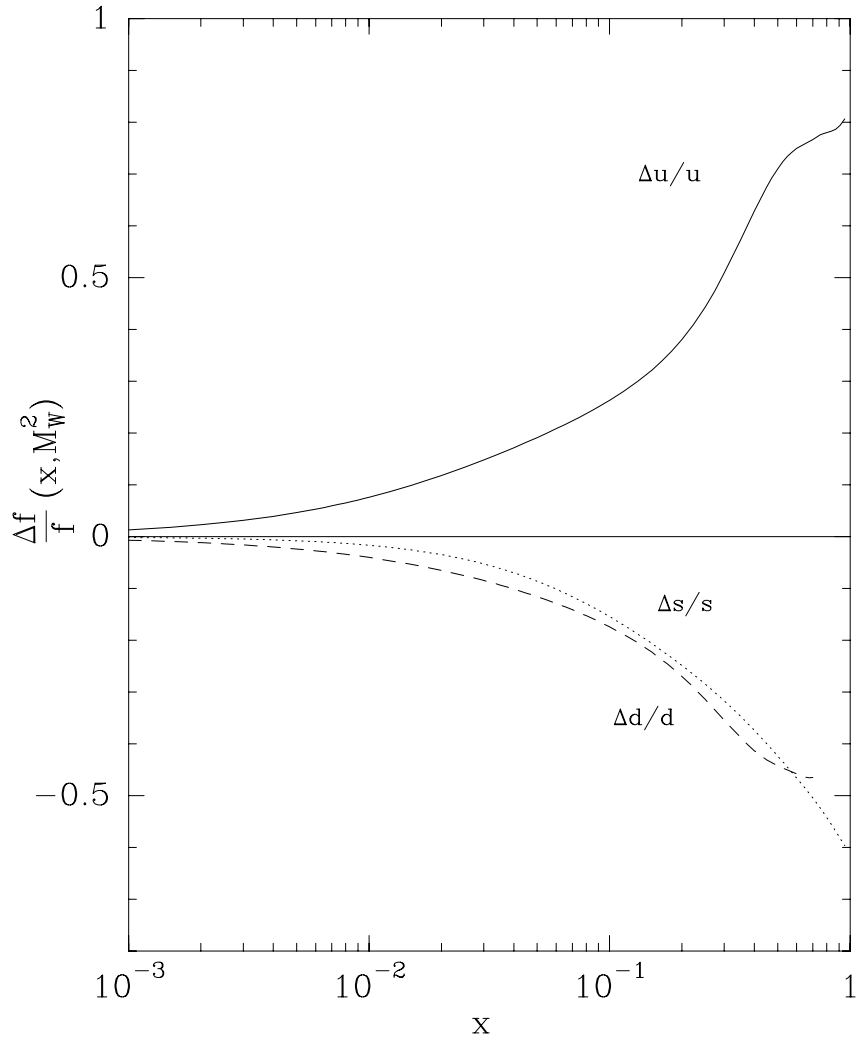


Figure 27: Ratio polarized/unpolarized quark distributions for u , d , s , at $Q^2 = 4\text{GeV}^2$.

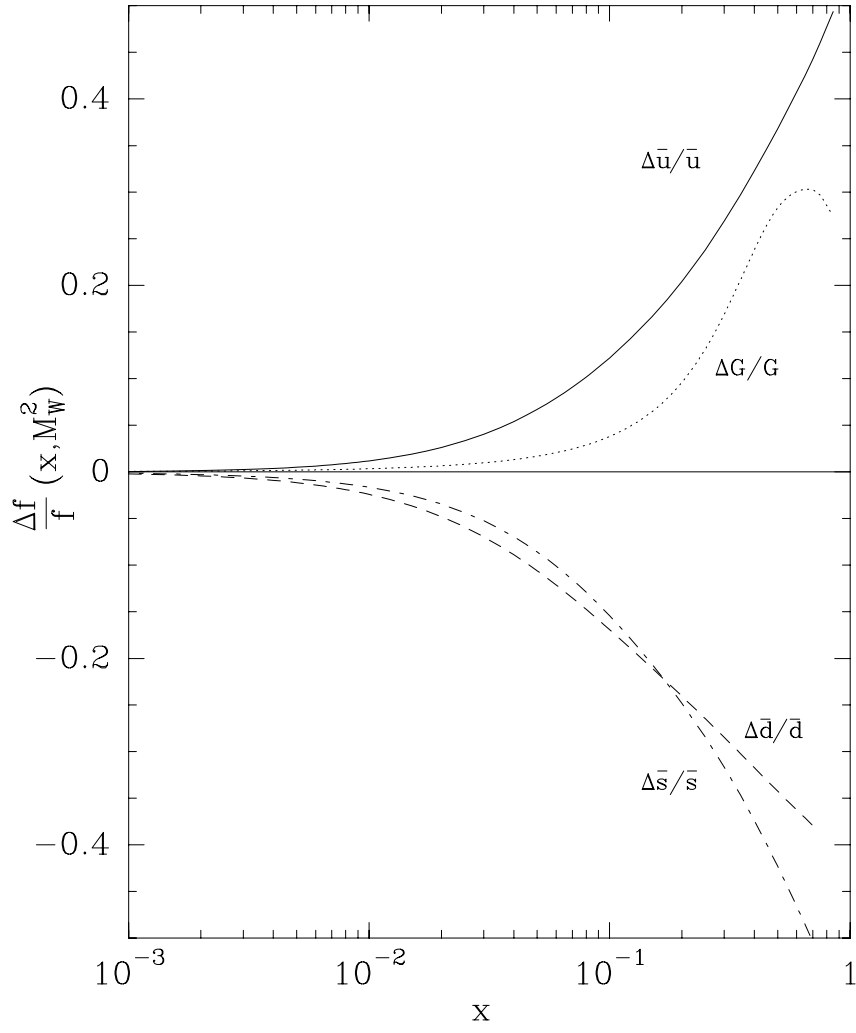


Figure 28: Ratio polarized/unpolarized antiquark distributions for \bar{u} , \bar{d} , \bar{s} and G , at $Q^2 = 4\text{GeV}^2$.

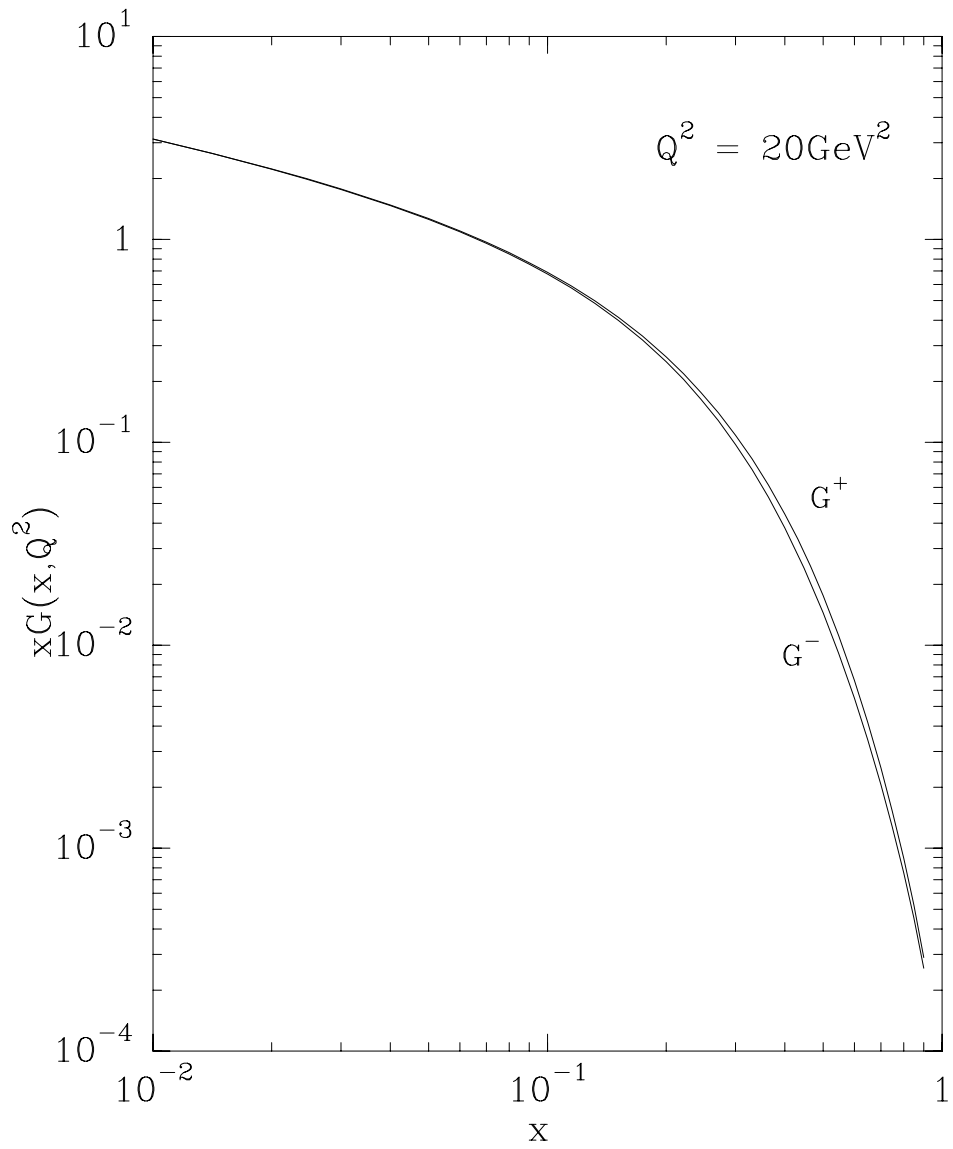


Figure 29: Spin components of gluon density

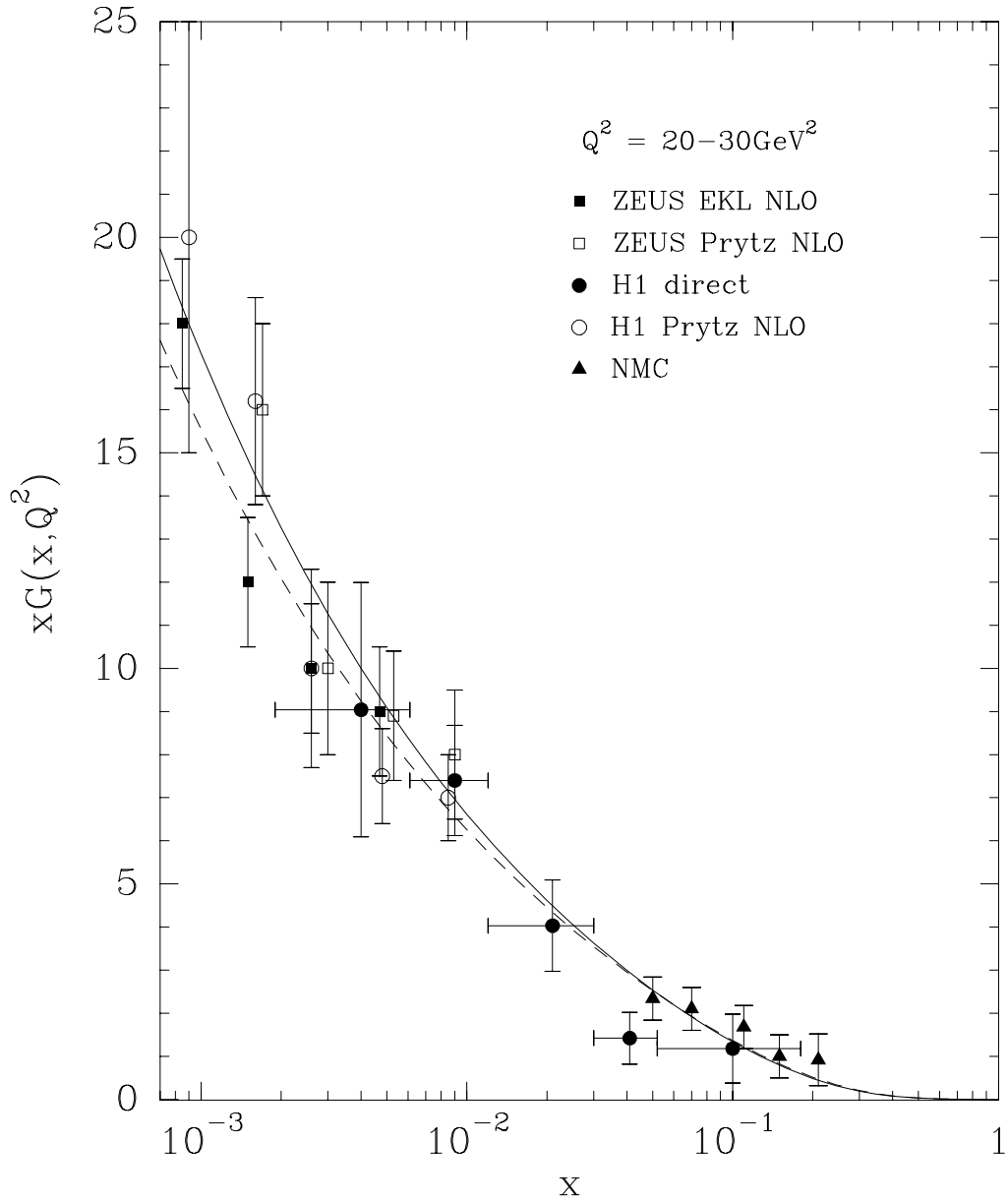


Figure 30: Comparison of $xG(x, Q^2)$ at $Q^2 = 20 - 30\text{GeV}^2$ (dashed-solid) with experimental determination from NMC [57], H1 [39] and ZEUS [91] experiments.

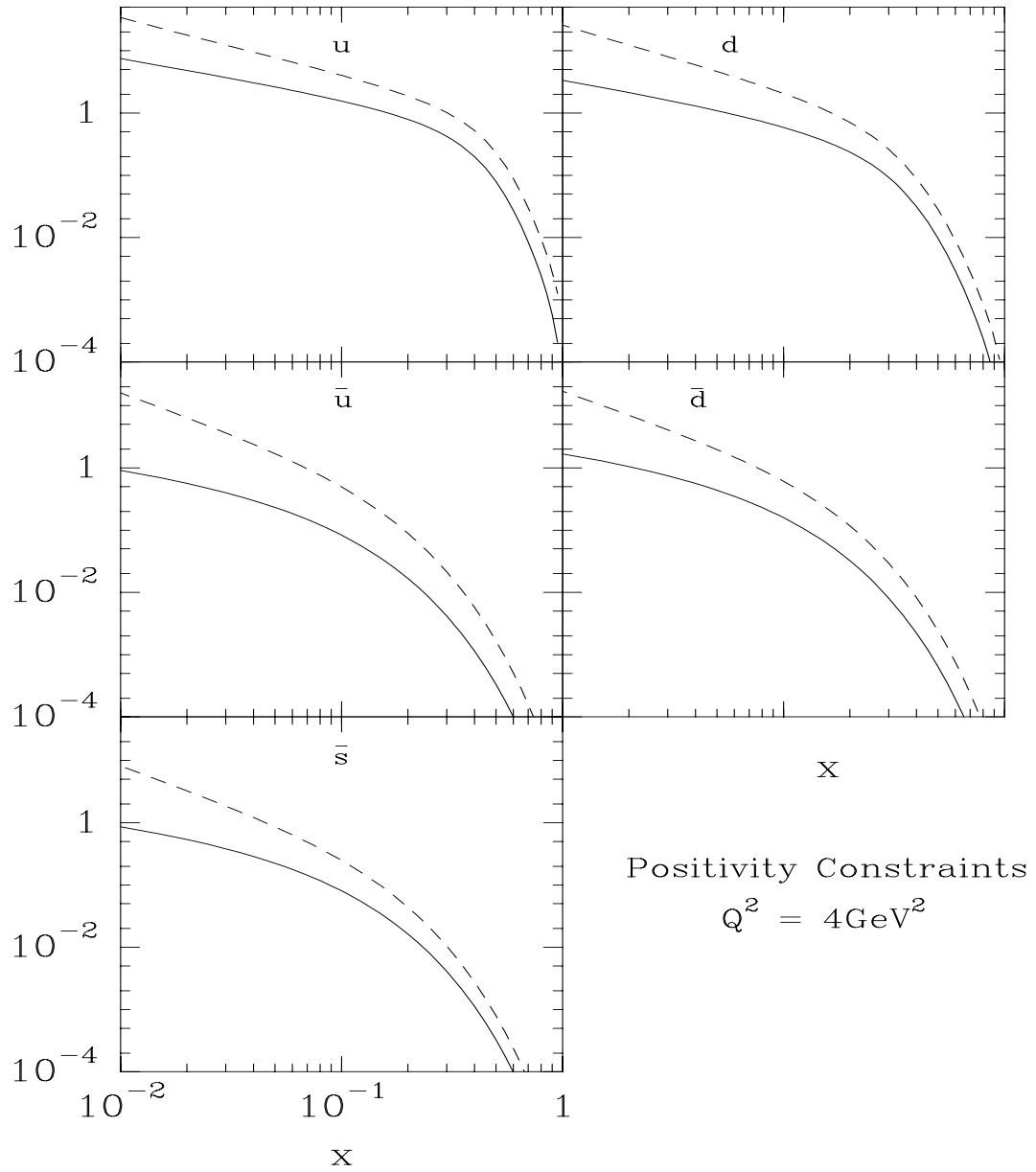


Figure 31: Positivity constraints between polarized and unpolarized distributions according to the inequality of Soffer-Teryaev [98].

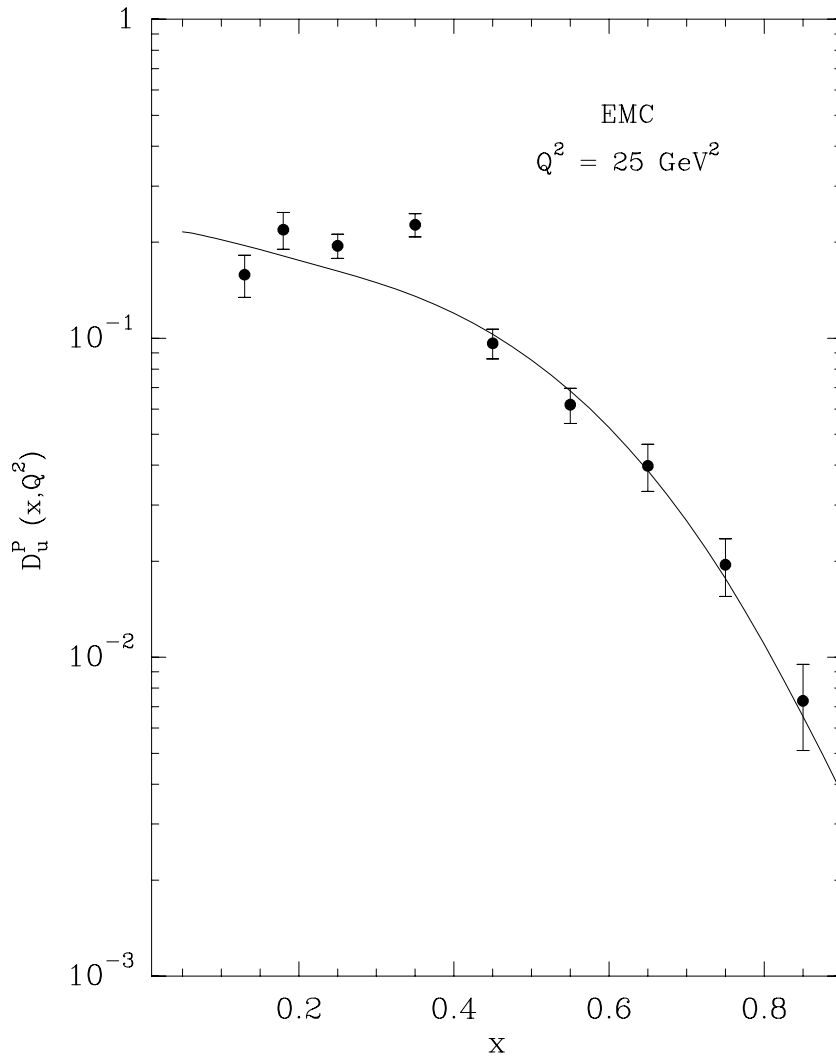


Figure 32: The u quark to proton fragmentation function $D_u^p(x, Q^2)$ as a function of x at $Q^2 = 25 \text{ GeV}^2$. The experimental data are from Ref. [36].

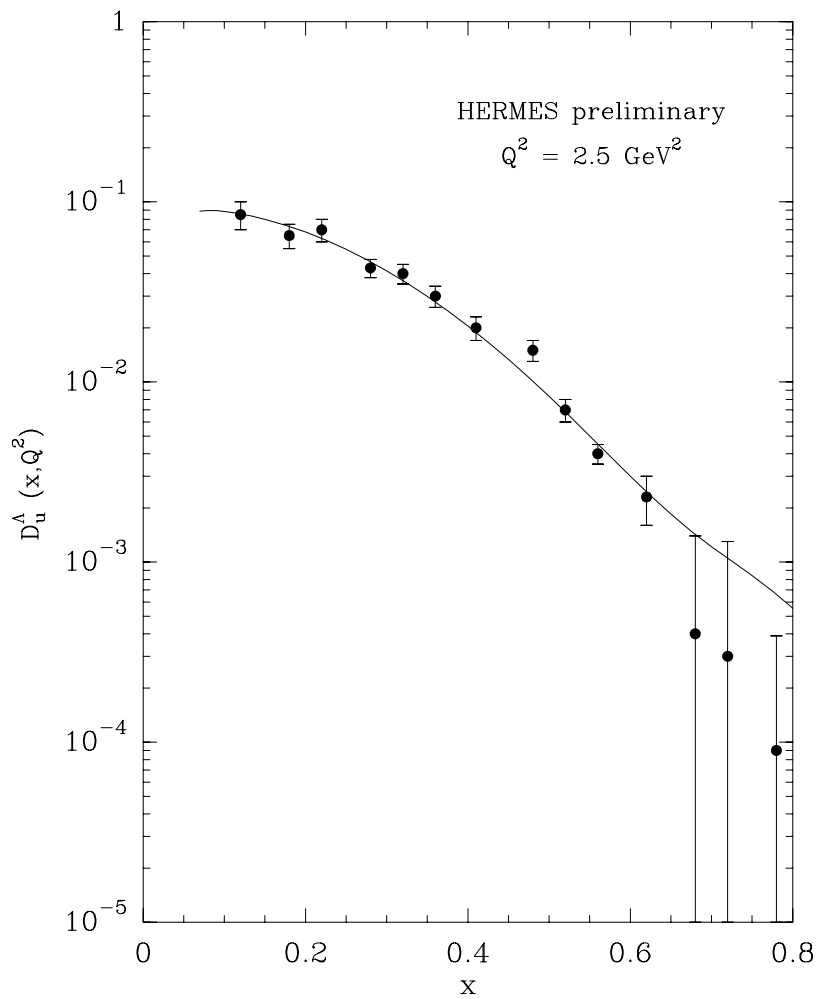


Figure 33: The fragmentation function for u quark to Λ , $D_u^\Lambda(x, Q^2)$, as a function of x at $Q^2 = 2.5 \text{ GeV}^2$. The experimental data are from Ref. [43].

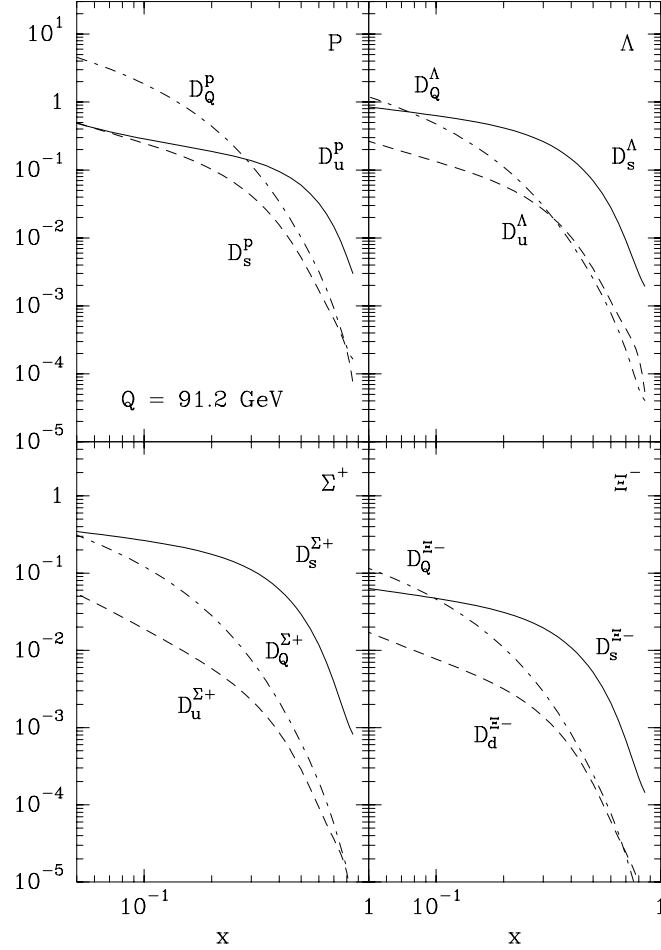


Figure 34: The quark to octet baryons fragmentation functions $D_q^B(x, Q^2)$ and $D_Q^B(x, Q^2)$ ($B = p, \Lambda, \Sigma^\pm, \Xi^\pm$, $q = u, d, s$ and $Q = c, b, t$), as a function of x at $Q = 91.2\text{GeV}$. Note that we used different vertical scales in the upper and lower parts of the figure.

4 Unpolarized experiments

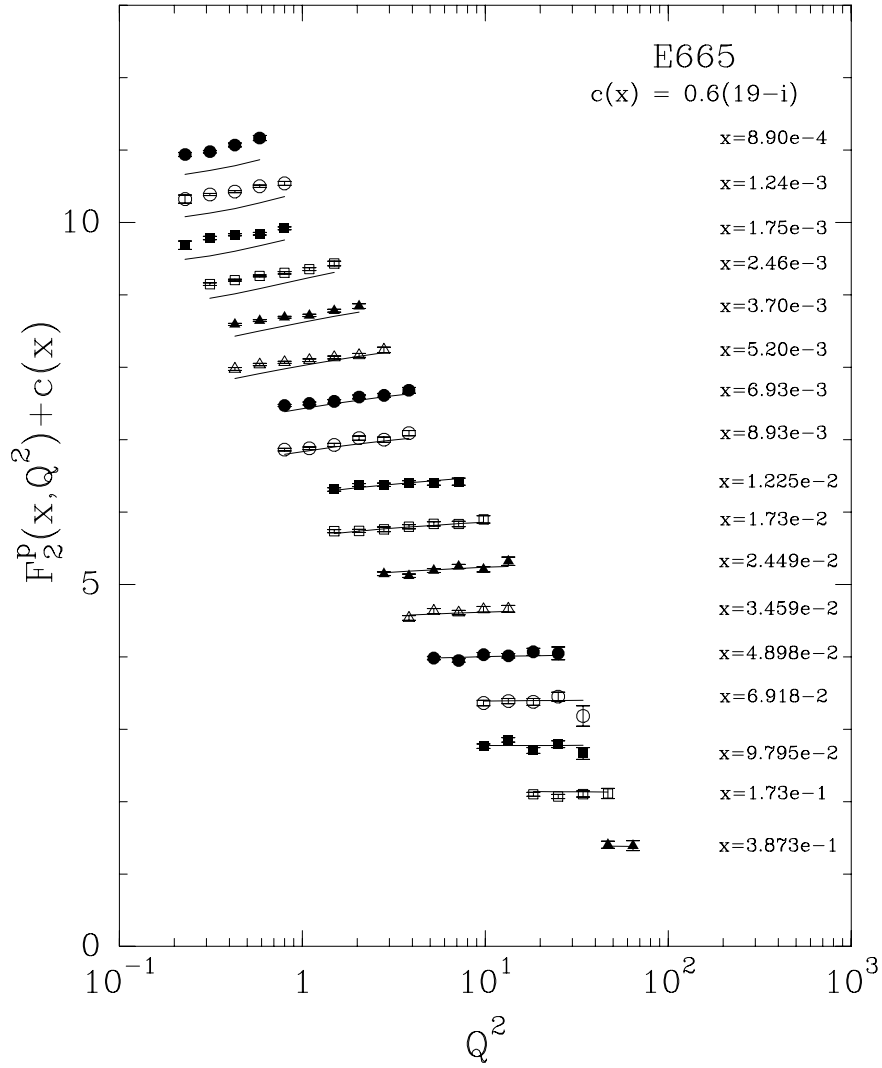


Figure 35: $F_2^p(x, Q^2)$ as function of Q^2 for fixed x , E665 data [23]. The function $c(x_i) = 0.6(19 - i)$, $i = 1$ corresponds to $x = 8.9 \cdot 10^{-4}$.

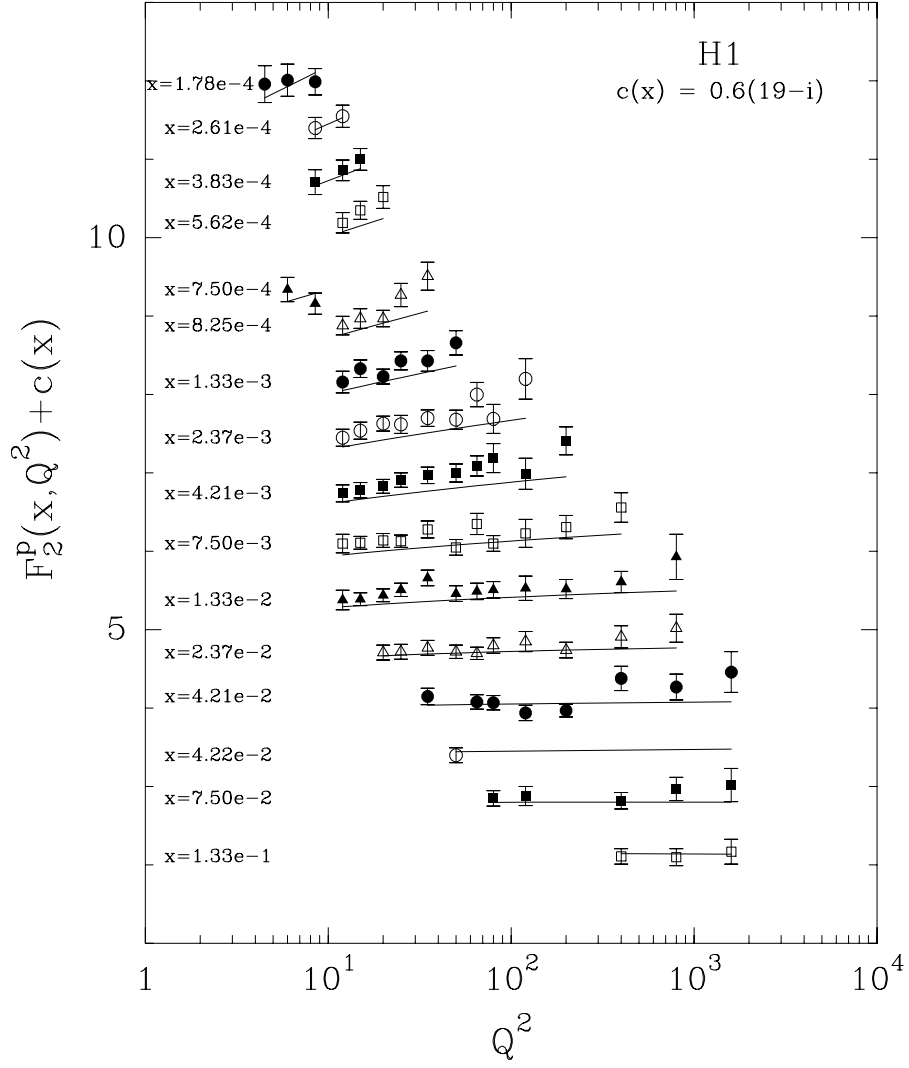


Figure 36: $F_2^p(x, Q^2)$ as function of Q^2 for fixed x , H1 data [37, 38]. The function $c(x_i) = 0.6(19 - i)$, $i = 1$ corresponds to $x = 1.78 \cdot 10^{-4}$.

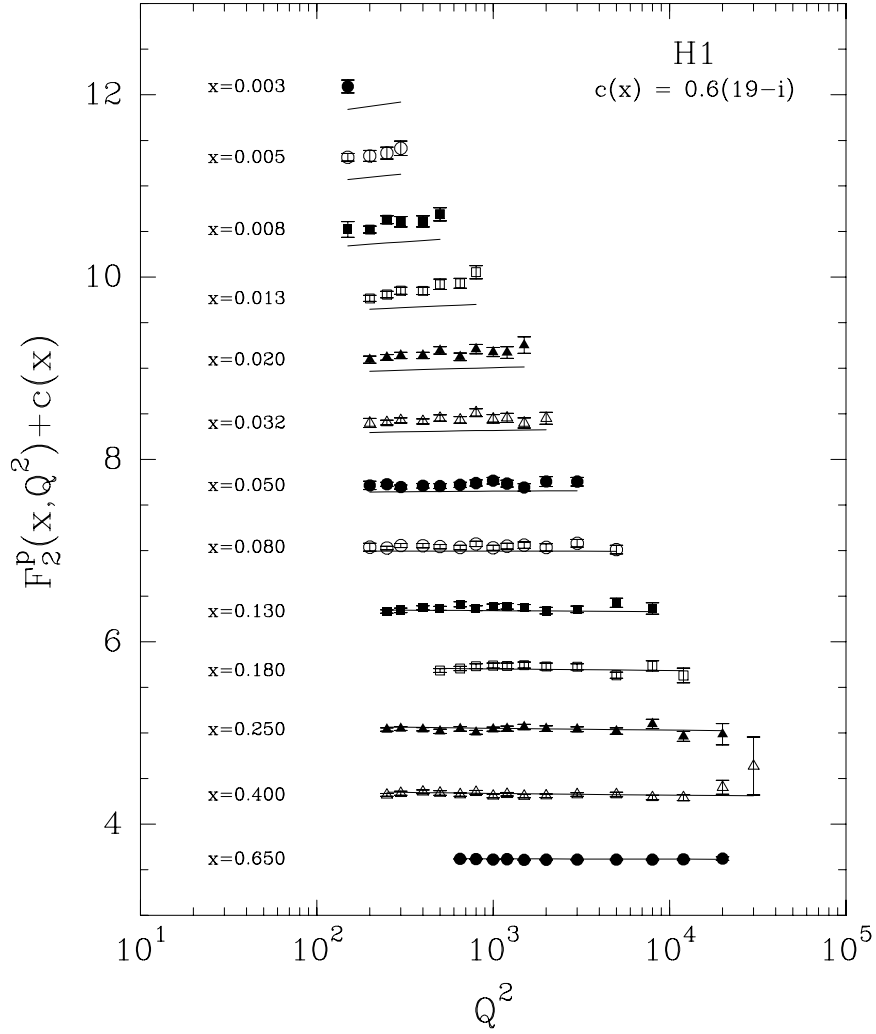


Figure 37: $F_2^p(x, Q^2)$ as function of Q^2 for fixed x , H1 Coll. The function $c(x_i) = 0.6(19 - i)$, $i = 1$ corresponds to $x = 0.003$.

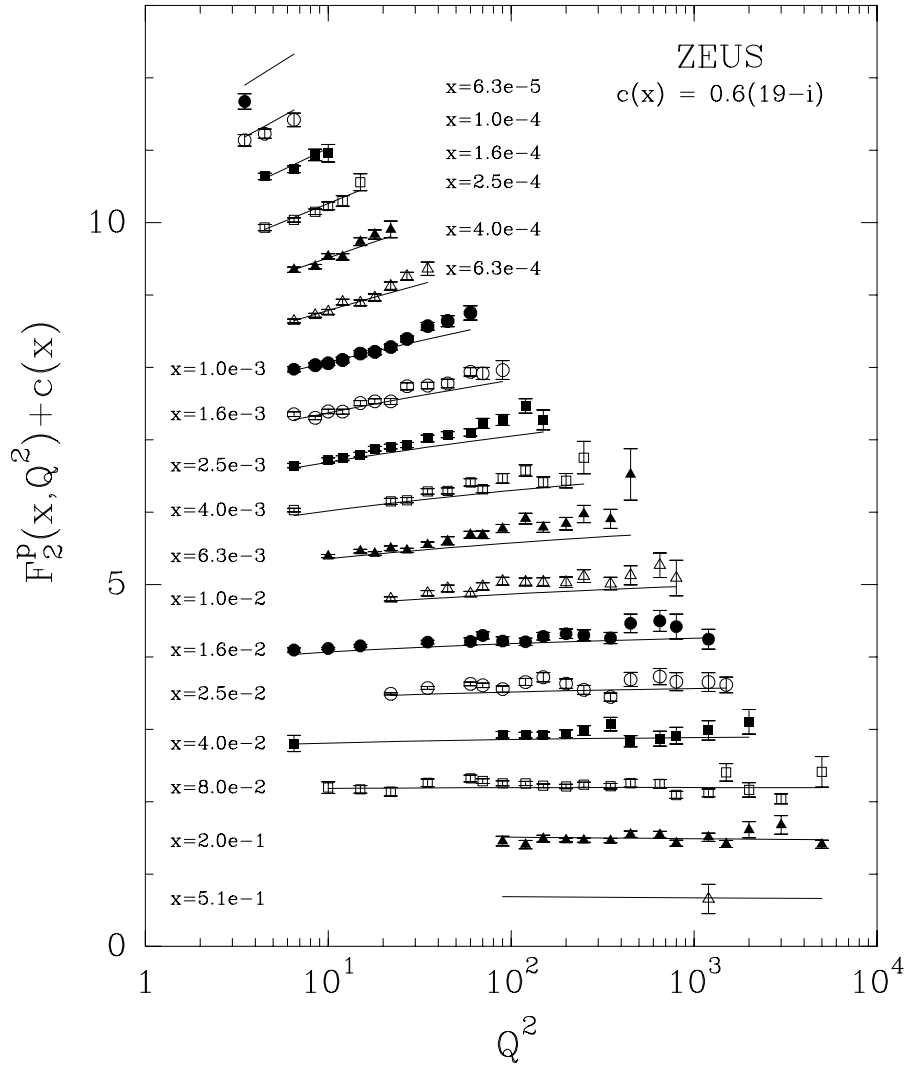


Figure 38: $F_2^p(x, Q^2)$ as function of Q^2 for fixed x , ZEUS data [92, 93]. The function $c(x_i) = 0.6(19 - i)$, $i = 1$ corresponds to $x = 6.3 \cdot 10^{-5}$.

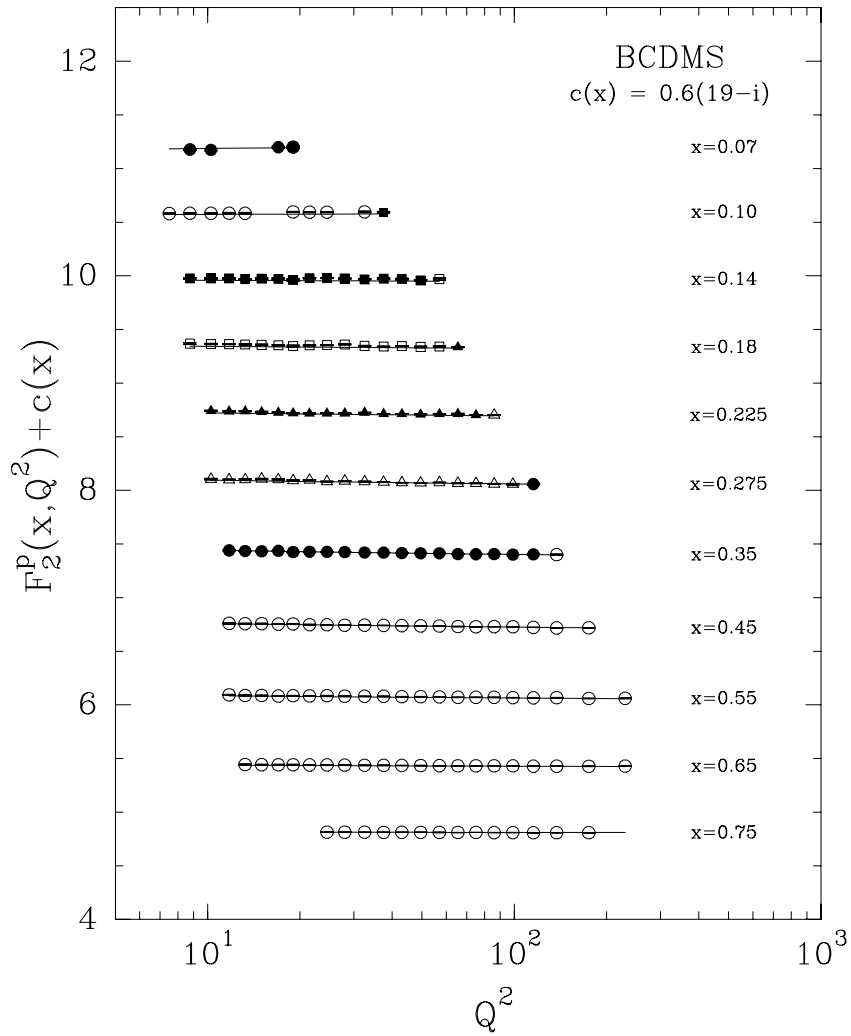


Figure 39: $F_2^p(x, Q^2)$ as function of Q^2 for fixed x , BCDMS Coll. [11, 12]. The function $c(x_i) = 0.6(19 - i)$, $i = 1$ corresponds to $x = 0.07$

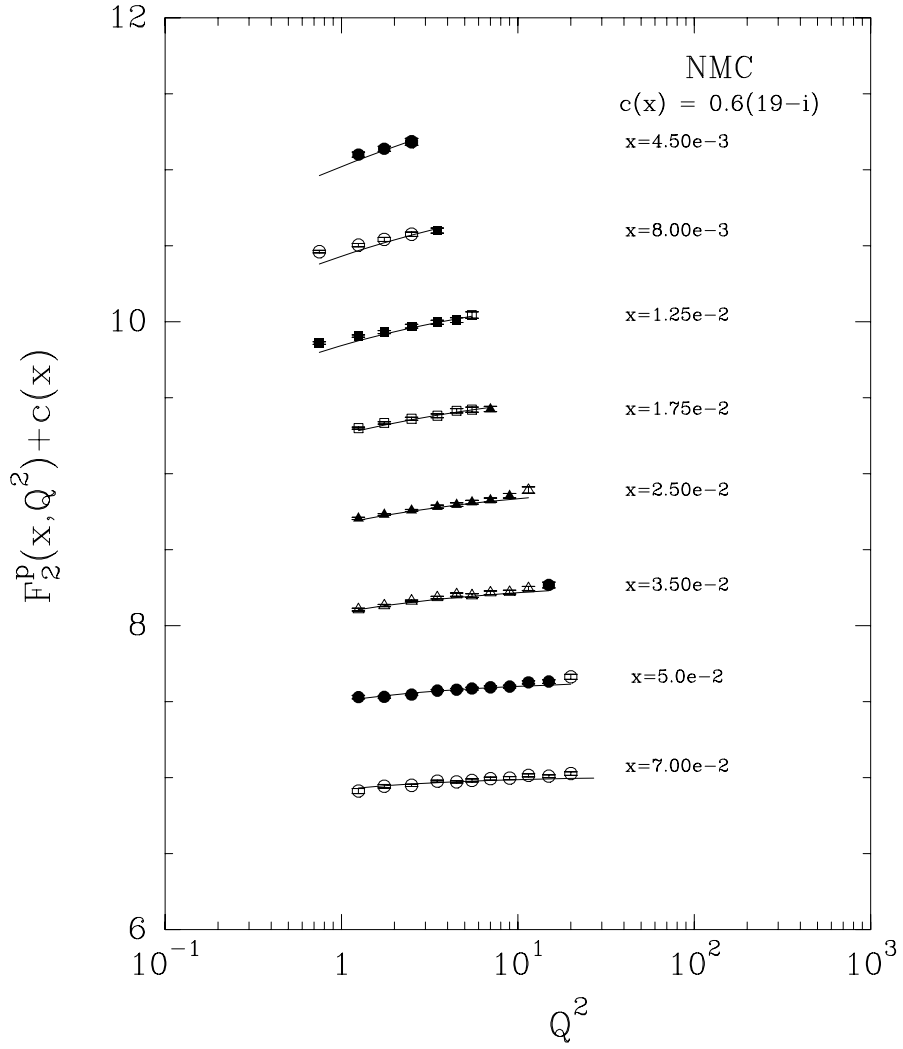


Figure 40: $F_2^p(x, Q^2)$ as function of Q^2 for fixed x , NMC Coll. The function $c(x_i) = 0.6(19 - i)$, $i = 1$ corresponds to $x = 4.5 \cdot 10^{-3}$.

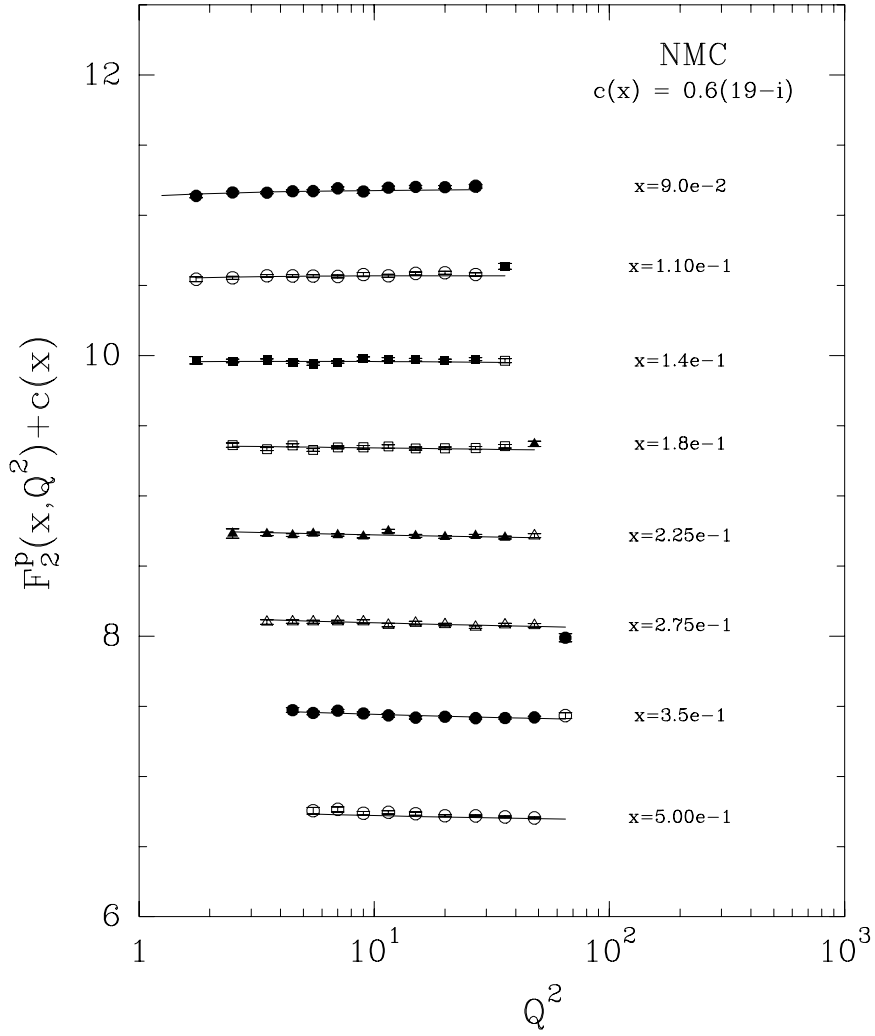


Figure 41: $F_2^p(x, Q^2)$ as function of Q^2 for fixed x , NMC Coll. The function $c(x_i) = 0.6(19 - i)$, $i = 1$ corresponds to $x = 9 \cdot 10^{-2}$.

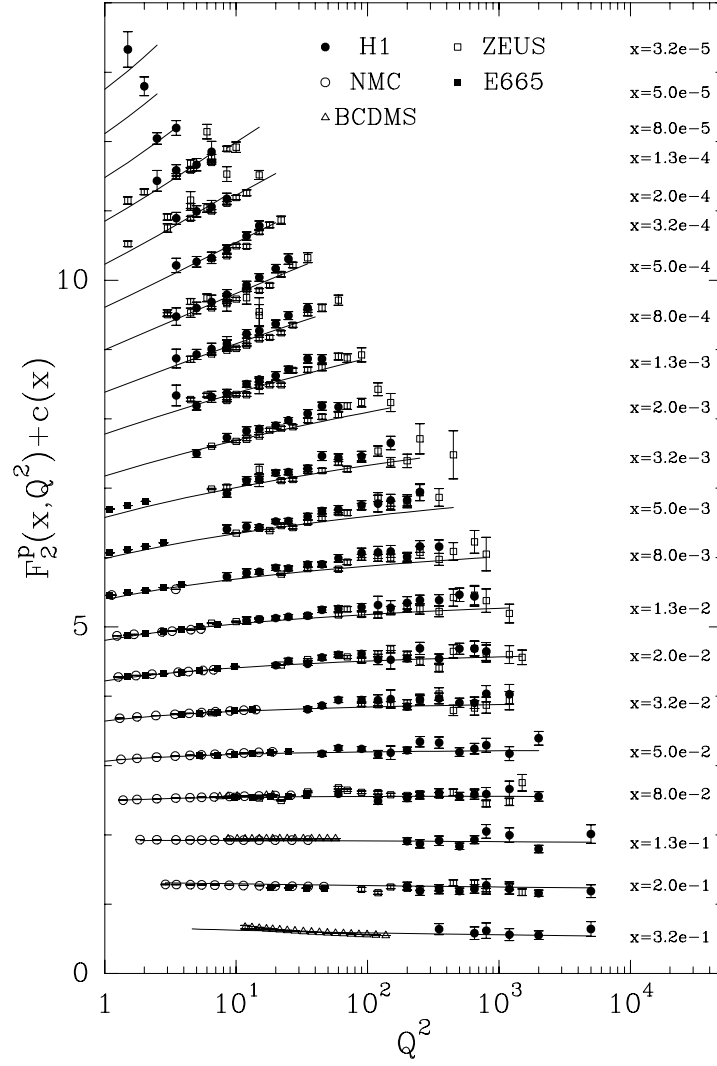


Figure 42: $F_2^p(x, Q^2)$ as function of Q^2 for fixed x , $c(x) = 0.6(i_x - 0.4)$, $i_x = 1 \rightarrow x = 0.32$, rebinned data H1, ZEUS, E665, NMC, BCDMS. (Presentation of data, courtesy of R. Voss).

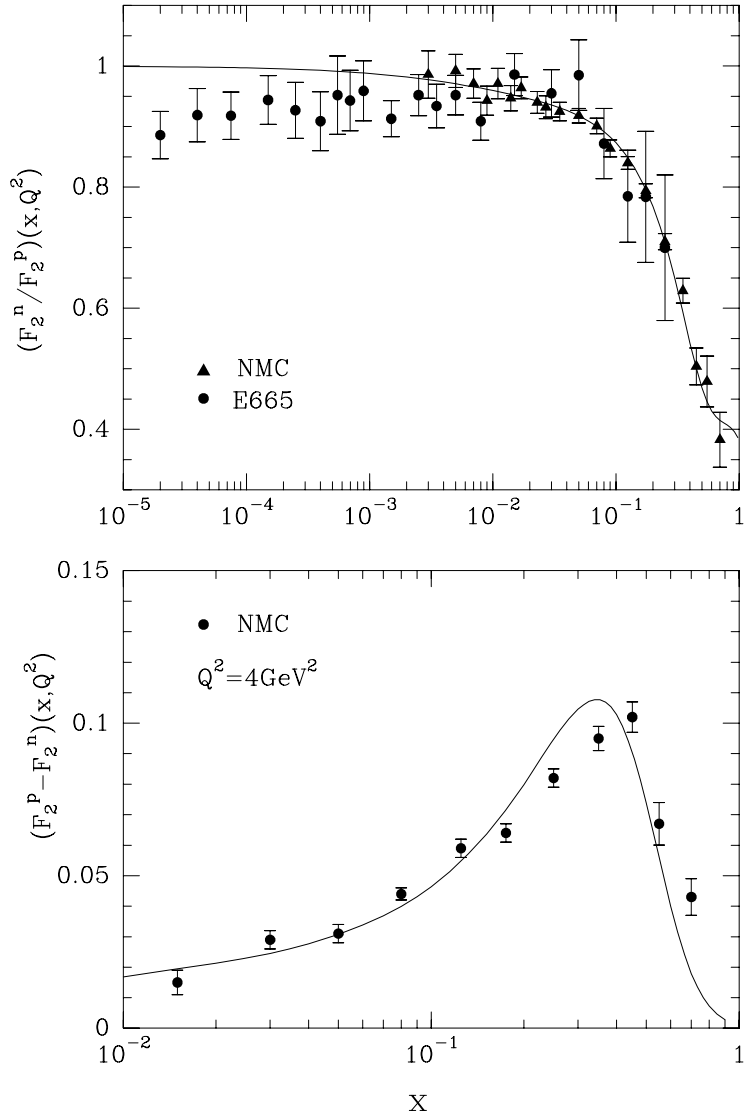


Figure 43: Ratio F_2^n/F_2^p as a function of x for different Q^2 values, data are from NMC and E665 Coll. Difference $F_2^p - F_2^n$ as a function of x for $Q^2 = 4\text{GeV}^2$, data are from NMC Coll.. The curves are shown for $Q^2 = 4\text{GeV}^2$.

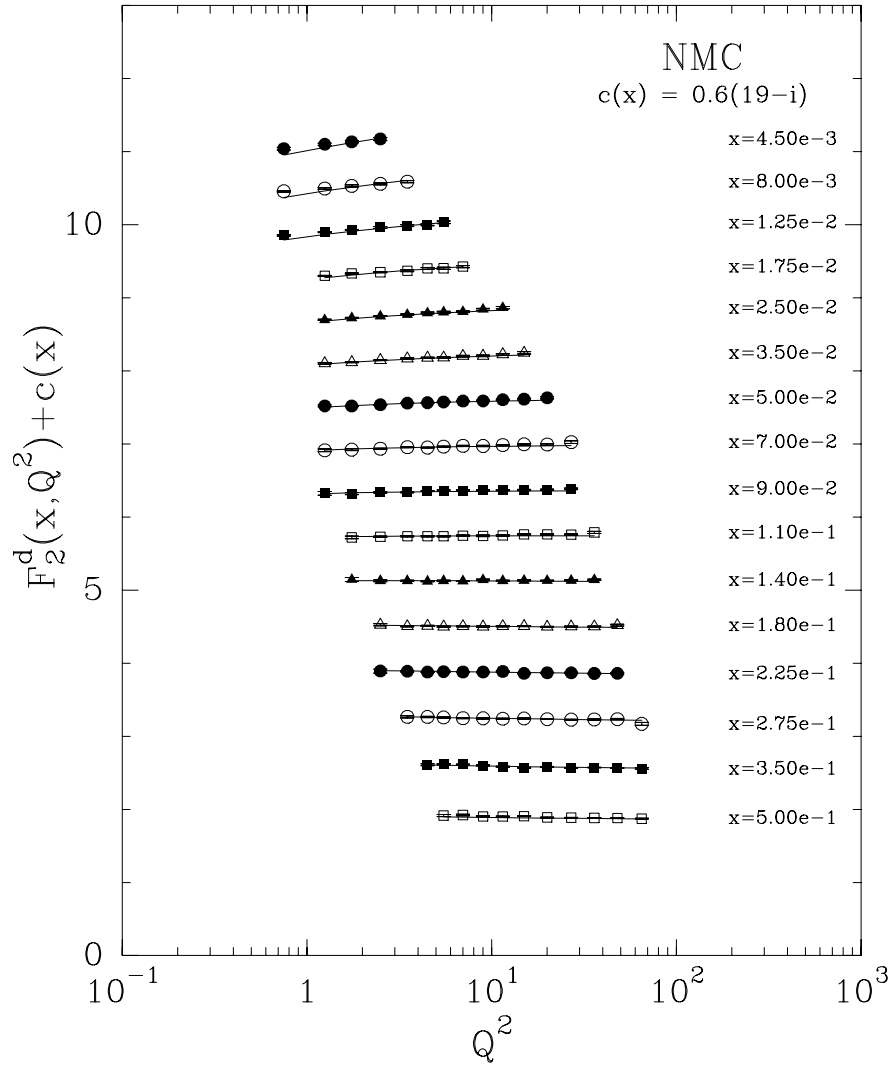


Figure 44: $F_2^d(x, Q^2)$ as function of Q^2 for fixed x , NMC data [58]. The function $c(x_i) = 0.6(19 - i)$, $i = 1$ corresponds to $x = 4.5 \cdot 10^{-3}$.

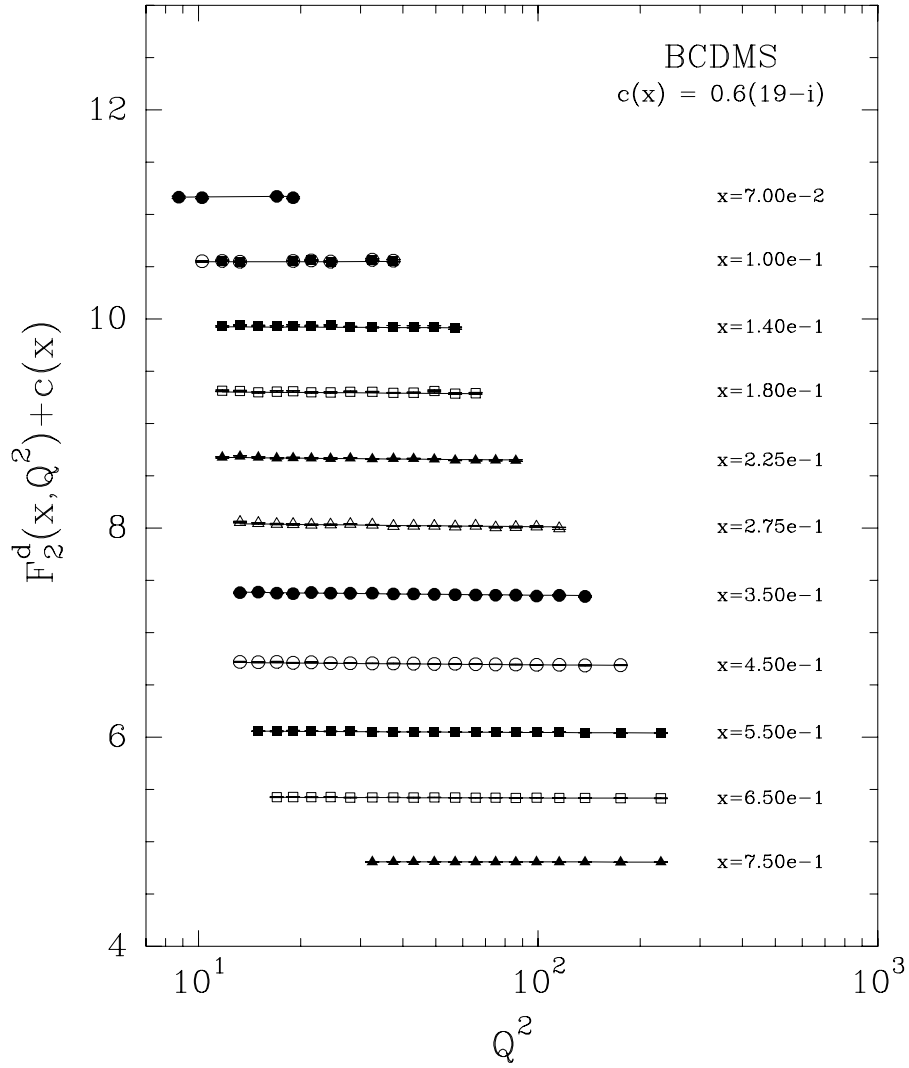


Figure 45: $F_2^d(x, Q^2)$ as function of Q^2 for fixed x , BCDMS data [12]. The function $c(x_i) = 0.6(19 - i)$, $i = 1$ corresponds to $x = 7 \cdot 10^{-2}$.

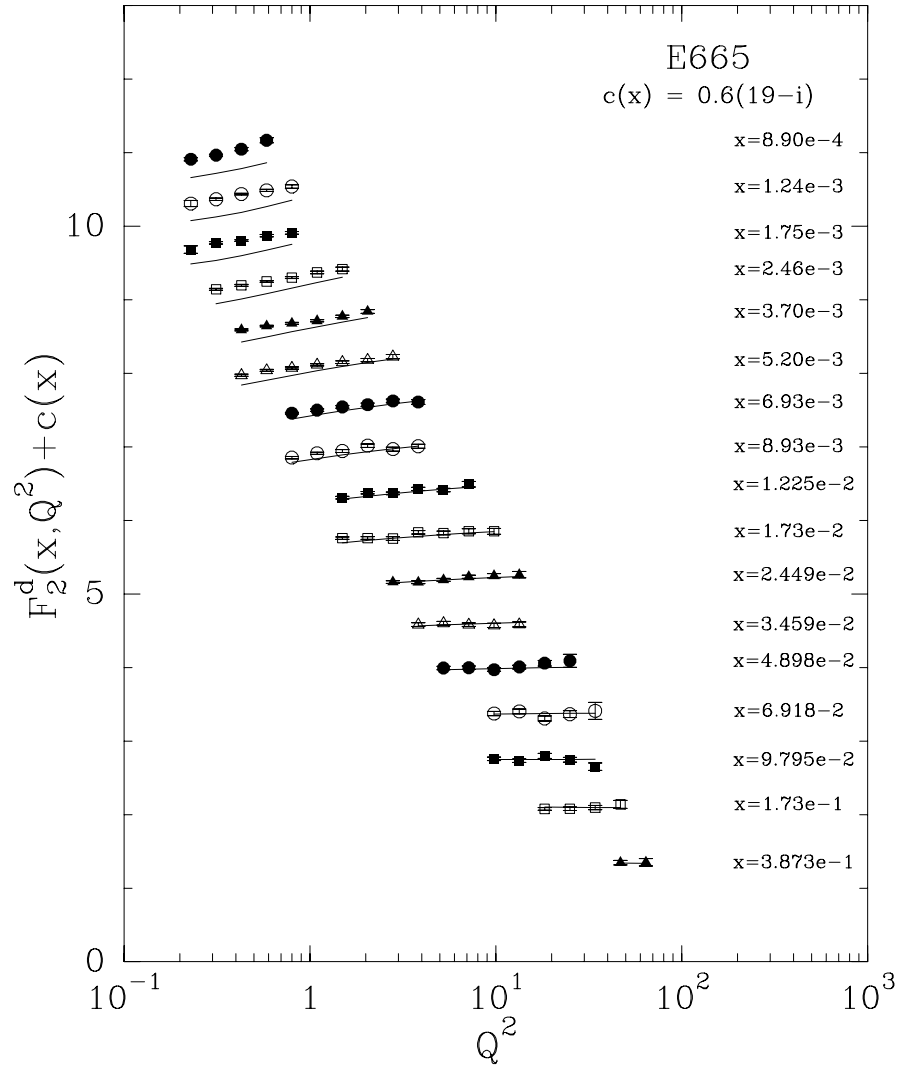


Figure 46: $F_2^d(x, Q^2)$ as function of Q^2 for fixed x , E665 data [23]. The function $c(x_i) = 0.6(19 - i)$, $i = 1$ corresponds to $x = 8.9 \cdot 10^{-4}$.

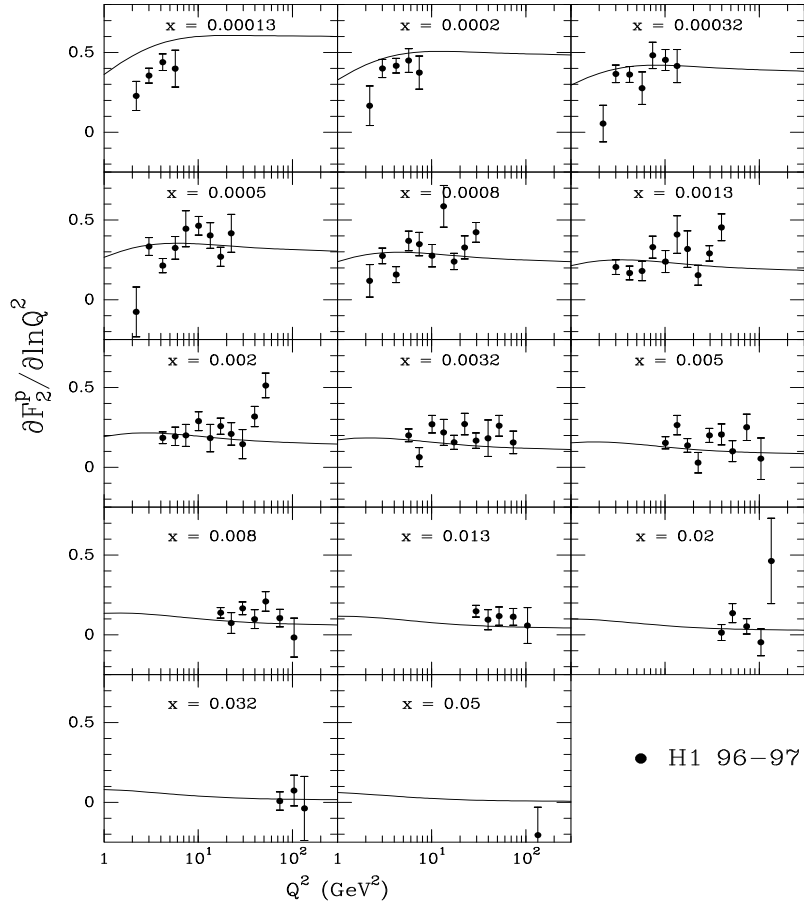


Figure 47: Prediction of the partial derivative $\partial F_2^p(x, Q^2)/\partial \ln(Q^2)$ for fixed x as a function of Q^2 . Data from H1 Collaboration [111].

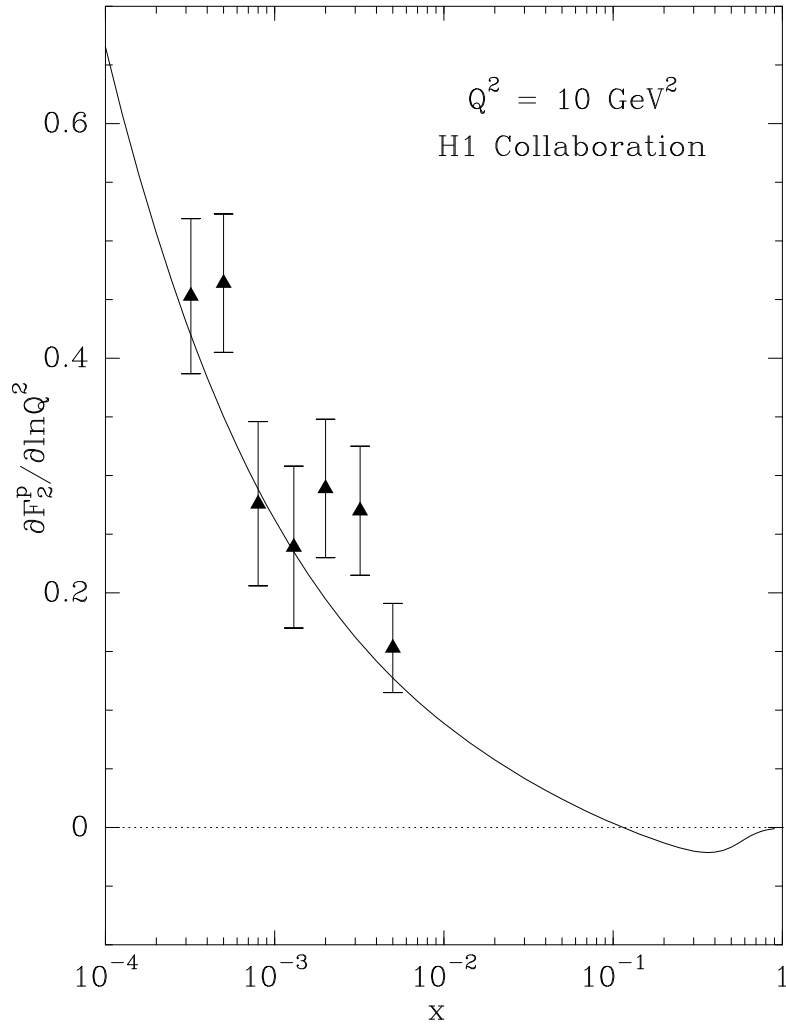


Figure 48: Prediction of the partial derivative $\partial F_2^p(x, Q^2)/\partial \ln(Q^2)$ for $Q^2 = 10\text{GeV}^2$ as a function of x . Data from H1 Collaboration [111].

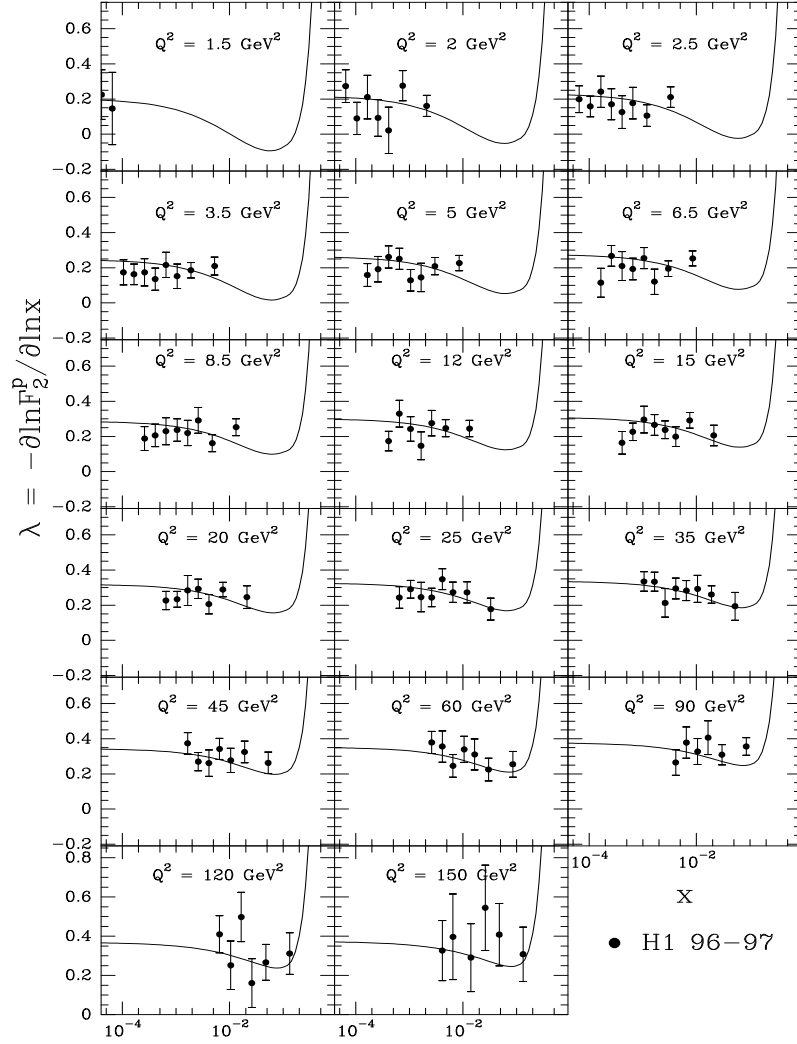


Figure 49: Prediction of the partial derivative $-\partial \ln F_2^p(x, Q^2)/\partial \ln(x)$ for fixed Q^2 as a function of x . Data from H1 Collaboration [112].

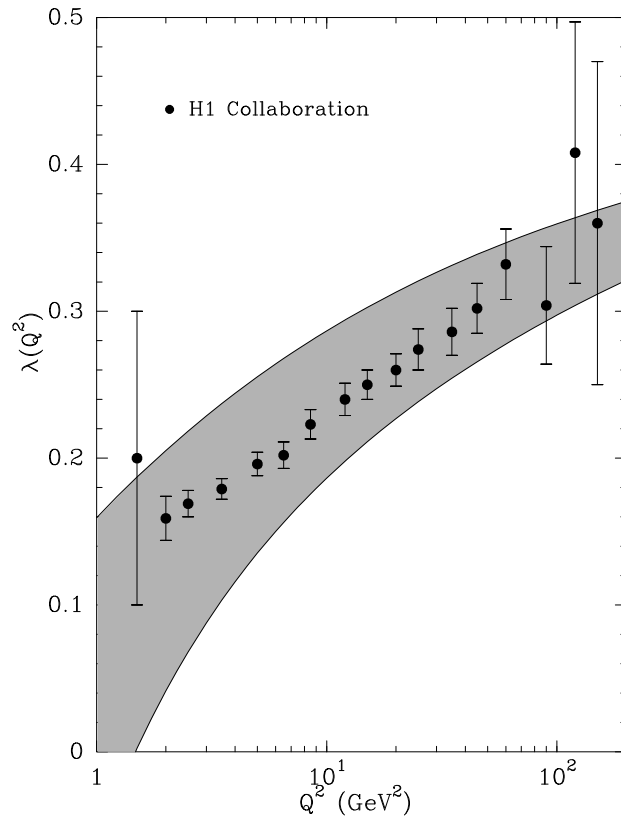


Figure 50: F_2^p partial derivative $\lambda(x, Q^2)$ as a function of Q^2 , the shaded surface represents the allowed domain for $10^{-4} \leq x \leq 10^{-2}$, predicted by the statistical model. Data from H1 Collaboration [112].

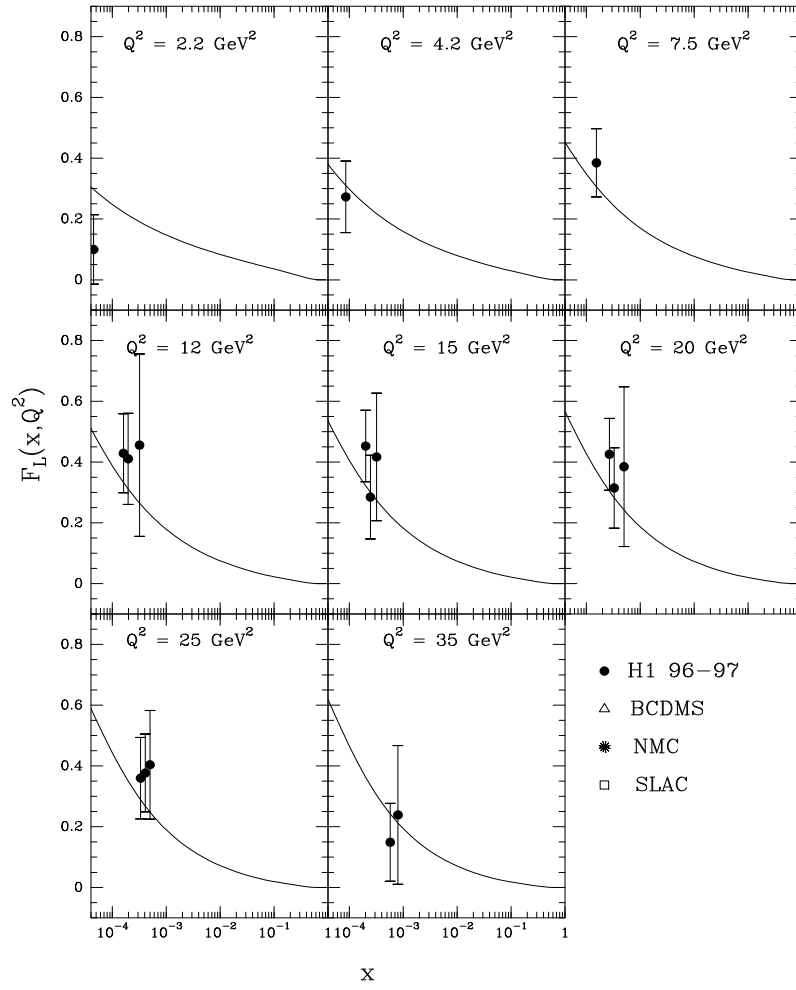


Figure 51: Prediction of the structure function F_L for different Q^2 as a function of x . Data from H1 Collaboration [111].

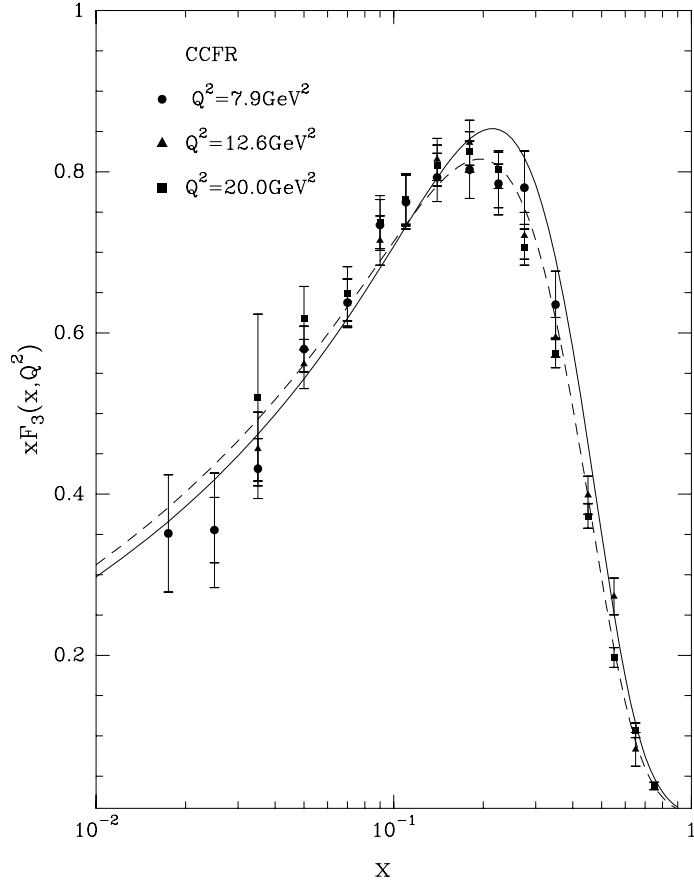


Figure 52: $xF_3^{\nu N}(x, Q^2)$ as function of x for low Q^2 values, CCFR Coll. The curves are for $Q^2 = 4, 12.6\text{GeV}^2$, solid, dashed respectively.

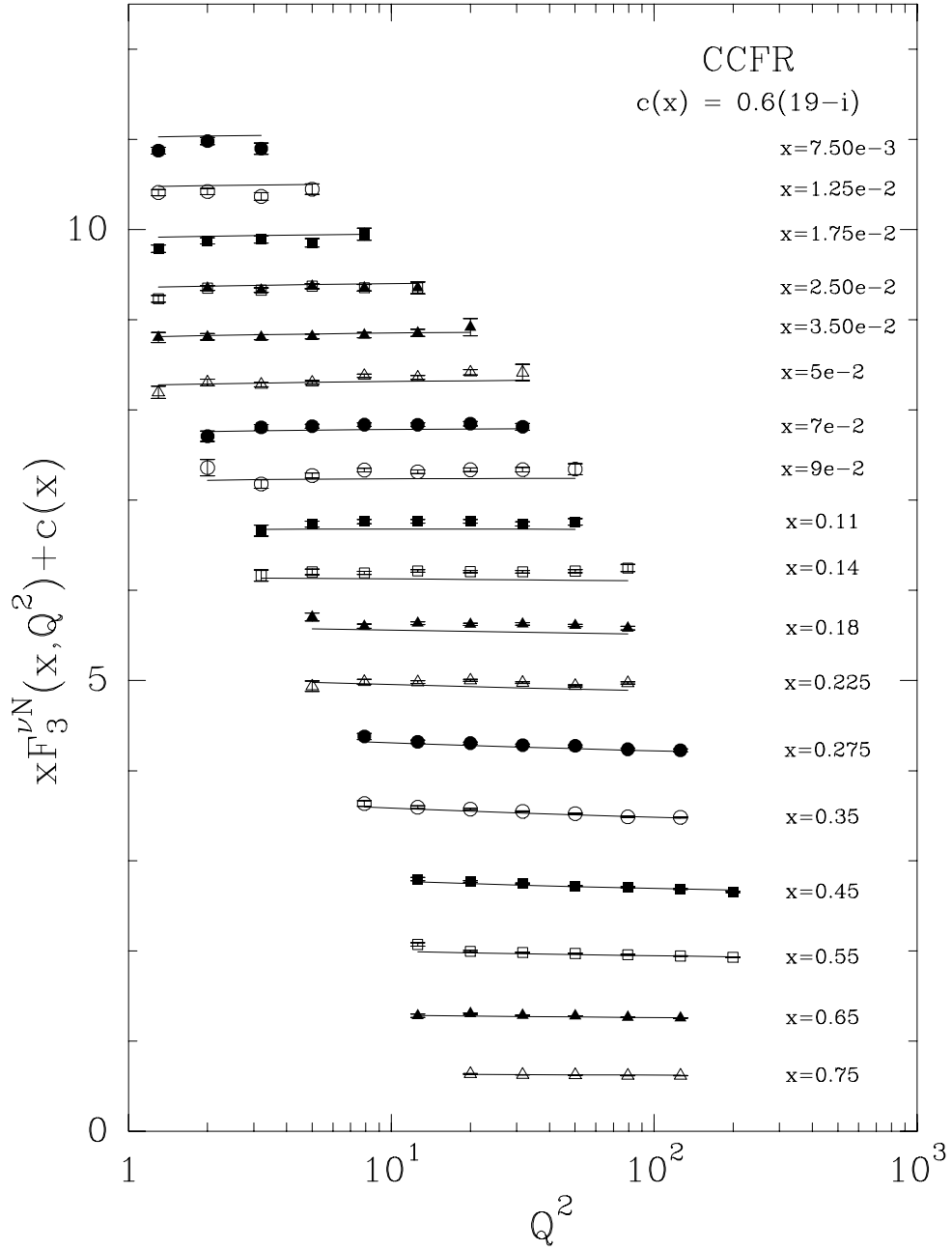


Figure 53: $xF_3^{\nu N}(x, Q^2)$ as function of Q^2 for fixed x , CCFR data [13]. The function $c(x_i) = 0.6(19 - i)$, $i = 1$ corresponds to $x = 7.5 \cdot 10^{-3}$.

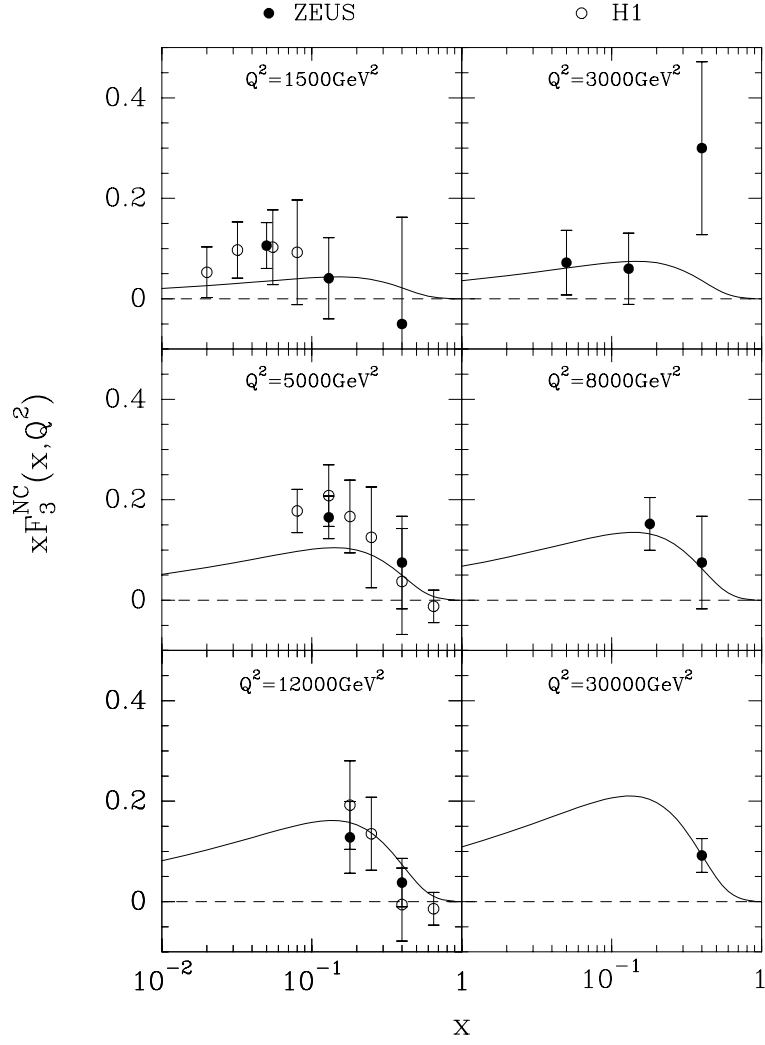


Figure 54: The structure function $x F_3^{NC}$ as a function of x , for different Q^2 . Data from ZEUS Coll. [95], H1 Coll. [40].

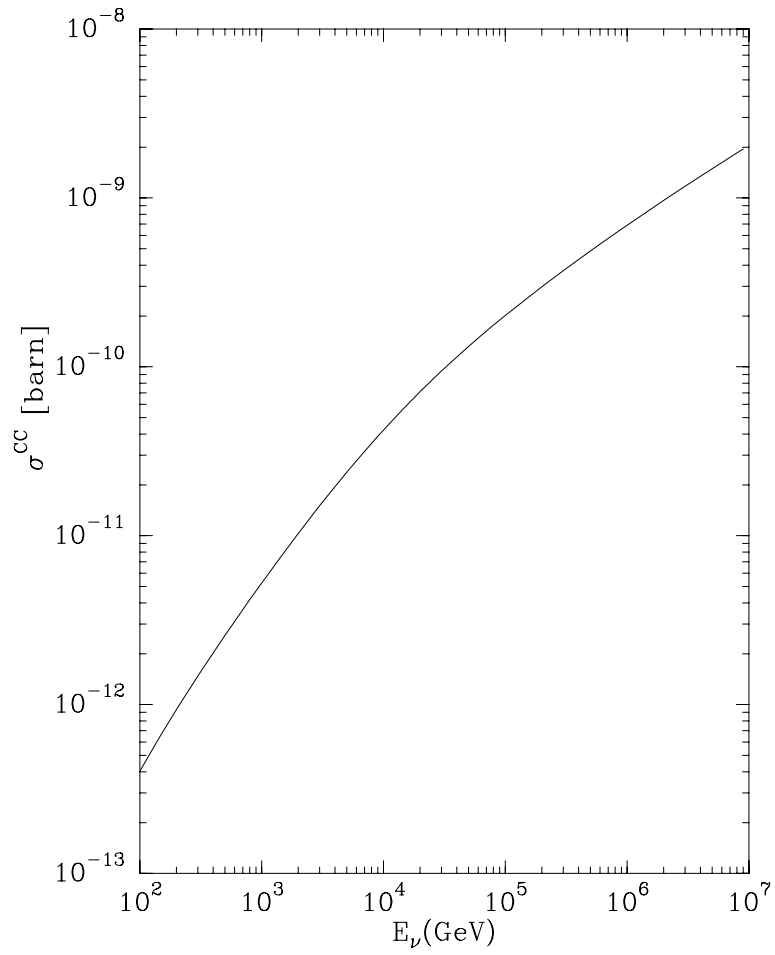


Figure 55: Charged-current total cross section νN for an isoscalar nucleon as a function of the neutrino energy.

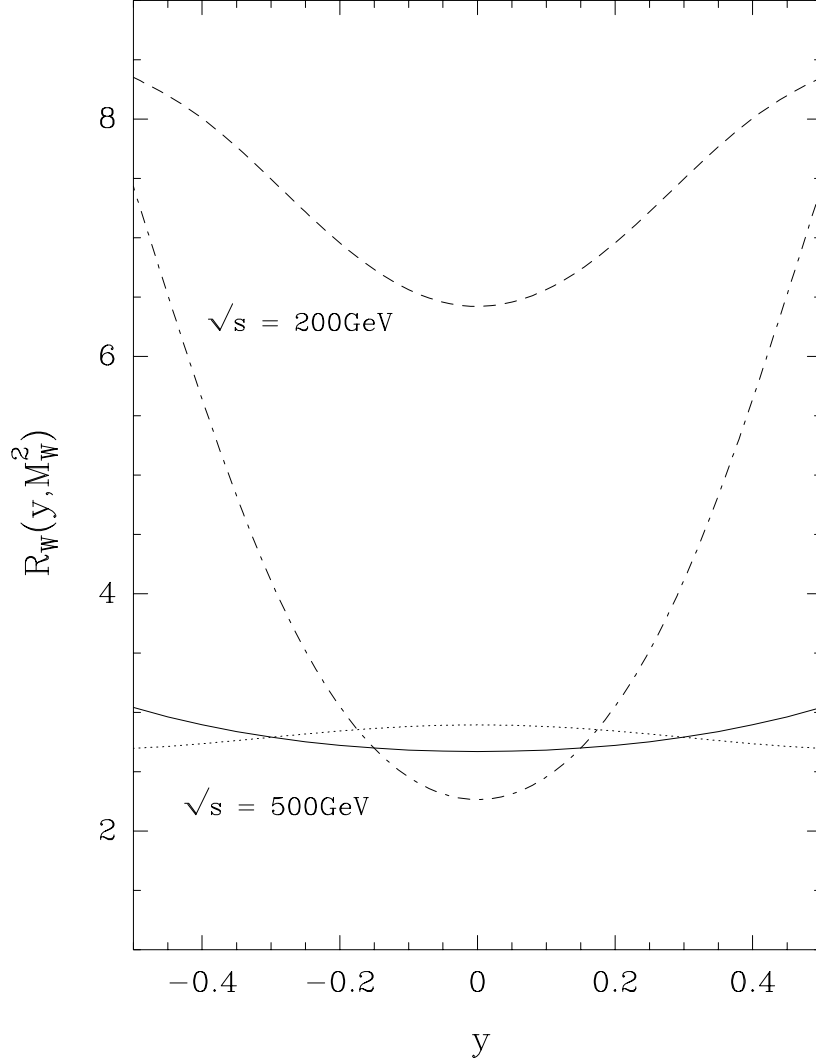


Figure 56: Theoretical calculations for the ratio $R_W(y) = (d\sigma^{W^+}/dy) / (d\sigma^{W^-}/dy)$ for pp versus the W rapidity, at two RHIC-BNL energies. Solid curve ($\sqrt{s} = 500 \text{ GeV}$) and dashed curve ($\sqrt{s} = 200 \text{ GeV}$) are the statistical model predictions. Dotted curve ($\sqrt{s} = 500 \text{ GeV}$) and dashed-dotted curve ($\sqrt{s} = 200 \text{ GeV}$) are the predictions obtained using the $\bar{d}(x)/\bar{u}(x)$ ratio from Ref. [84].

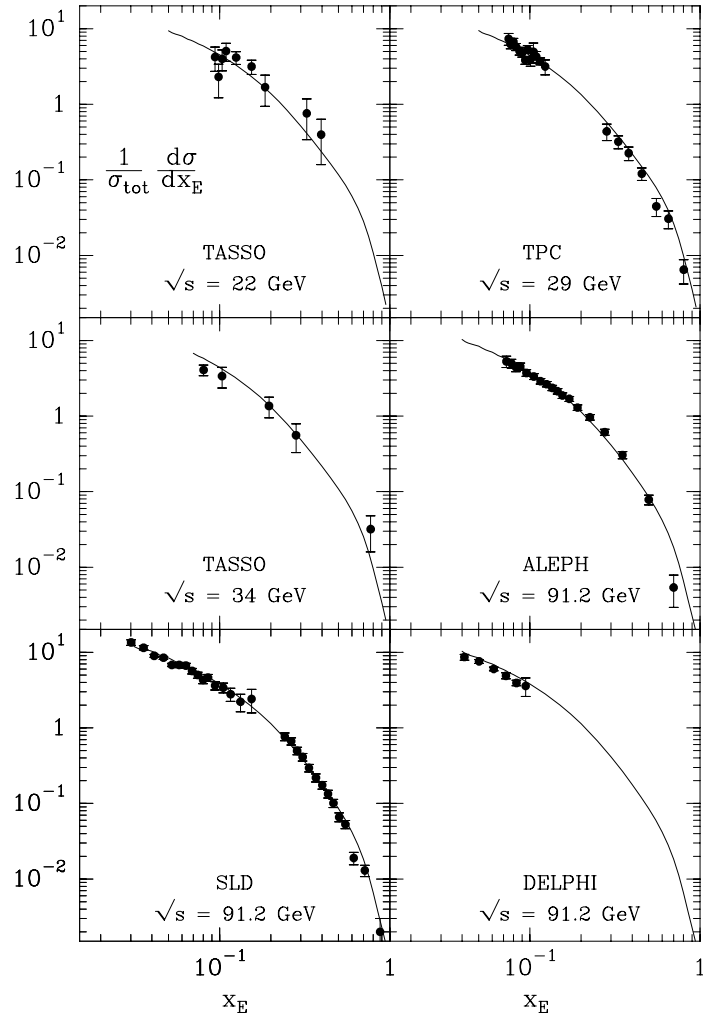


Figure 57: Cross sections for proton production in e^+e^- annihilation at several energies as function of x_E . The experimental data are from Refs. [8, 20, 79, 86, 90, 88].

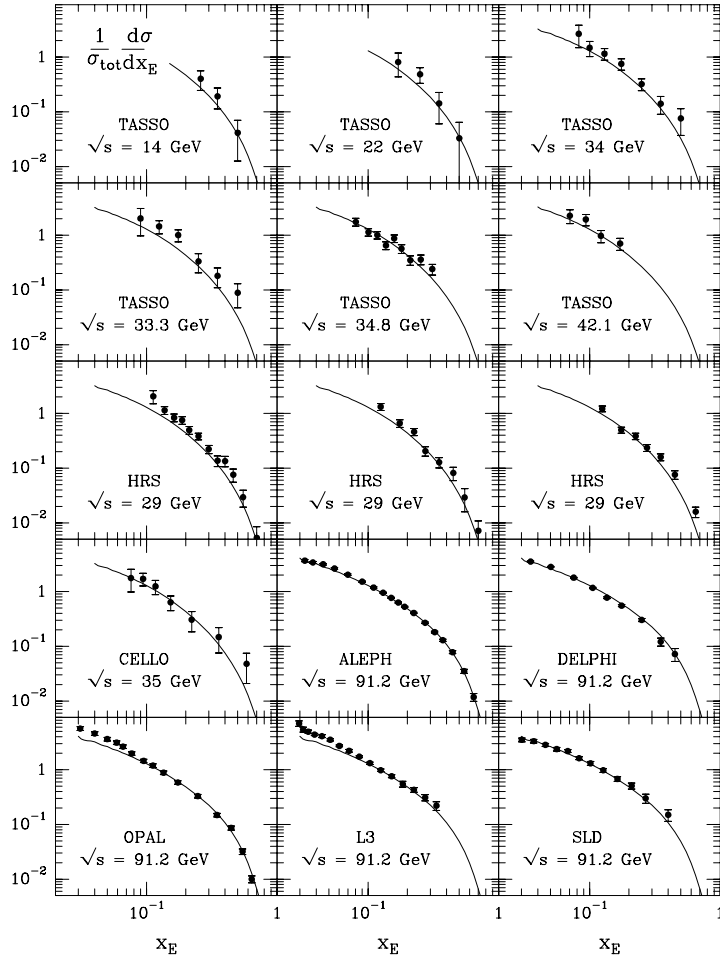


Figure 58: Cross sections for Λ production in e^+e^- annihilation at several energies, as function of x_E . The experimental data are from Refs. [15, 9, 21, 61, 55, 79, 85, 87, 89, 50, 51, 52].

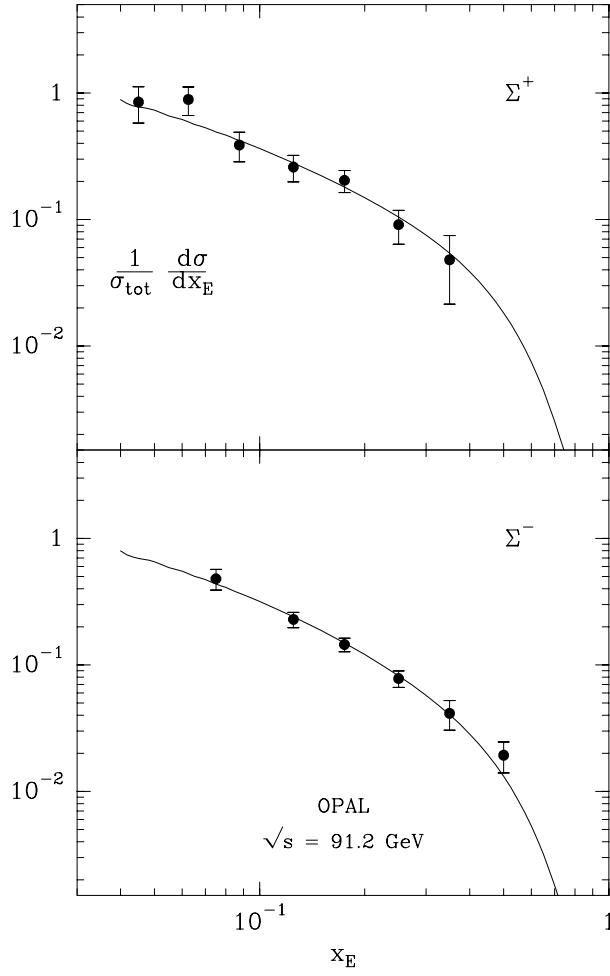


Figure 59: Cross sections for Σ^\pm production in e^+e^- annihilation at the Z-pole as function of x_E . The experimental data are from Ref. [61].

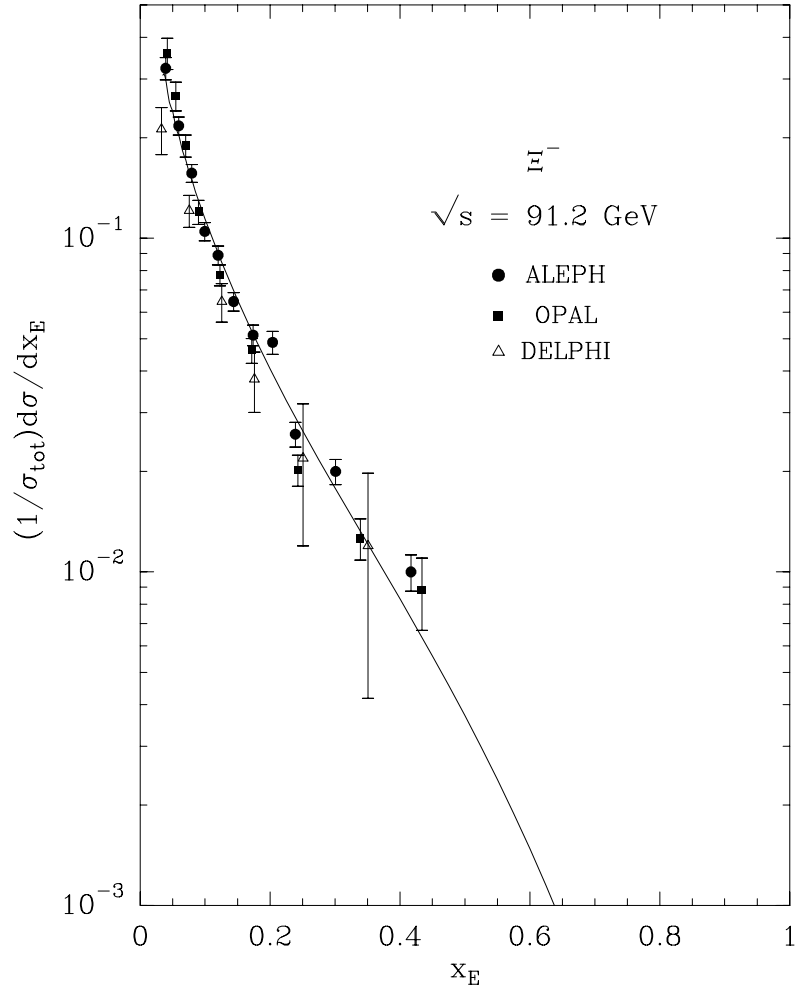


Figure 60: Cross sections for Ξ^- production in e^+e^- annihilation at the Z-pole as function of x_E . The experimental data are from Refs. [9, 61, 22].

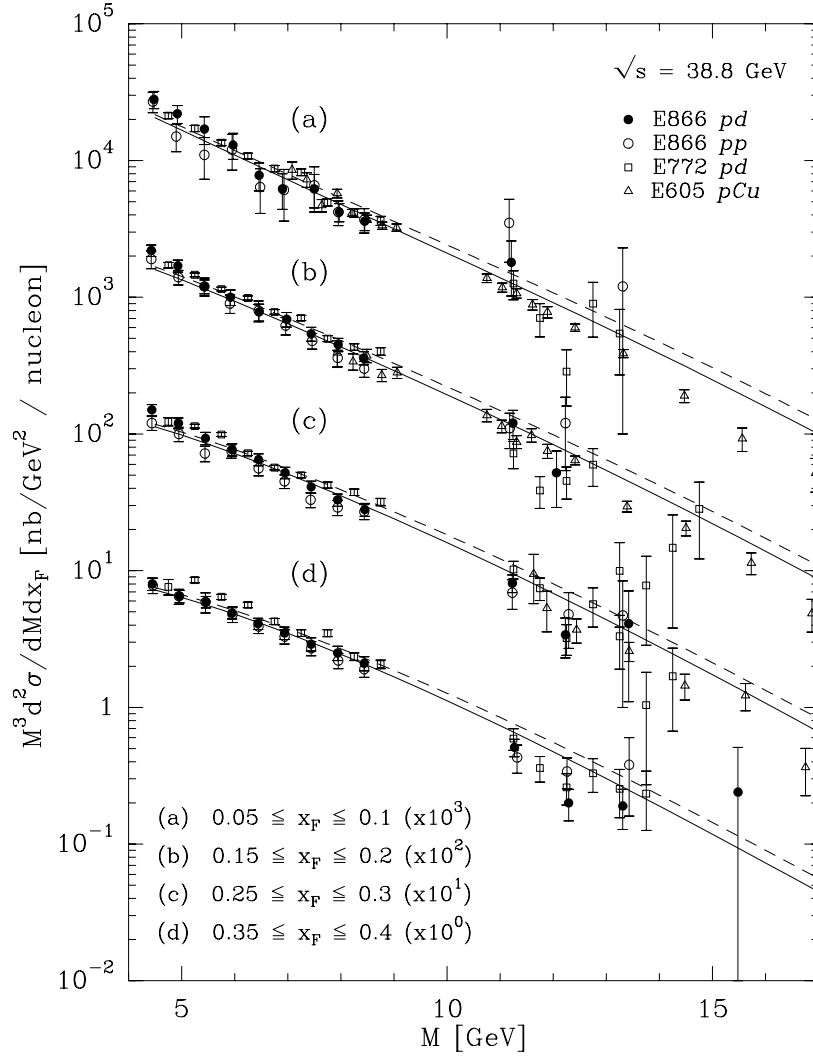


Figure 61: Drell-Yan cross sections per nucleon at $\sqrt{s} = 38.8 \text{ GeV}$ for *pp*, *pd*, and *pCu* as a function of M for selected x_F bins. Experimental data are from Refs. [26, 27, 28].

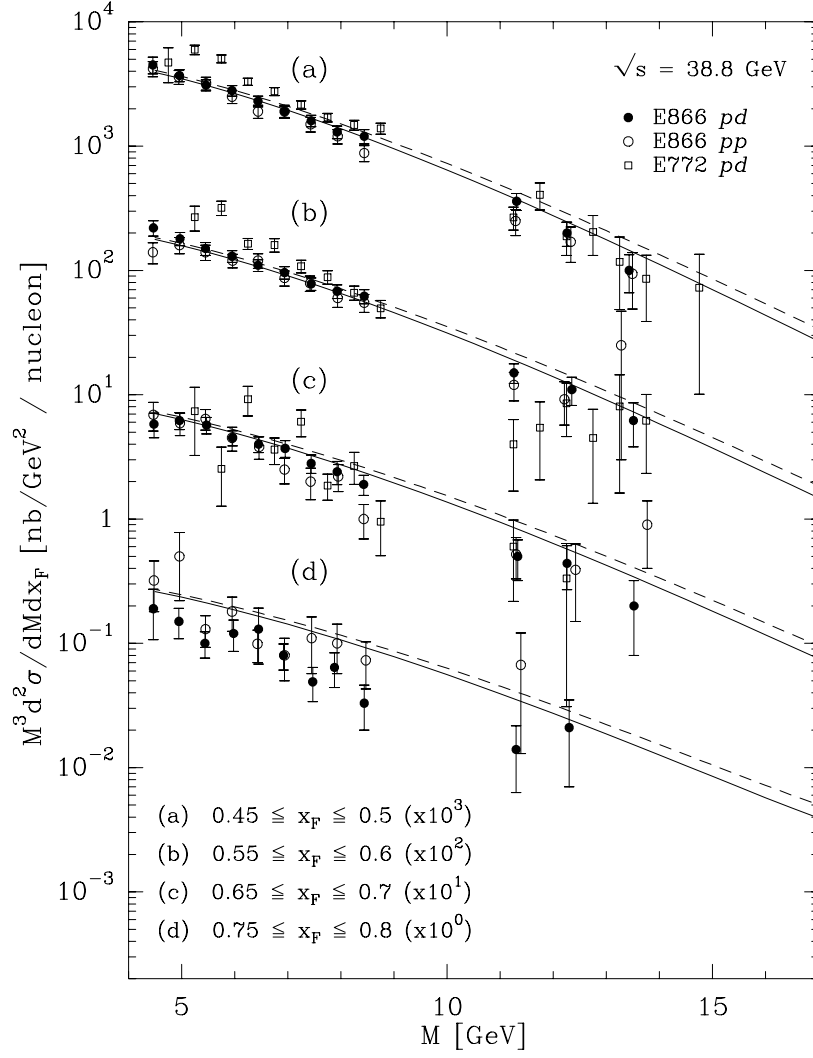


Figure 62: Drell-Yan cross sections per nucleon at $\sqrt{s} = 38.8 \text{ GeV}$ for *pp* and *pd* as a function of M for selected x_F bins. Experimental data are from Refs. [26, 27].

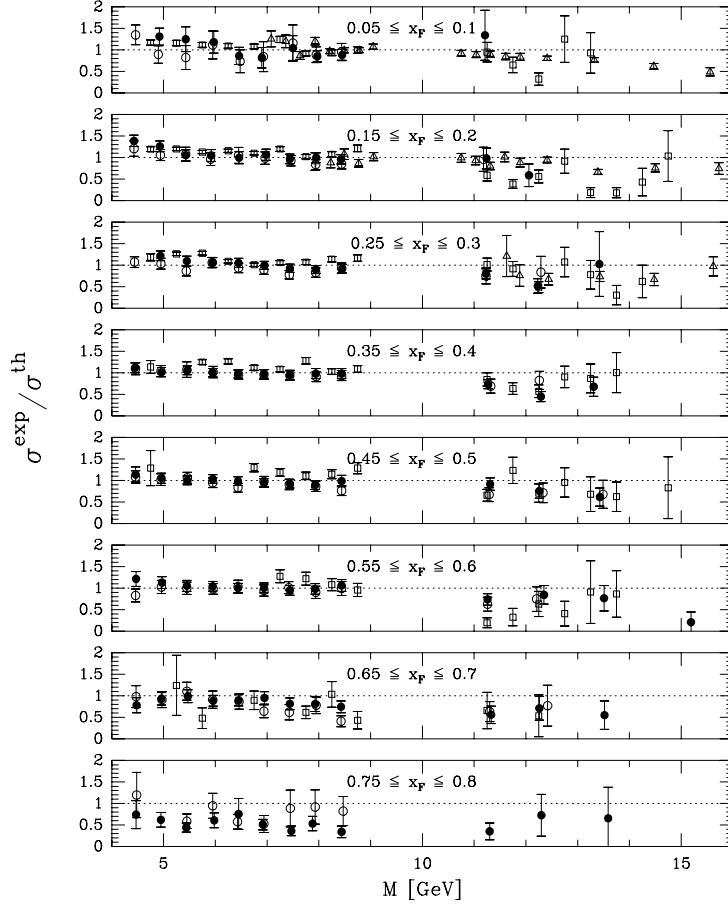


Figure 63: Drell-Yan cross sections ratios experiment vs theory at $\sqrt{s} = 38.8\text{GeV}$ for pp , pd , and pCu as a function of M for selected x_F bins. Experimental data are from Refs. [26, 27, 28].

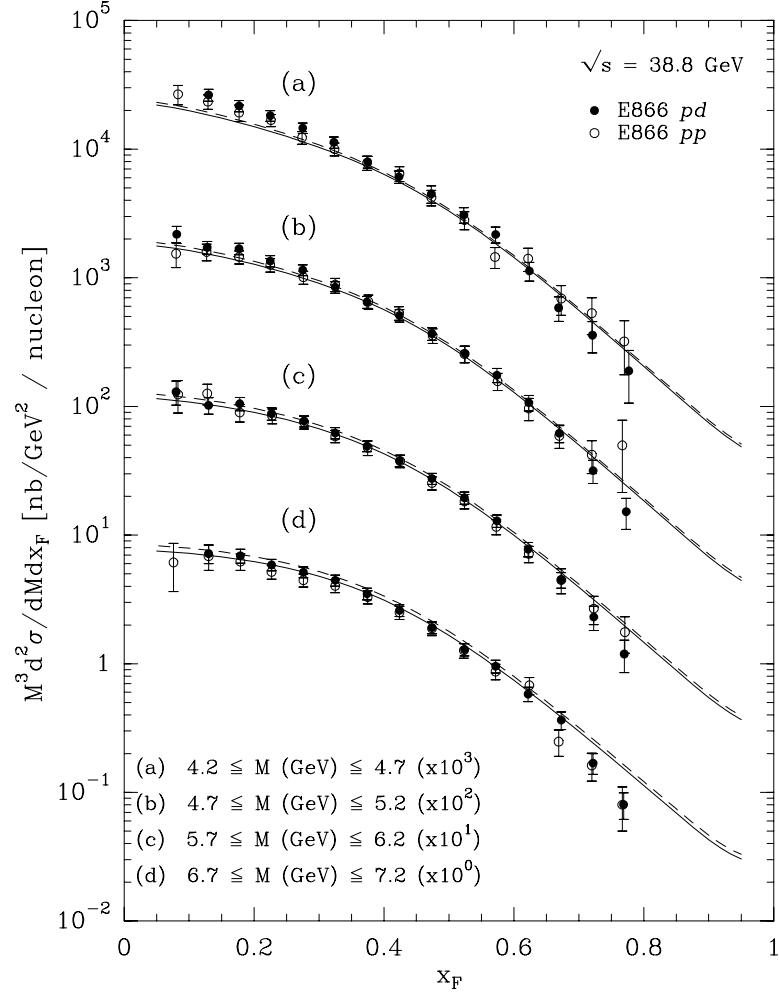


Figure 64: Drell-Yan cross sections per nucleon at $\sqrt{s} = 38.8\text{GeV}$ for *pp* and *pd* as a function of x_F for selected M bins. Experimental data are from Ref. [26].

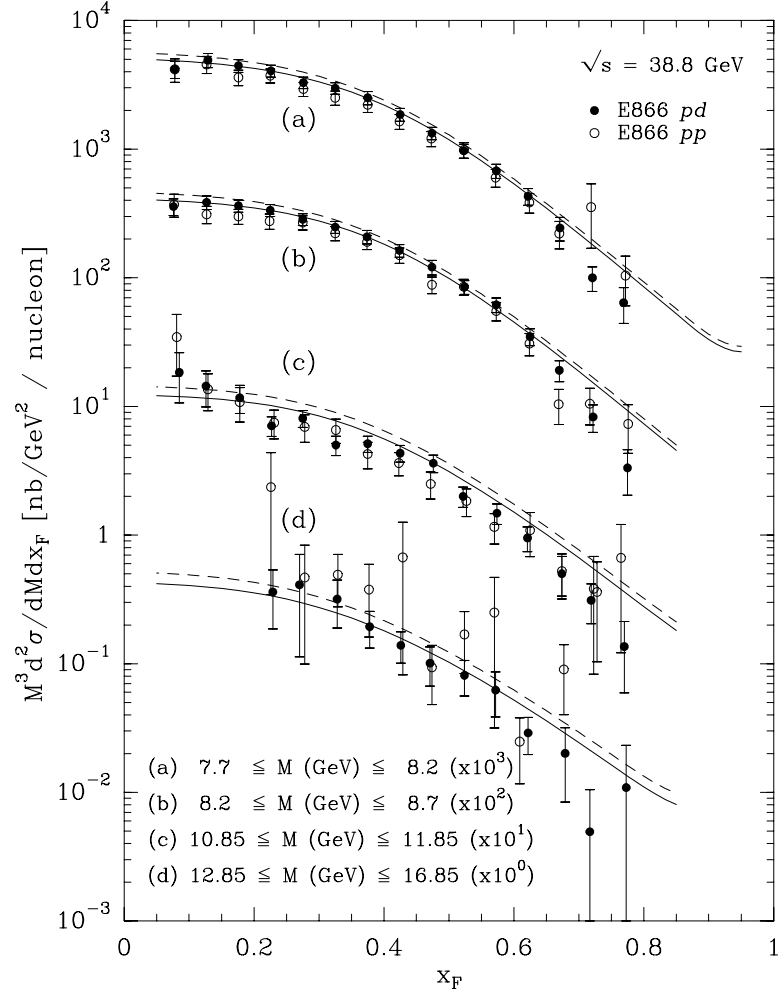


Figure 65: Drell-Yan cross sections per nucleon at $\sqrt{s} = 38.8 \text{ GeV}$ for *pp* and *pd* as a function of x_F for selected M bins. Experimental data are from Ref. [26].

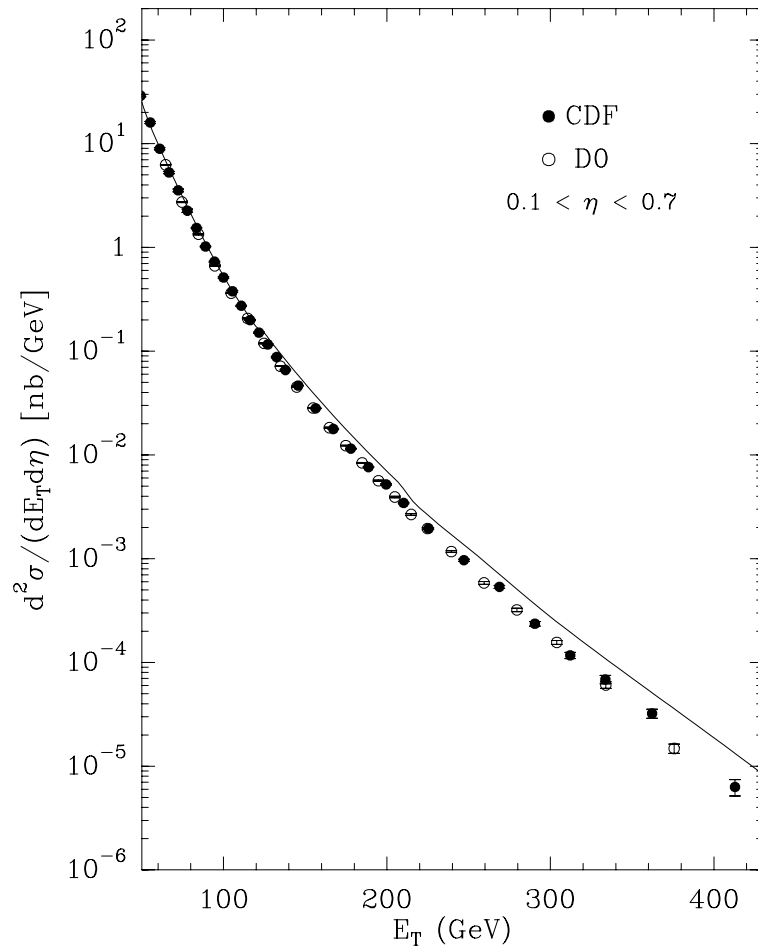


Figure 66: Cross section for single jet production in $\bar{p}p$ at $\sqrt{s} = 1.8\text{TeV}$ as a function of E_T . Data from CDF [17] and D0 [18] collaborations.

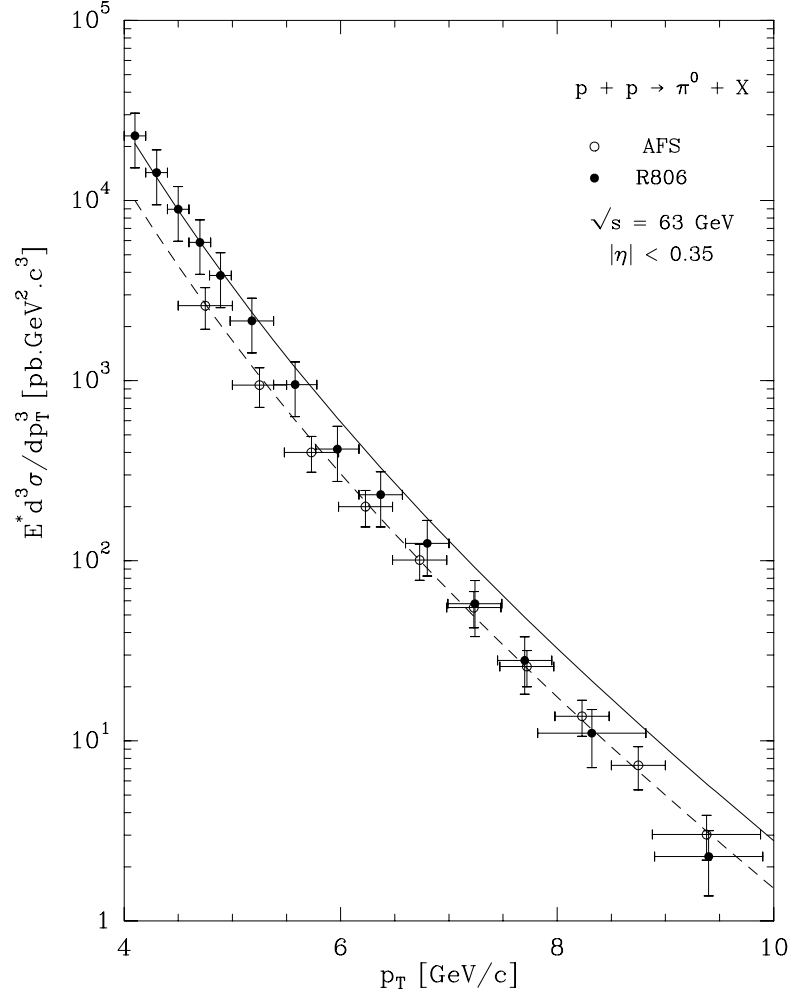


Figure 67: Inclusive π^0 production in pp reaction at $\sqrt{s} = 63\text{GeV}$ as a function of p_T . Data from AFS [7] and R806 [63] Collaborations. Solid curve scale $\mu = p_T/2$, dashed $\mu = p_T$, fragmentation functions from KKP [100].

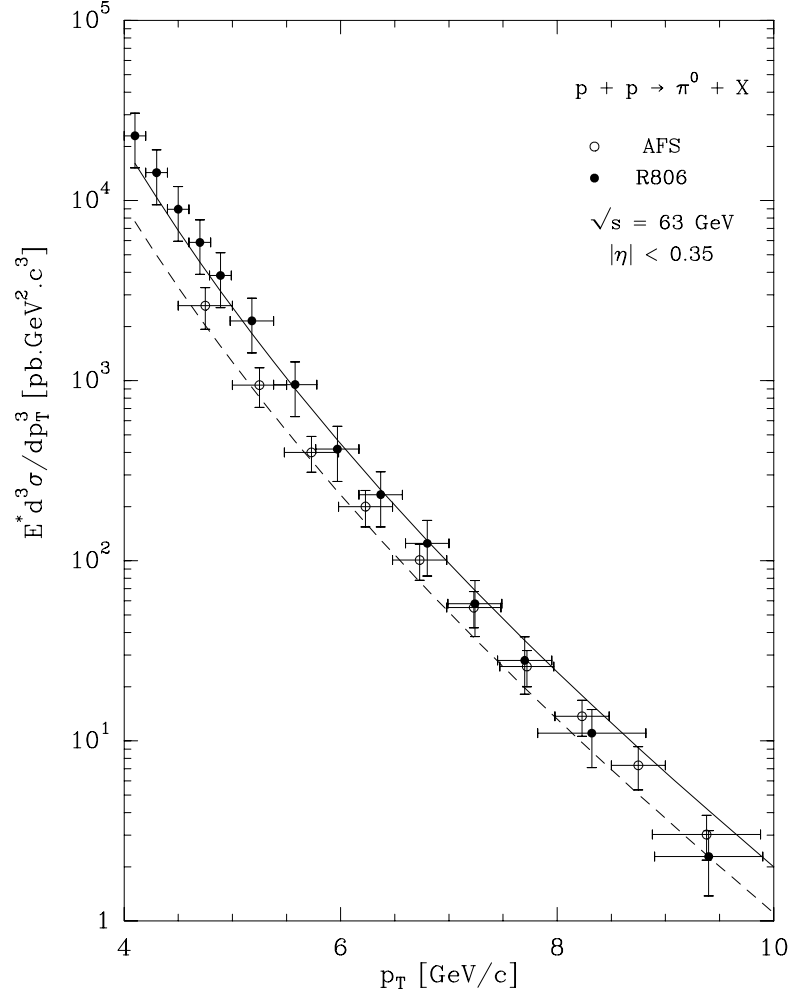


Figure 68: Inclusive π^0 production in pp reaction at $\sqrt{s} = 63\text{GeV}$ as a function of p_T . Data from AFS [7] and R806 [63] Collaborations. Solid curve scale $\mu = p_T/2$, dashed $\mu = p_T$, fragmentation functions BKP [101].

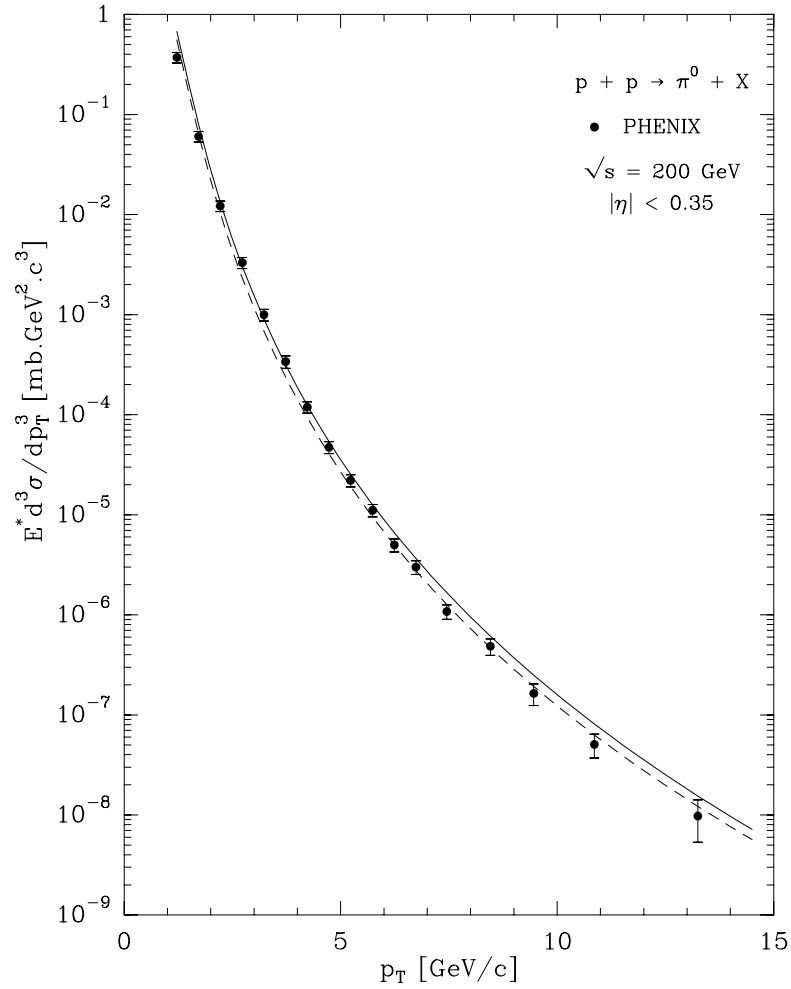


Figure 69: Inclusive π^0 production in pp reaction at $\sqrt{s} = 200\text{GeV}$ as a function of p_T , scale $\mu = p_T$. Data from Phenix Collaboration [62]. Solid curve fragmentation functions from KKP [100], dashed curve BKP [101].

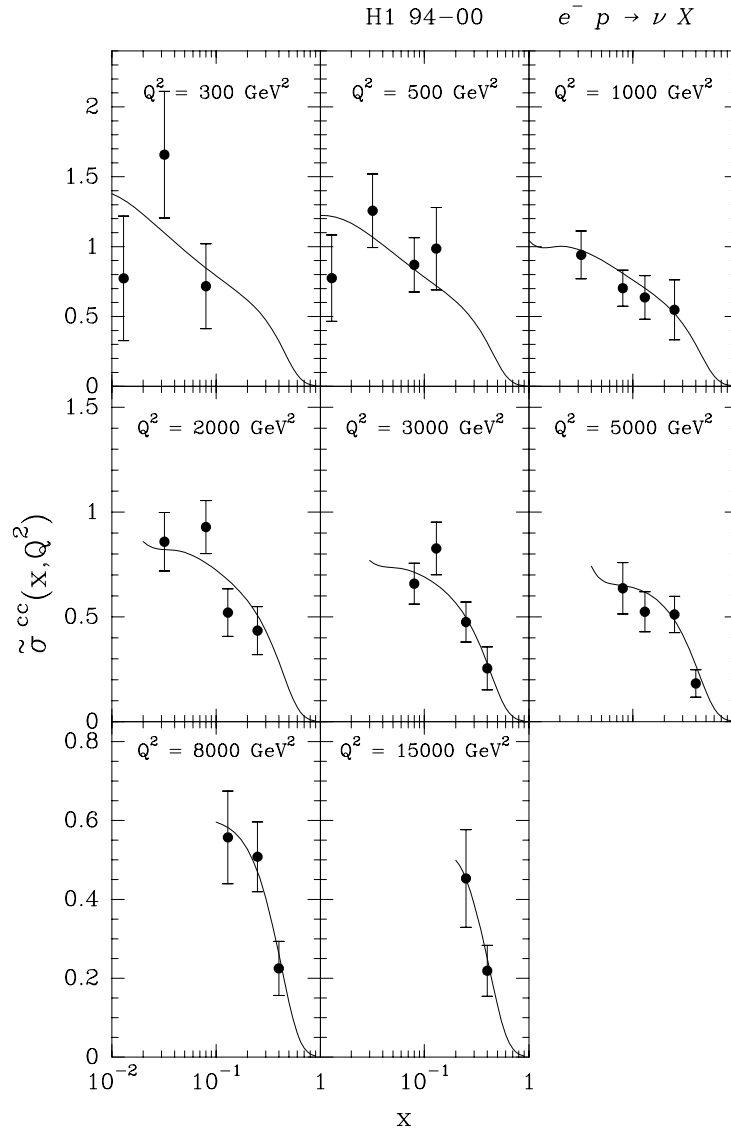


Figure 70: The reduced charged current cross section, $\tilde{\sigma}$, in e^-p reaction as a function of x , for different fixed values of Q^2 . Data from H1 Coll. [40].

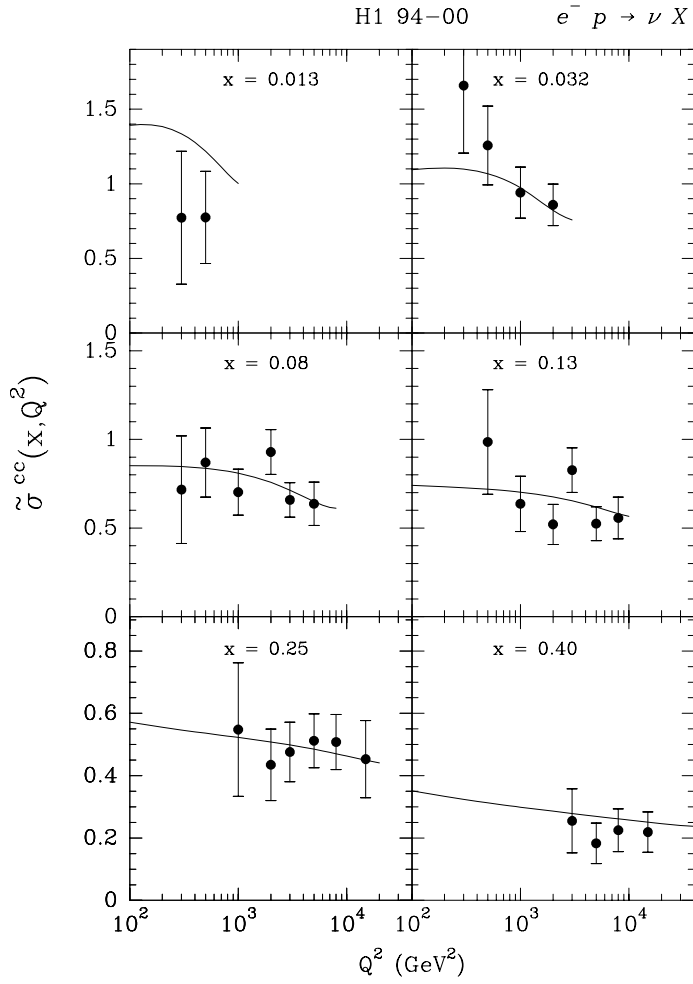


Figure 71: The reduced charged current cross section, $\tilde{\sigma}$, in e^-p reaction as a function of Q^2 , for different fixed values of x . Data from H1 Coll. [40].

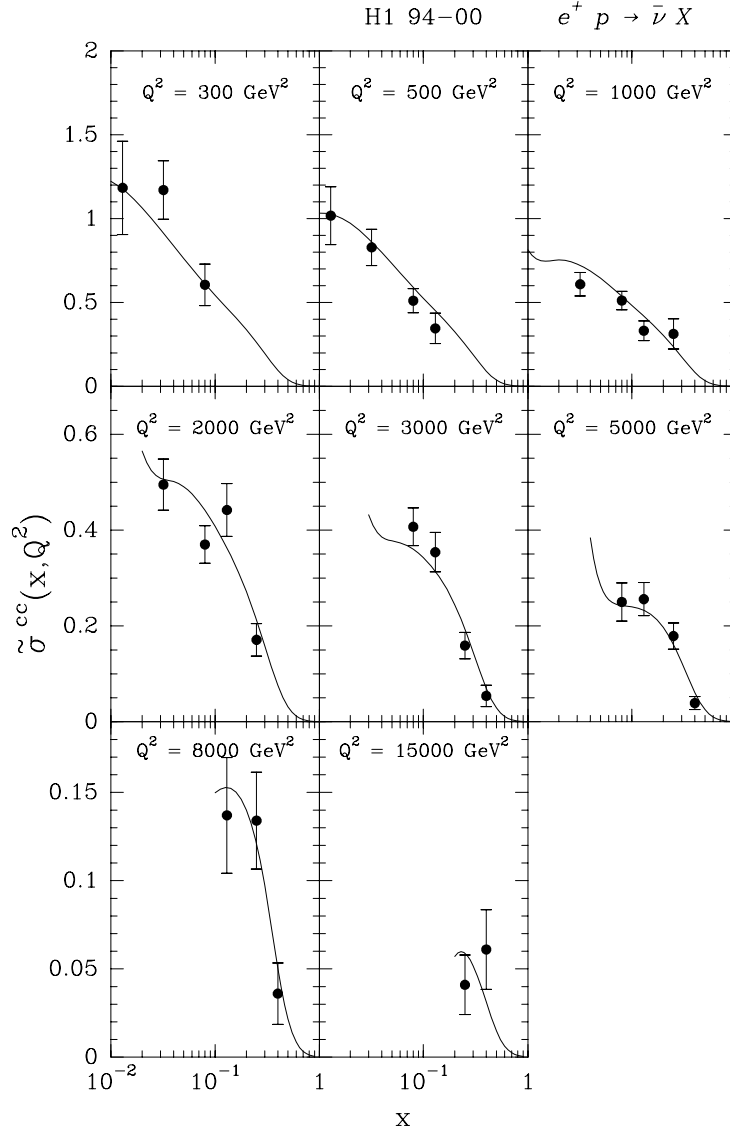


Figure 72: The reduced charged current cross section, $\tilde{\sigma}$, in e^+p reaction as a function of x , for different fixed values of Q^2 . Data from H1 Coll. [41].

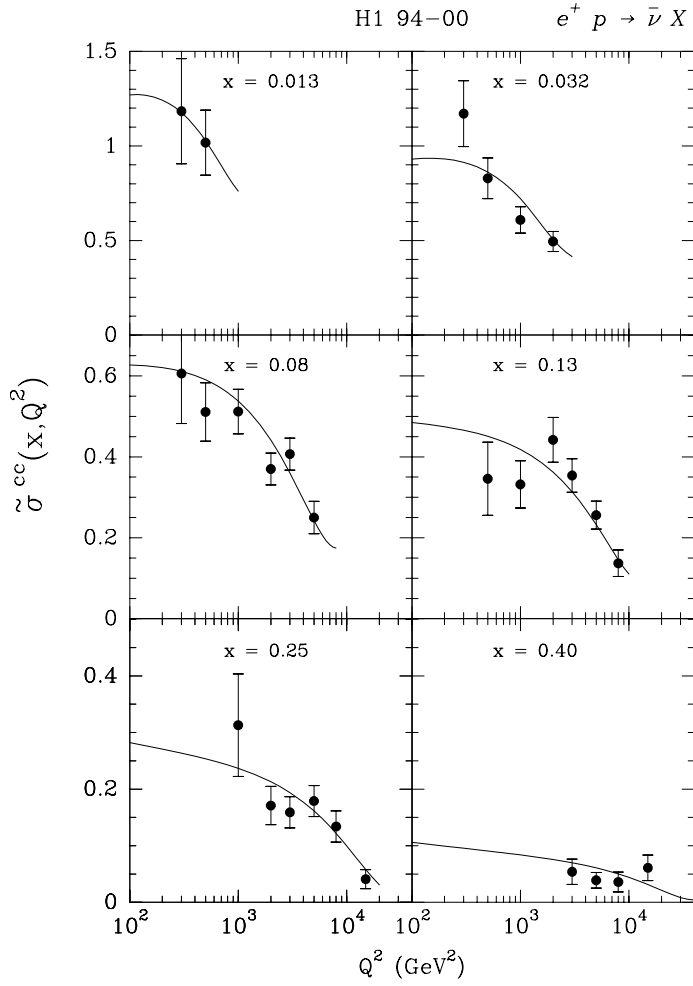


Figure 73: The reduced charged current cross section, $\tilde{\sigma}$, in e^+p reaction as a function of Q^2 , for different fixed values of x . Data from H1 Coll. [41].

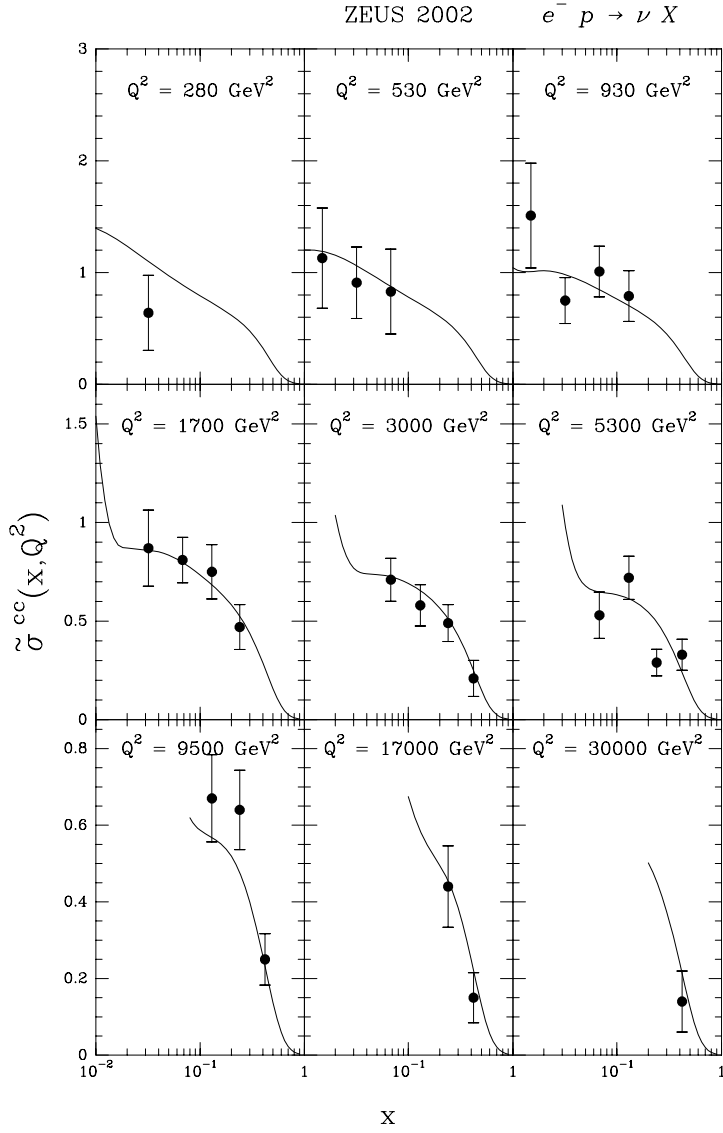


Figure 74: The reduced charged current cross section, $\tilde{\sigma}$, in e^-p reaction as a function of x , for different fixed values of Q^2 . Data from ZEUS Coll. [96].

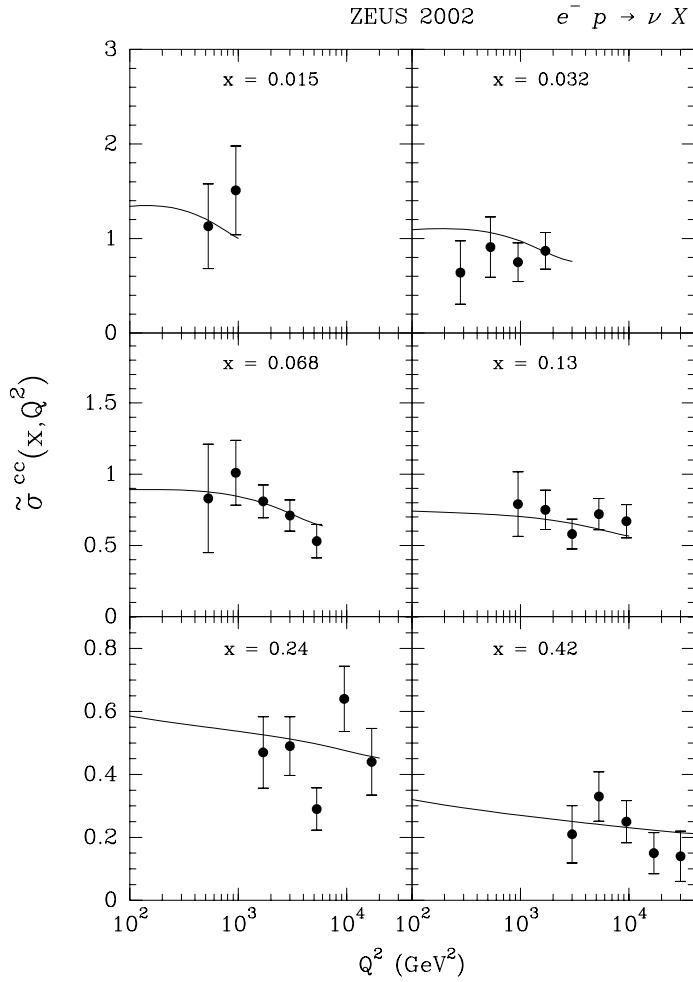


Figure 75: The reduced charged current cross section, $\tilde{\sigma}$, in e^-p reaction as a function of Q^2 , for different fixed values of x . Data from ZEUS Coll. [96].

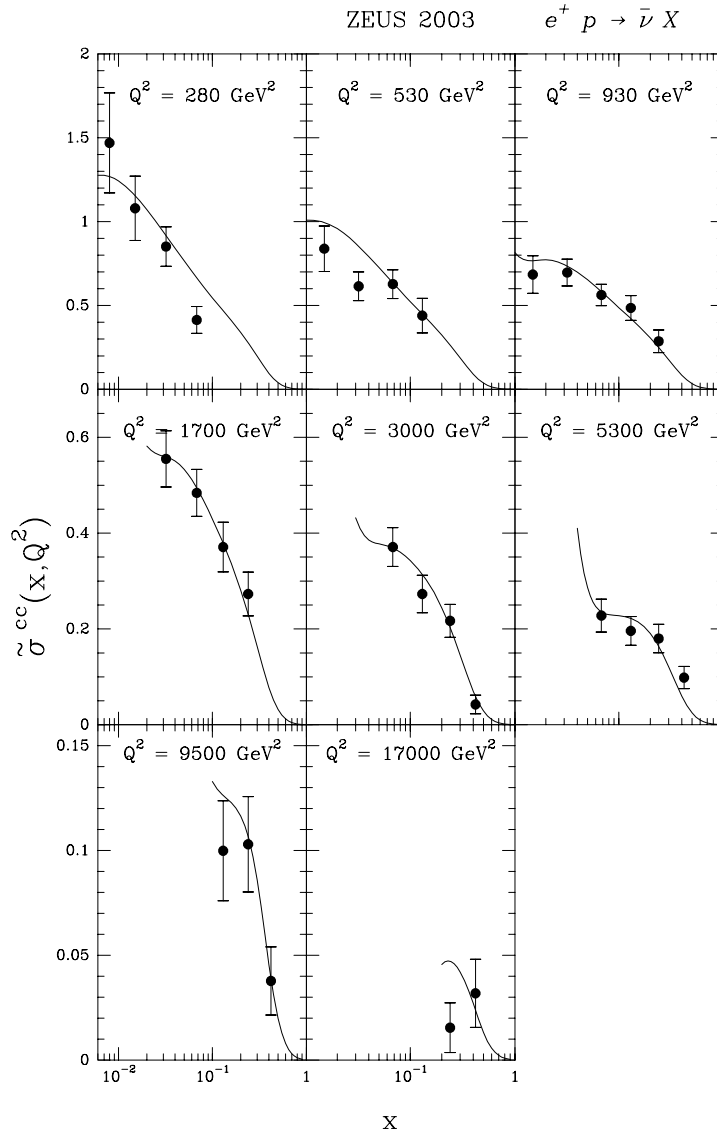


Figure 76: The reduced charged current cross section, $\tilde{\sigma}$, in e^+p reaction as a function of x , for different fixed values of Q^2 . Data from ZEUS Coll. [97].

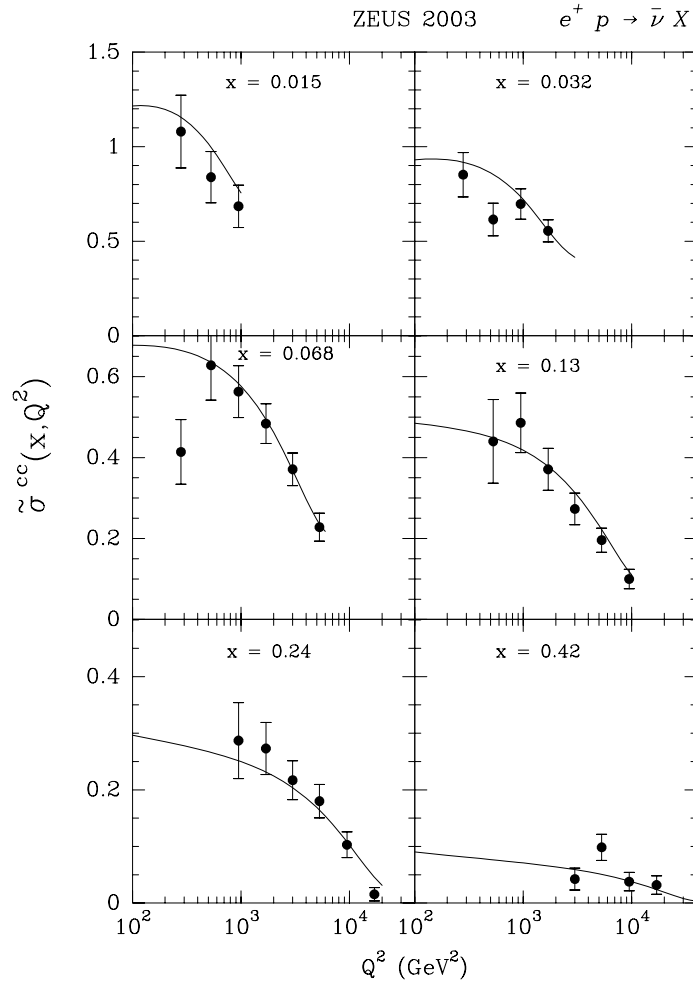


Figure 77: The reduced charged current cross section, $\tilde{\sigma}$, in e^+p reaction as a function of Q^2 , for different fixed values of x . Data from ZEUS Coll. [97].

H1 $e^- p \rightarrow e^- X$

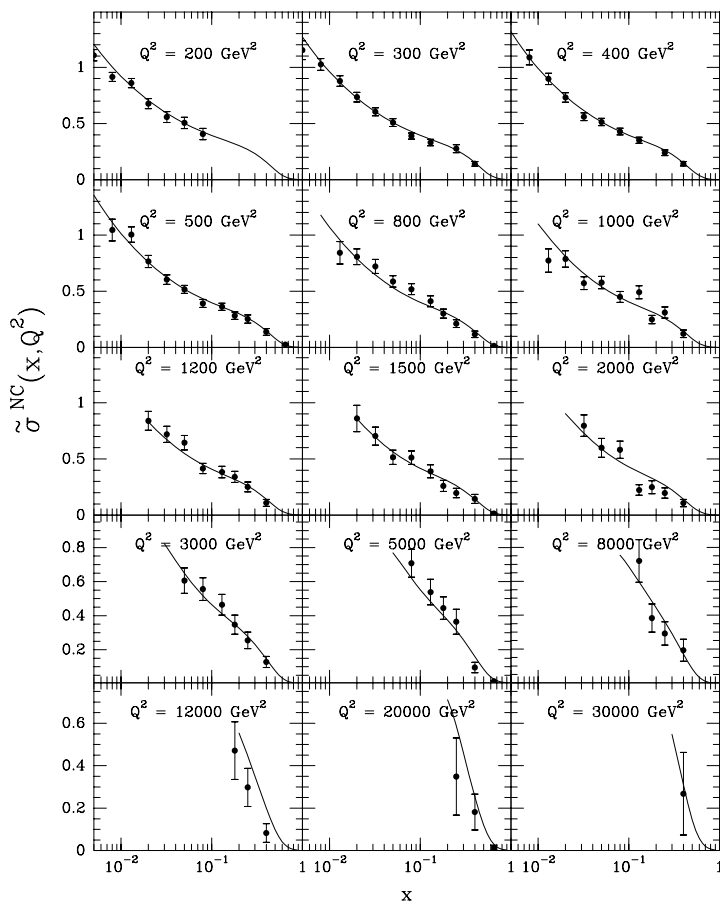


Figure 78: The reduced neutral current cross section $\tilde{\sigma}$, in $e^- p$ reaction as a function of x , for different fixed values of Q^2 and $\sqrt{s} = 320\text{GeV}$. Data from H1 Coll [40]

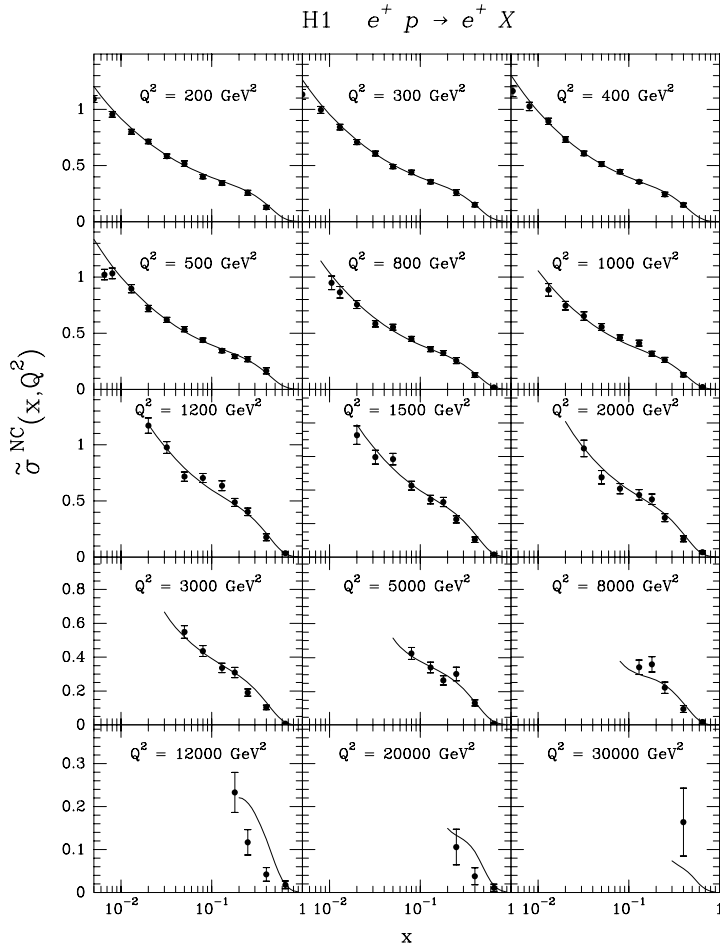


Figure 79: The reduced neutral current cross section $\tilde{\sigma}$, in e^+p reaction as a function of x , for different fixed values of Q^2 and $\sqrt{s} = 319\text{GeV}$. Data from H1 Coll [40]

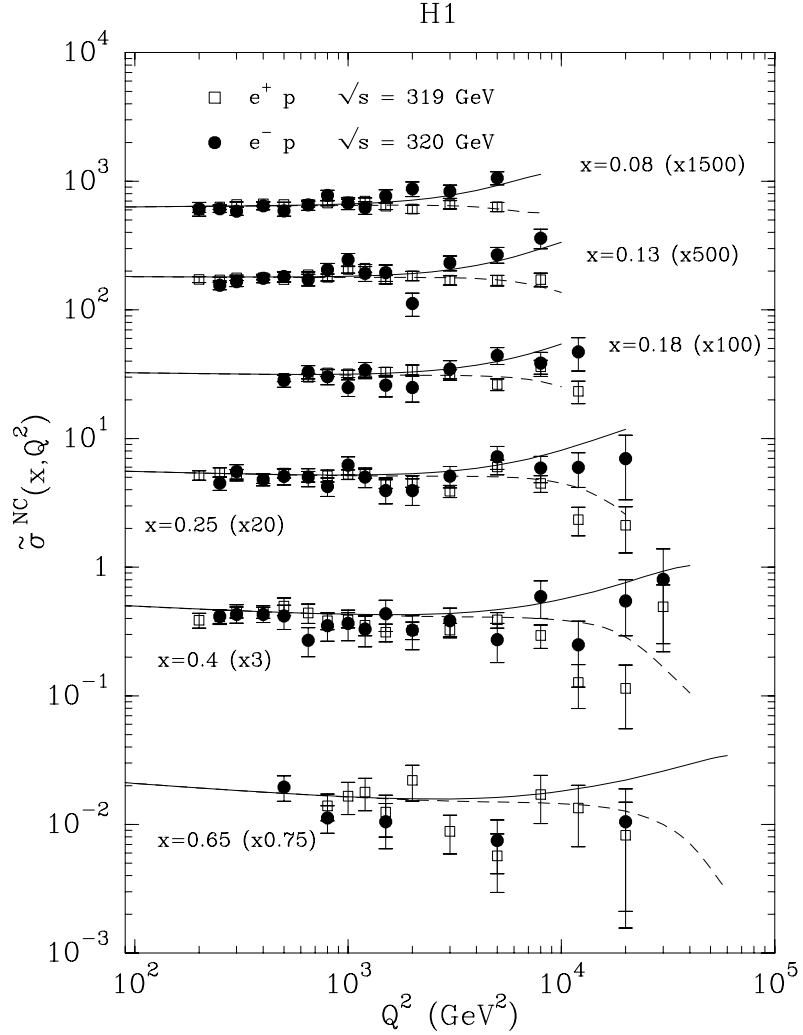


Figure 80: The reduced neutral current cross section $\tilde{\sigma}$, in $e^\pm p$ reaction as a function of Q^2 , for different fixed values of x . Solid line $e^- p$, dashed line $e^+ p$. Data from H1 Coll [40]

ZEUS $e^- p \rightarrow e^- X$

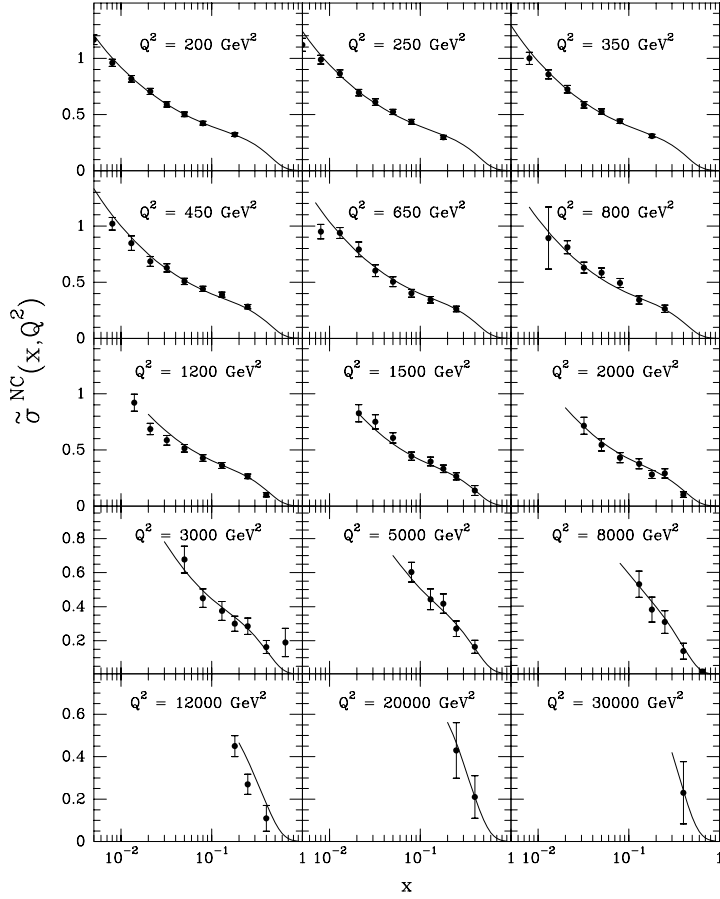


Figure 81: The reduced neutral current cross section $\tilde{\sigma}$, in $e^- p$ reaction as a function of x , for different fixed values of Q^2 and $\sqrt{s} = 318\text{GeV}$. Data from Zeus Coll [97]

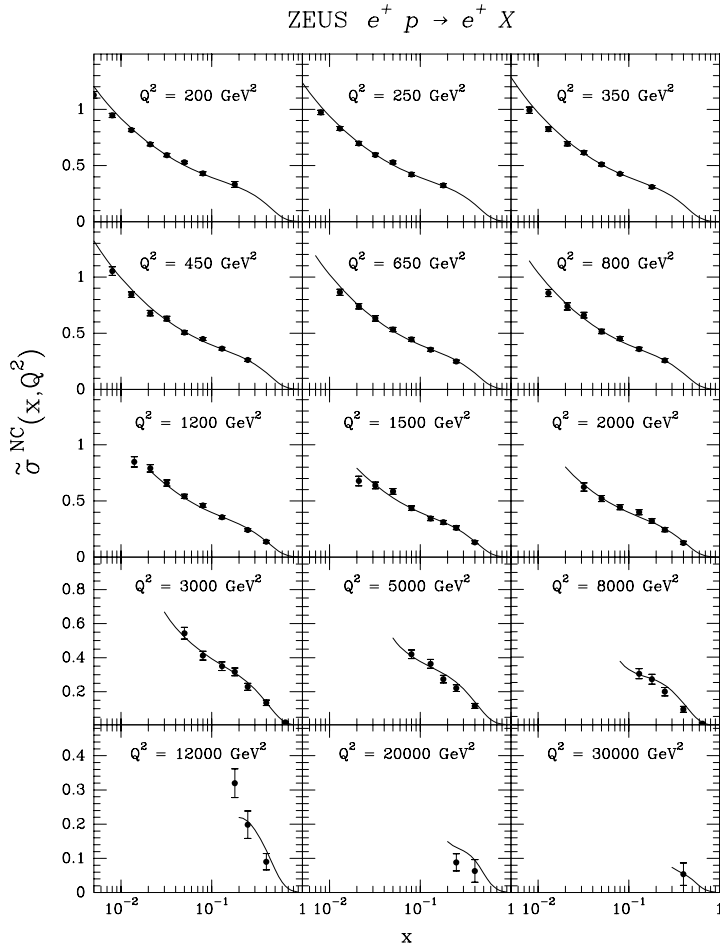


Figure 82: The reduced neutral current cross section $\tilde{\sigma}$, in e^+p reaction as a function of x , for different fixed values of Q^2 and $\sqrt{s} = 318\text{GeV}$. Data from Zeus Coll [97]

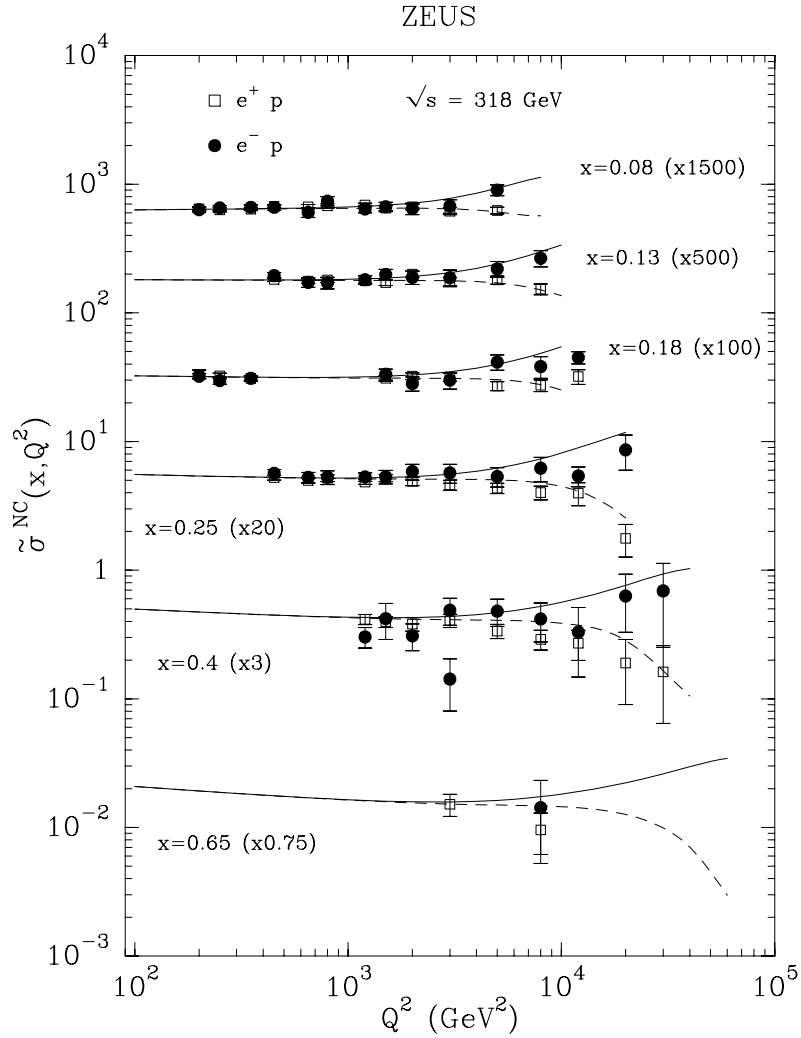


Figure 83: The reduced neutral current cross section $\tilde{\sigma}$, in $e^\pm p$ reaction as a function of Q^2 , for different fixed values of x . Solid line e^-p , dashed line e^+p . Data from Zeus Coll [97]

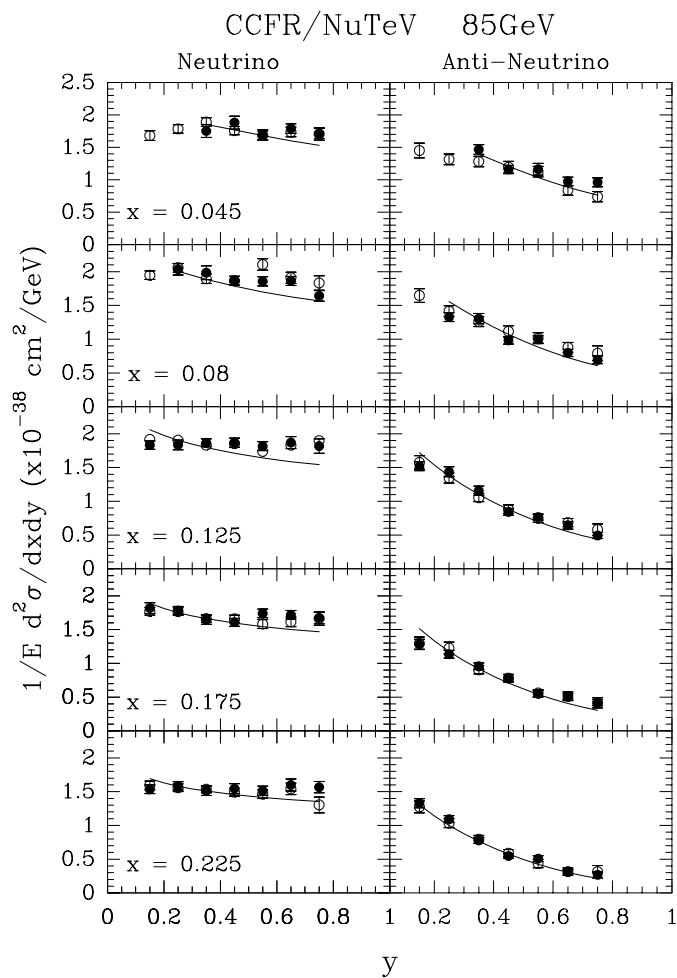


Figure 84: Differential cross section νN proton for $E_\nu = 85\text{GeV}$ as a function of y for different x bins. Data from CCFR [29] and NuTeV collaboration [31, 30].

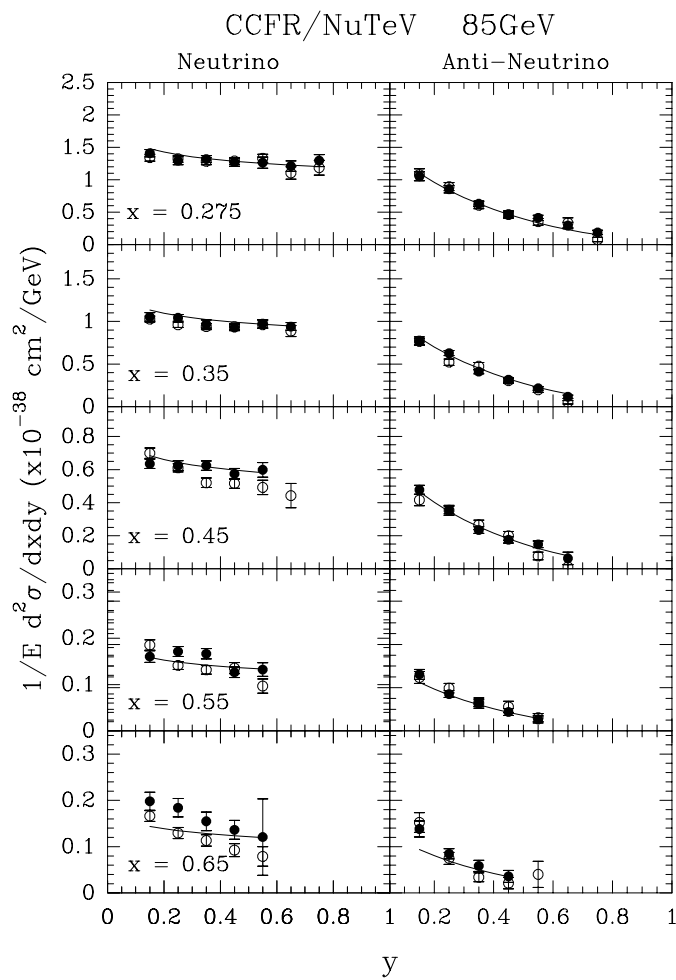


Figure 85: Differential cross section νN proton for $E_\nu = 85\text{GeV}$ as a function of y for different x bins. Data from CCFR [29] and NuTeV collaboration [31, 30].

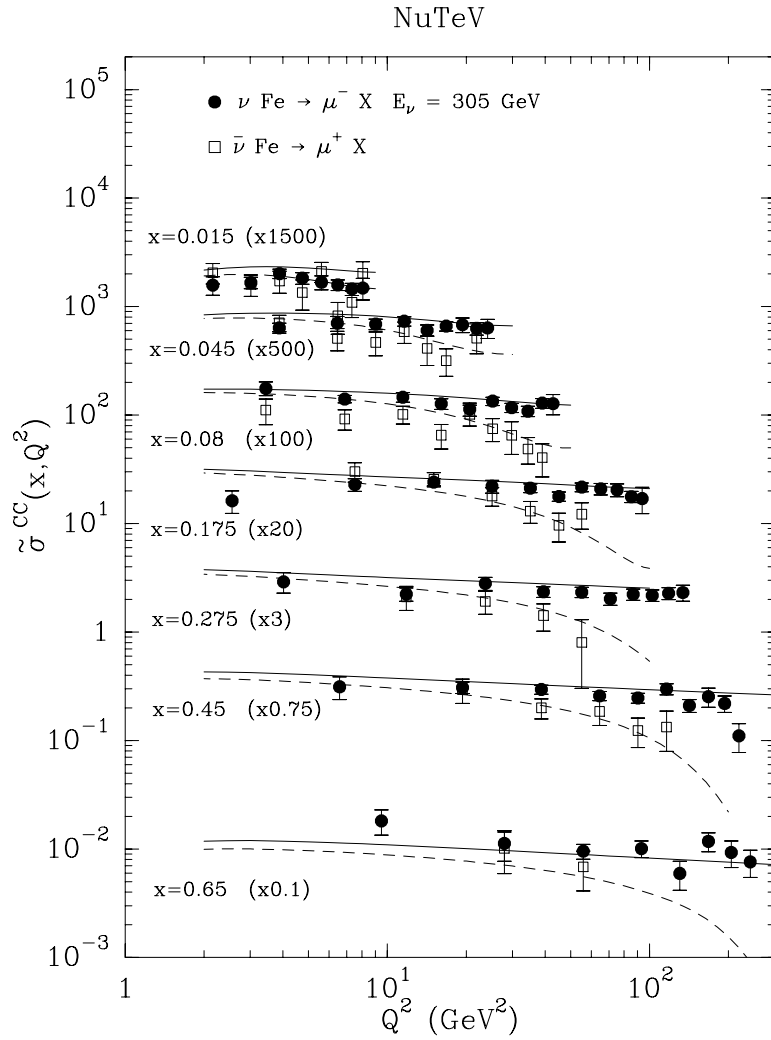


Figure 86: The reduced charged current cross section νN , for different x bins as a function of Q^2 . The data points are obtained from the differential cross section [31, 30], they are not a direct measurement

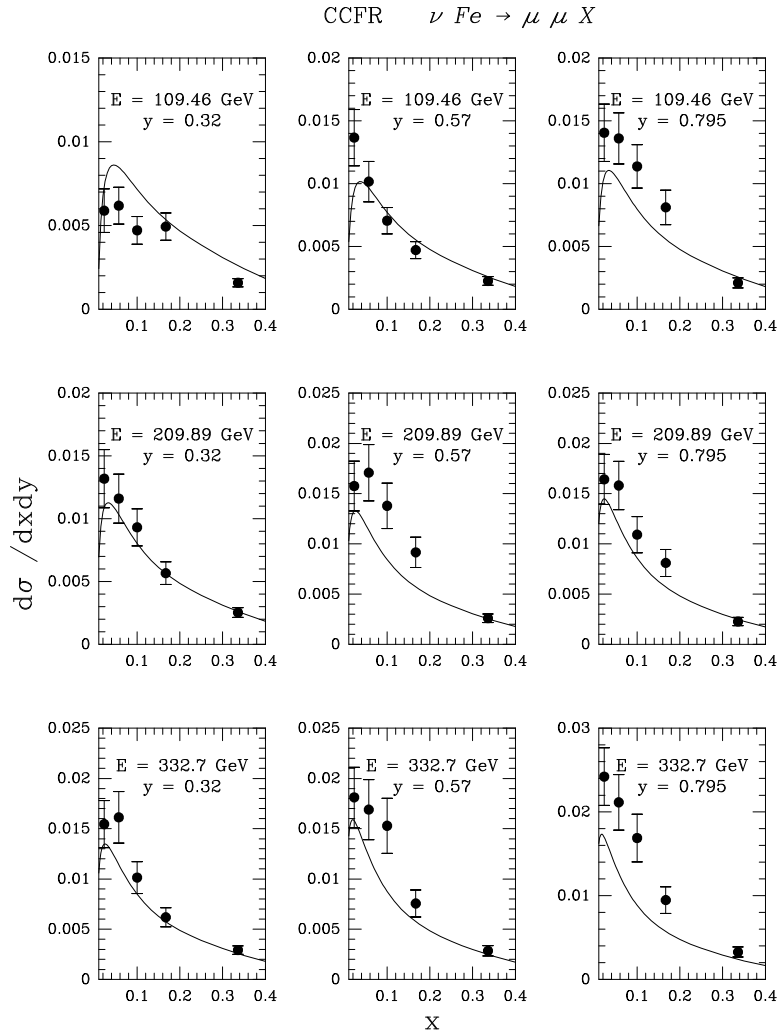


Figure 87: Comparison of the CCFR ν data [103] to the result of the fit for $d\sigma/dxdy$, in units of charged-current σ , for various kinematic ranges in energy, x and y .

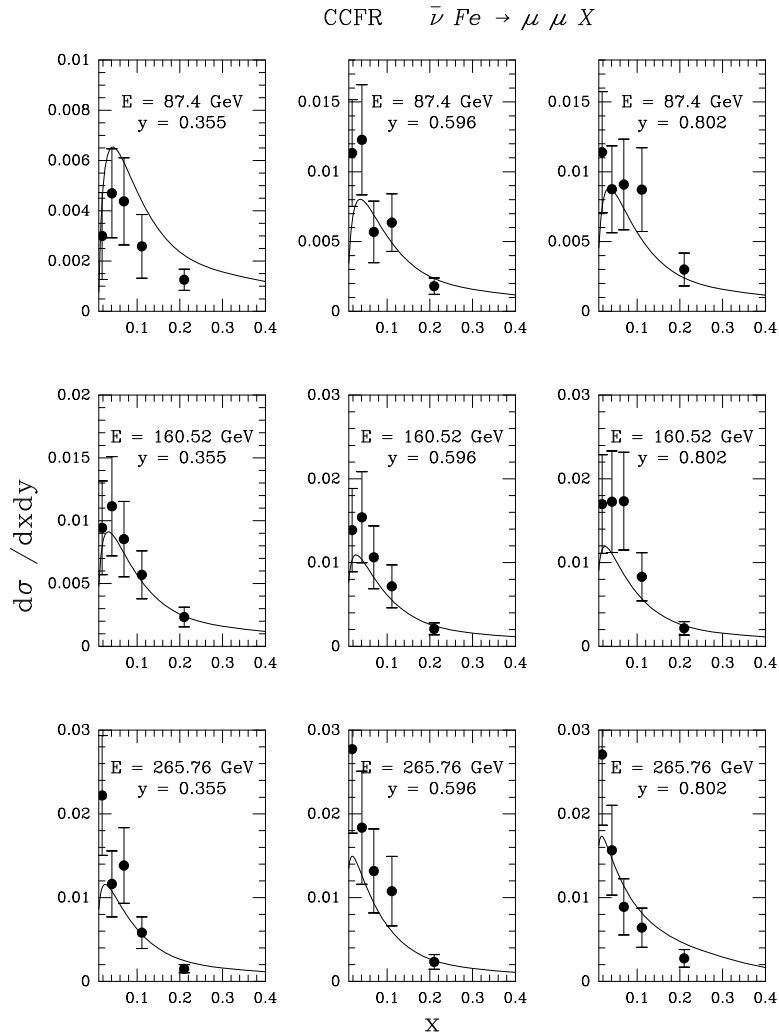


Figure 88: Comparison of the CCFR $\bar{\nu}$ data [103] to the result of the fit for $d\sigma/dx dy$ in units of charged-current σ , for various kinematic ranges in energy, x and y .

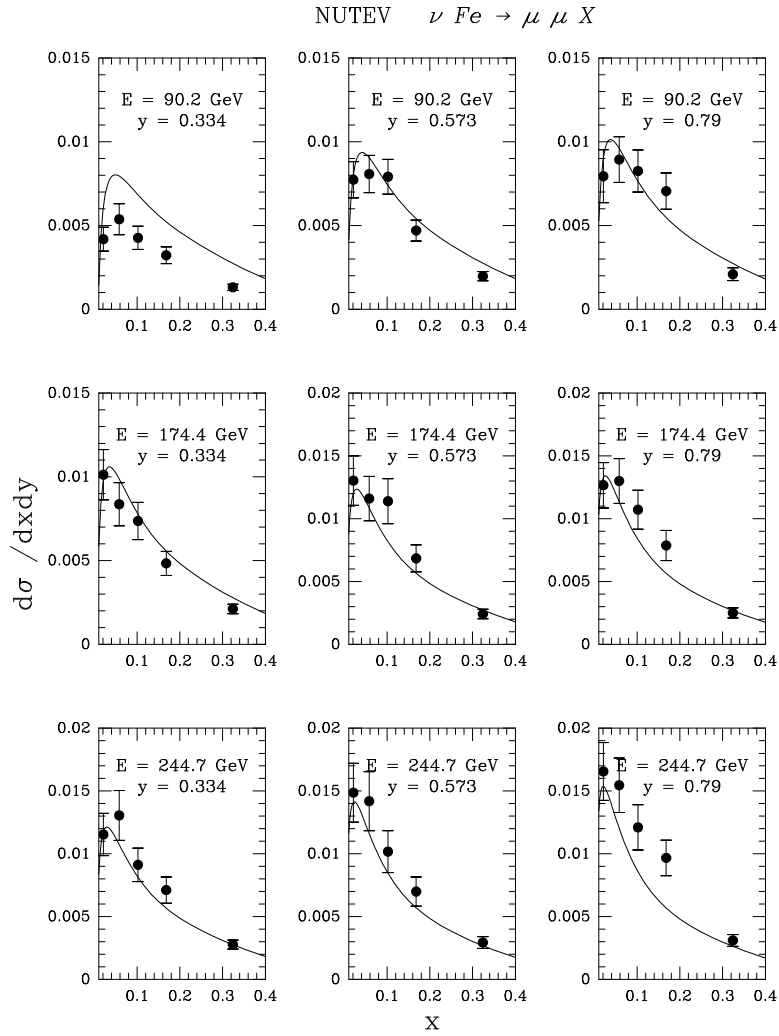


Figure 89: Comparison of the NuTeV ν data [103] to the result of the fit for $d\sigma/dx dy$, in units of charged-current σ , for various kinematic ranges in energy, x and y .

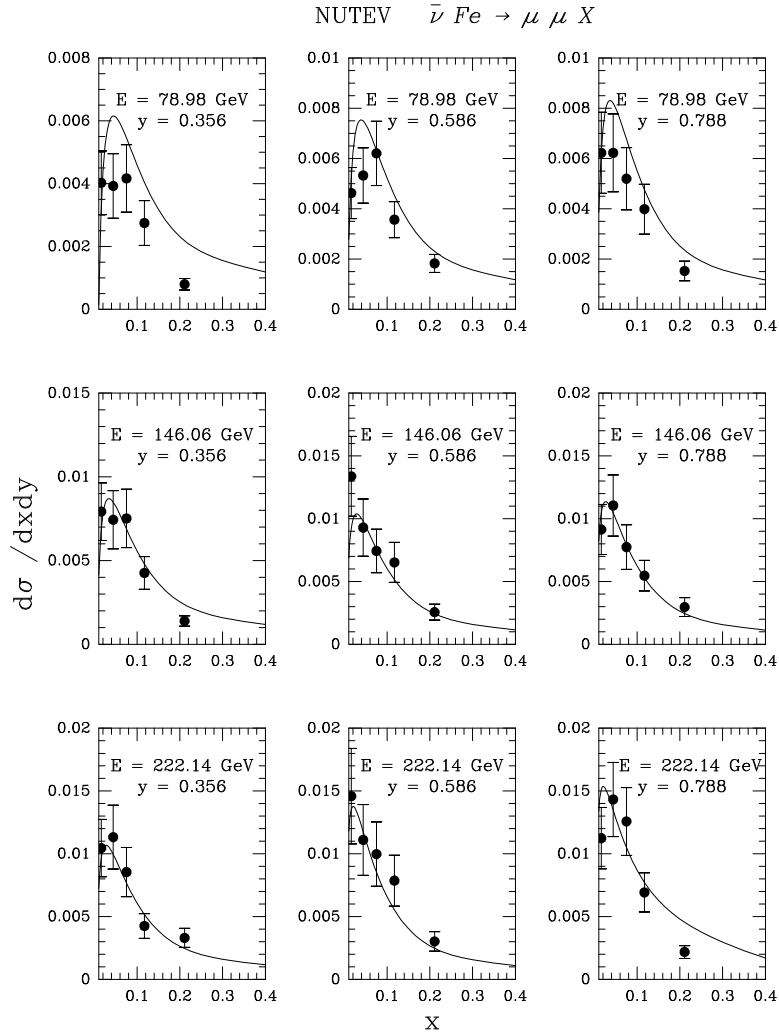


Figure 90: Comparison of the NuTeV $\bar{\nu}$ data [103] to the result of the fit for $d\sigma/dx dy$, in units of charged-current σ , for various kinematic ranges in energy, x and y .

5 Polarized experiments

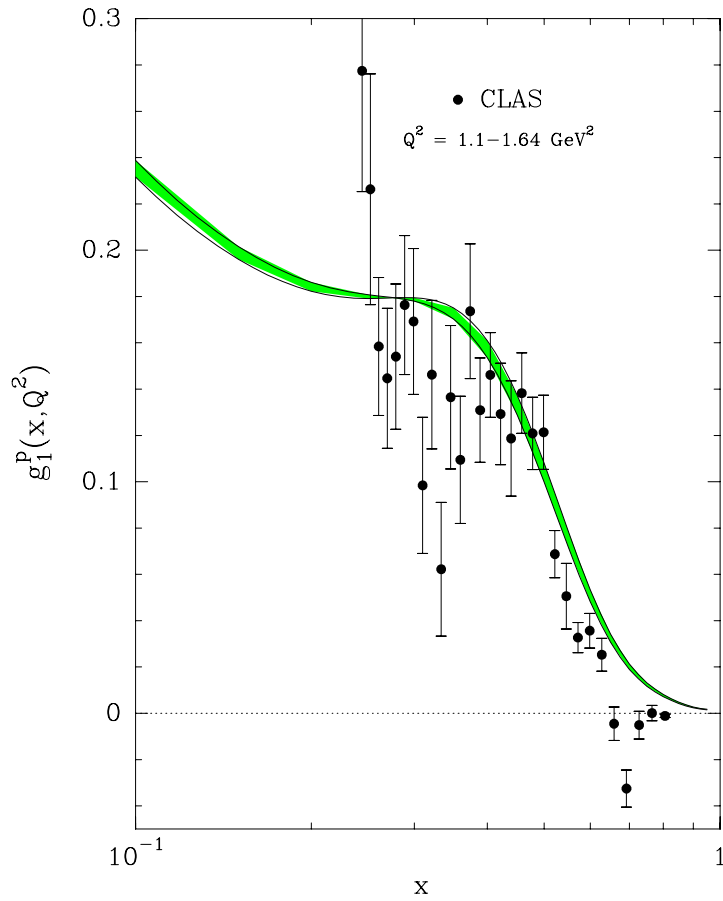


Figure 91: $g_1^p(x, Q^2)$ as function of x at for a range $1.1 \leq Q^2 \leq 1.64 \text{GeV}^2$, CLAS Coll [16]. The two curves represent the extreme Q^2 values.

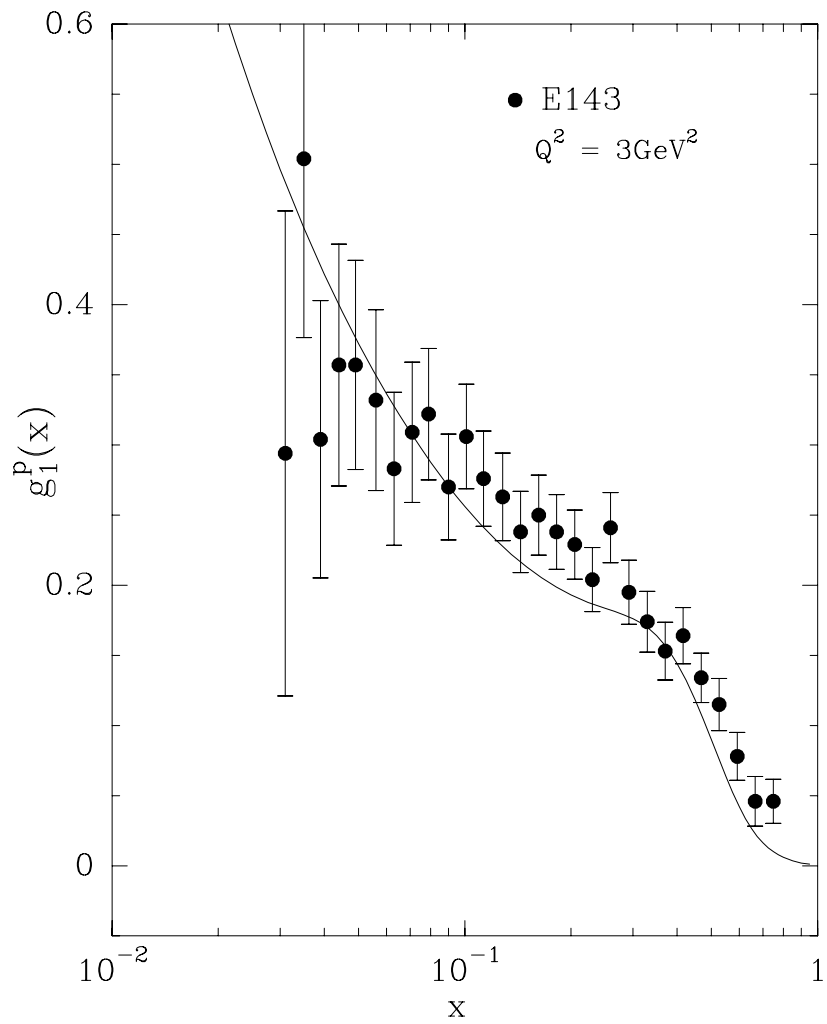


Figure 92: $g_1^p(x, Q^2)$ as function of x at fixed $Q^2 = 3\text{GeV}^2$, E143 Coll.

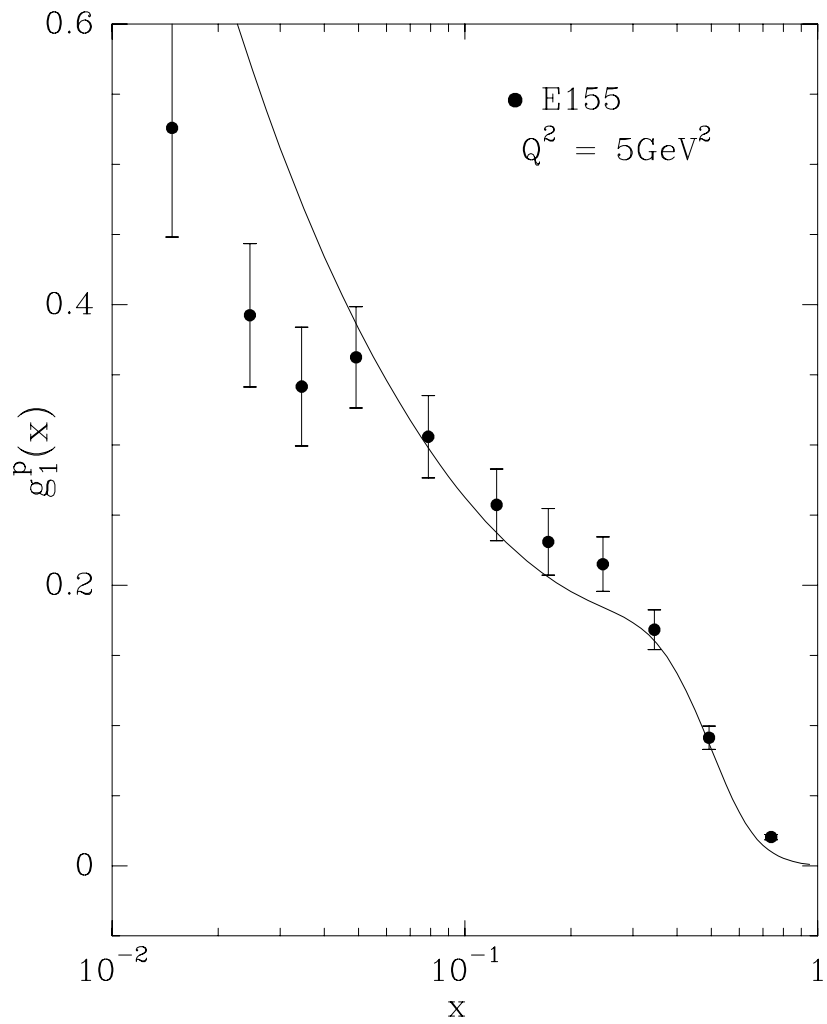


Figure 93: $g_1^p(x, Q^2)$ as function of x at fixed $Q^2 = 5\text{GeV}^2$, E155 Coll.

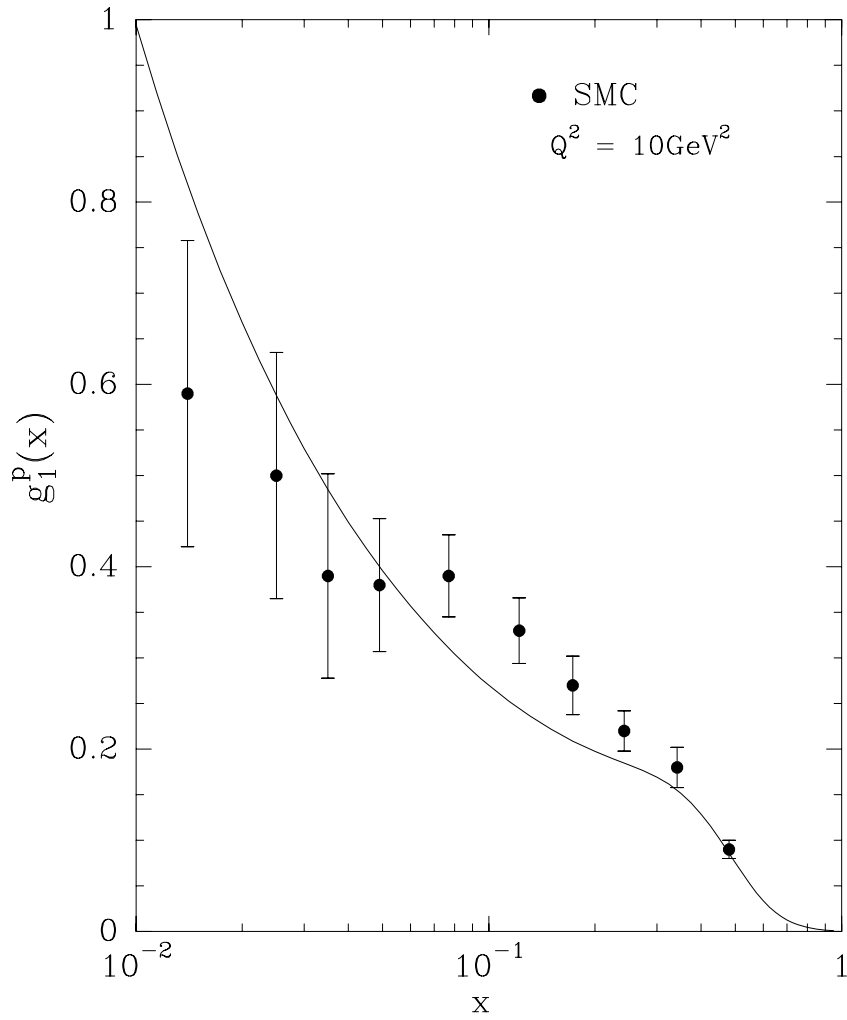


Figure 94: $g_1^p(x, Q^2)$ as function of x at fixed $Q^2 = 10\text{GeV}^2$, evolved SMC data.

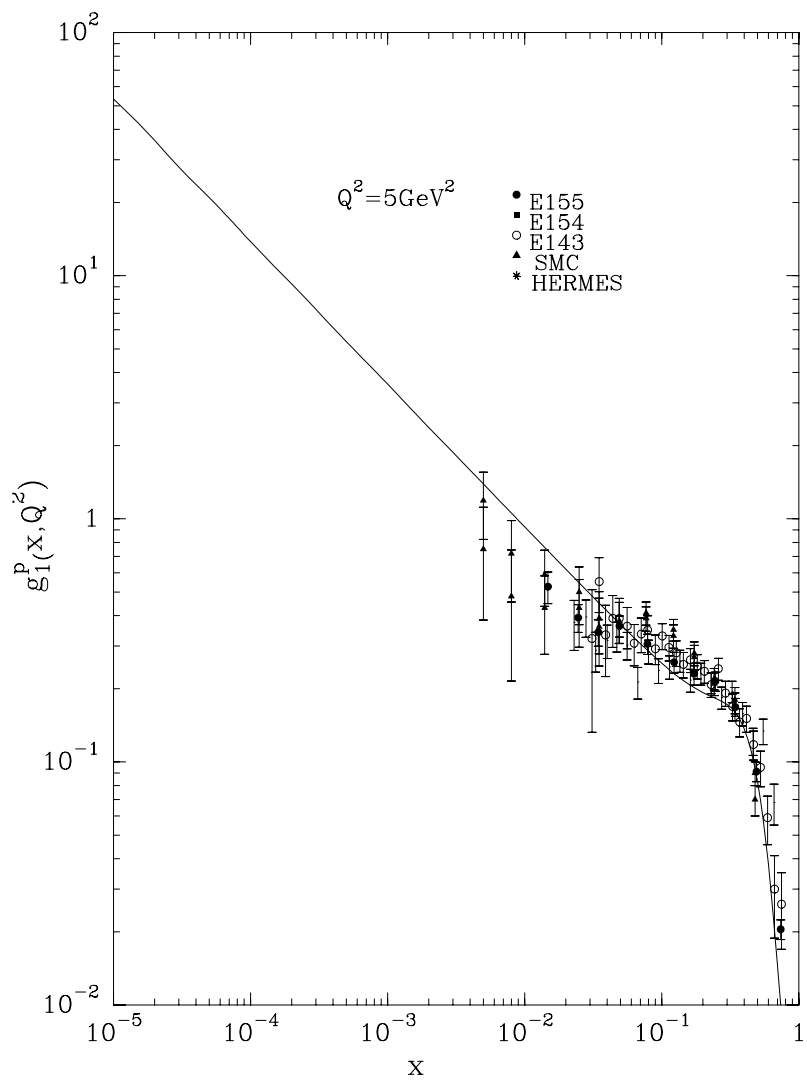


Figure 95: Behavior of $g_1^p(x, Q^2)$ at low x and fixed $Q^2 = 5\text{GeV}^2$,

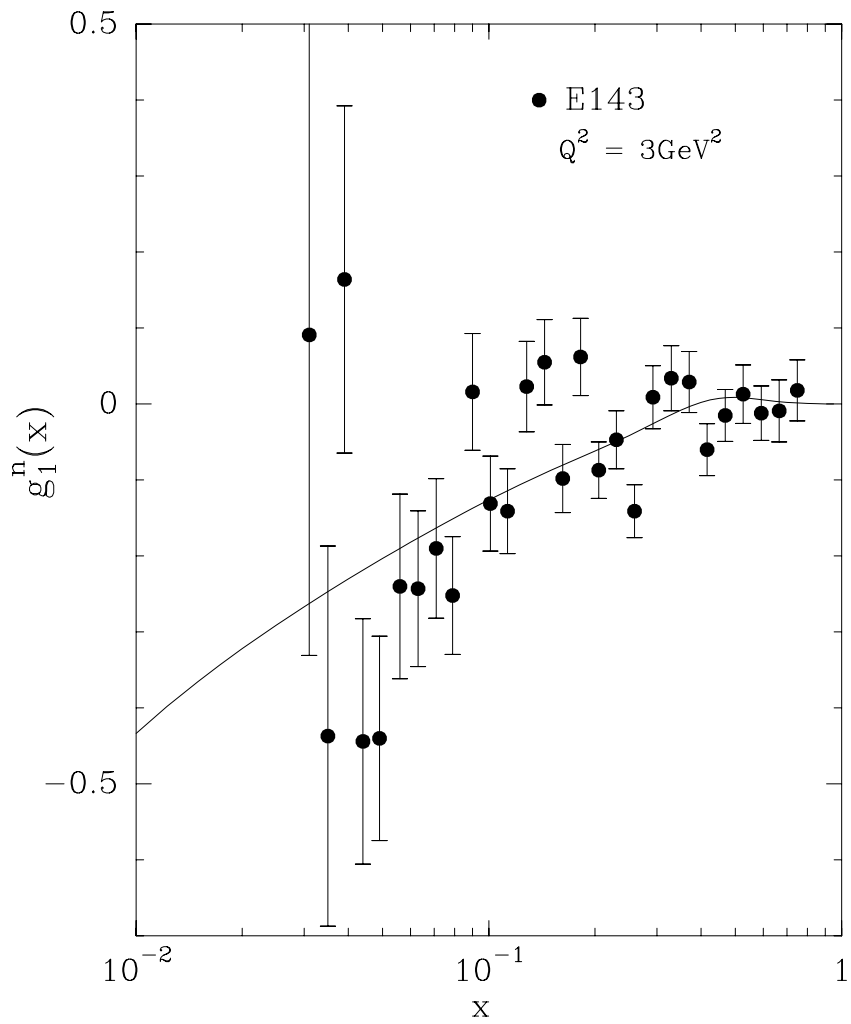


Figure 96: $g_1^n(x, Q^2)$ as function of x at fixed $Q^2 = 3\text{GeV}^2$, E143 Coll.

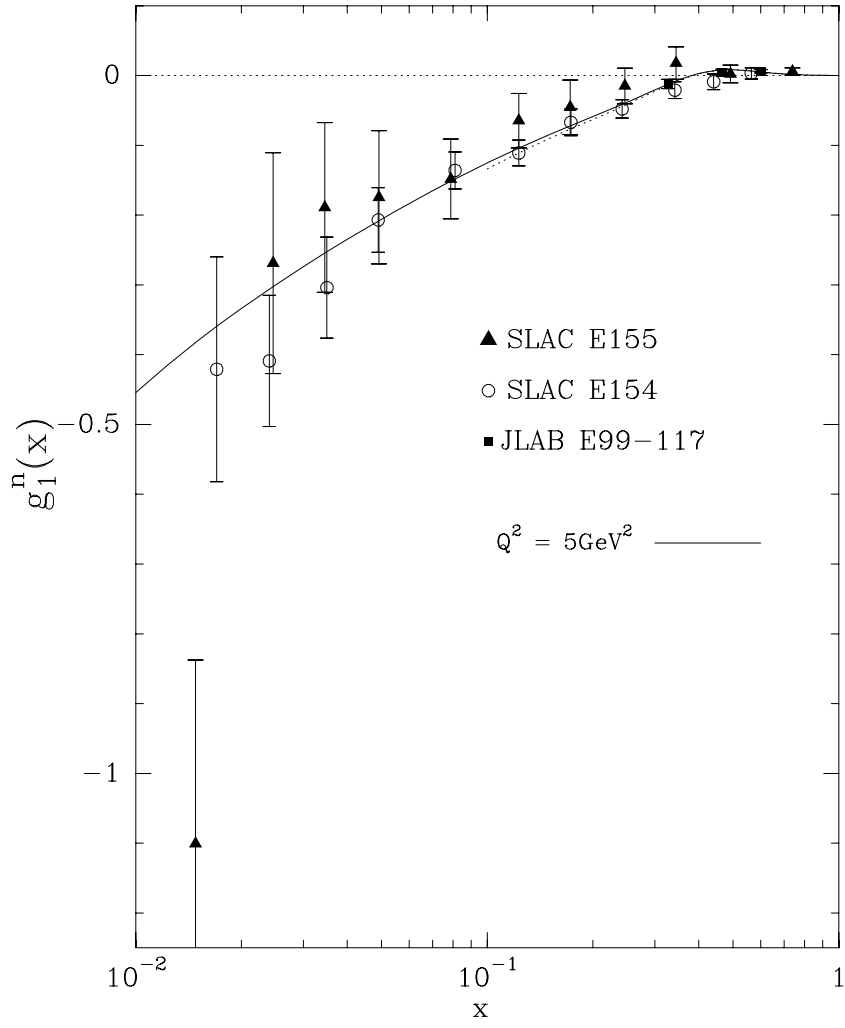


Figure 97: $g_1^n(x, Q^2)$ as function of x at fixed $Q^2 = 5\text{GeV}^2$, E154, E155, JLab Coll..

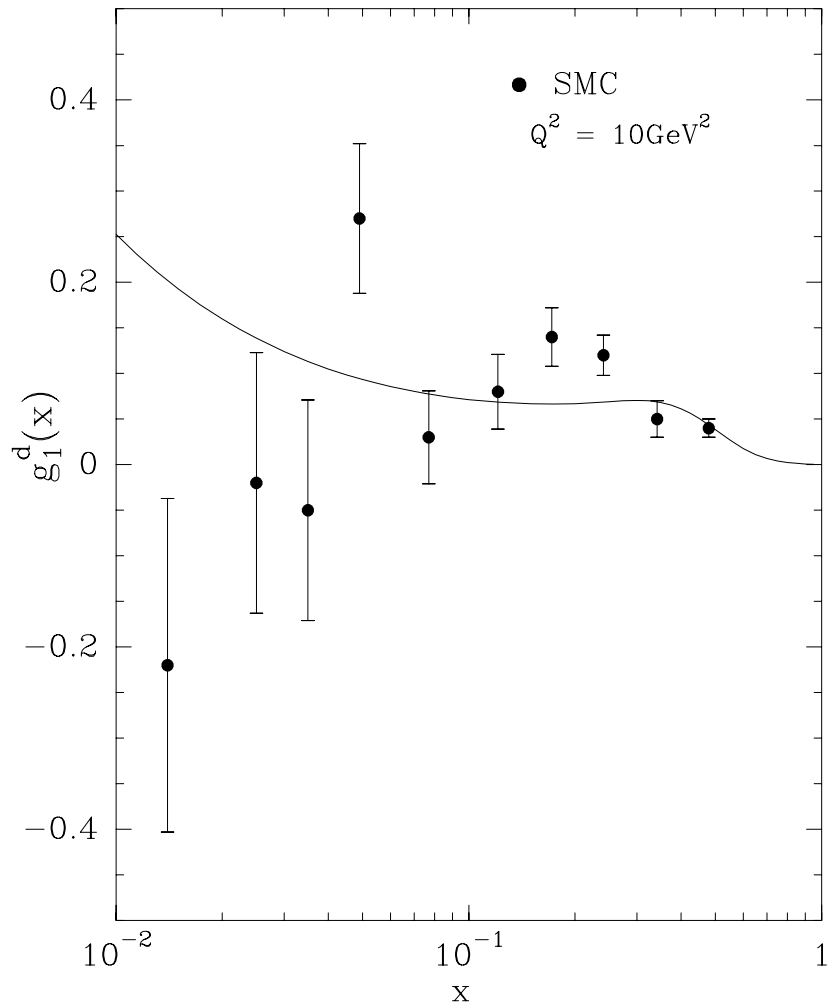


Figure 98: $g_1^d(x, Q^2)$ as function of x at fixed $Q^2 = 10 \text{ GeV}^2$, evolved SMC data.

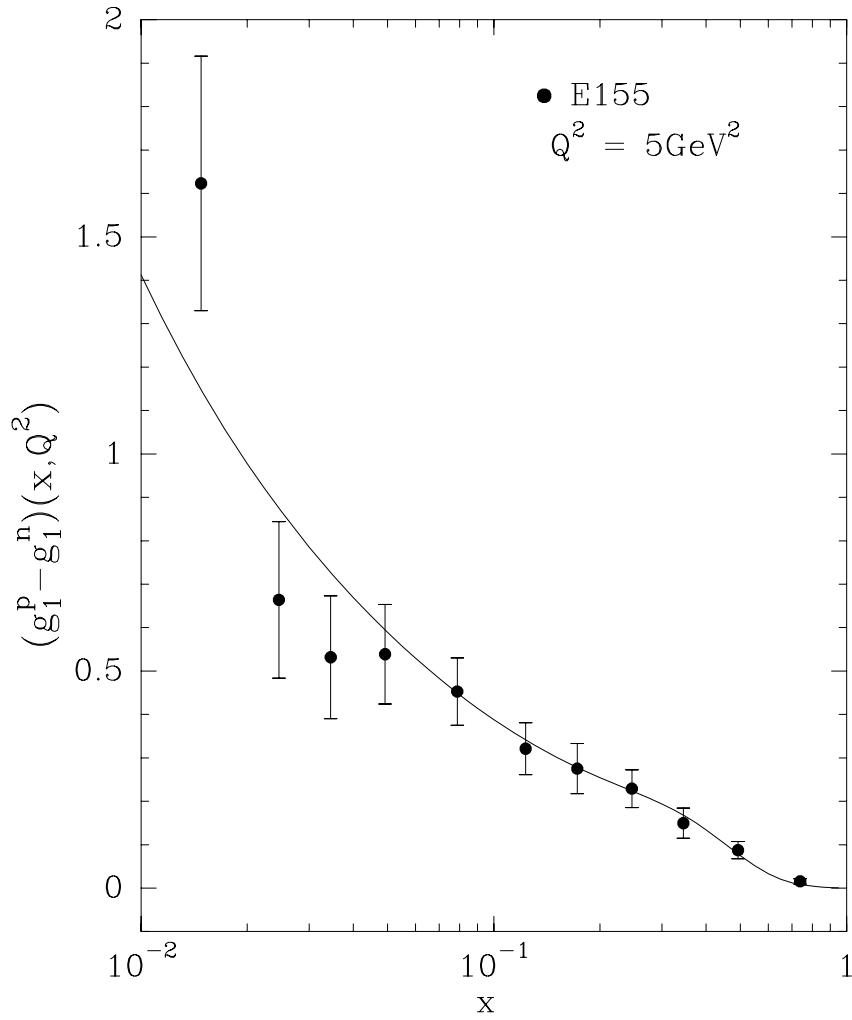


Figure 99: $g_1^p(x, Q^2) - g_1^n(x, Q^2)$ as function of x at fixed $Q^2 = 5\text{GeV}^2$, E155 Coll..

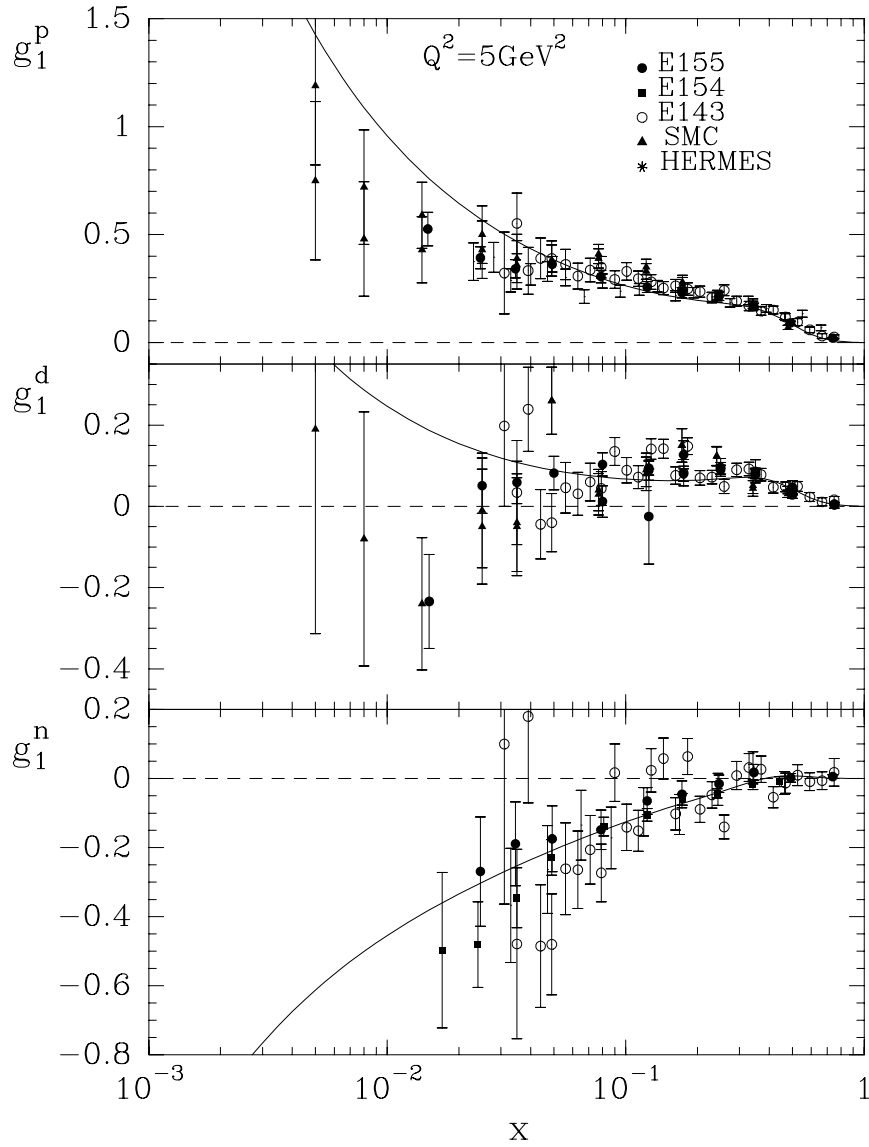


Figure 100: $g_1^{p,d,n}(x, Q^2)$ as function of x for different Q^2 values, from E155, E154, E143, SMC, HERMES experiments. The curves correspond to our model predictions at $Q^2 = 5\text{GeV}^2$.

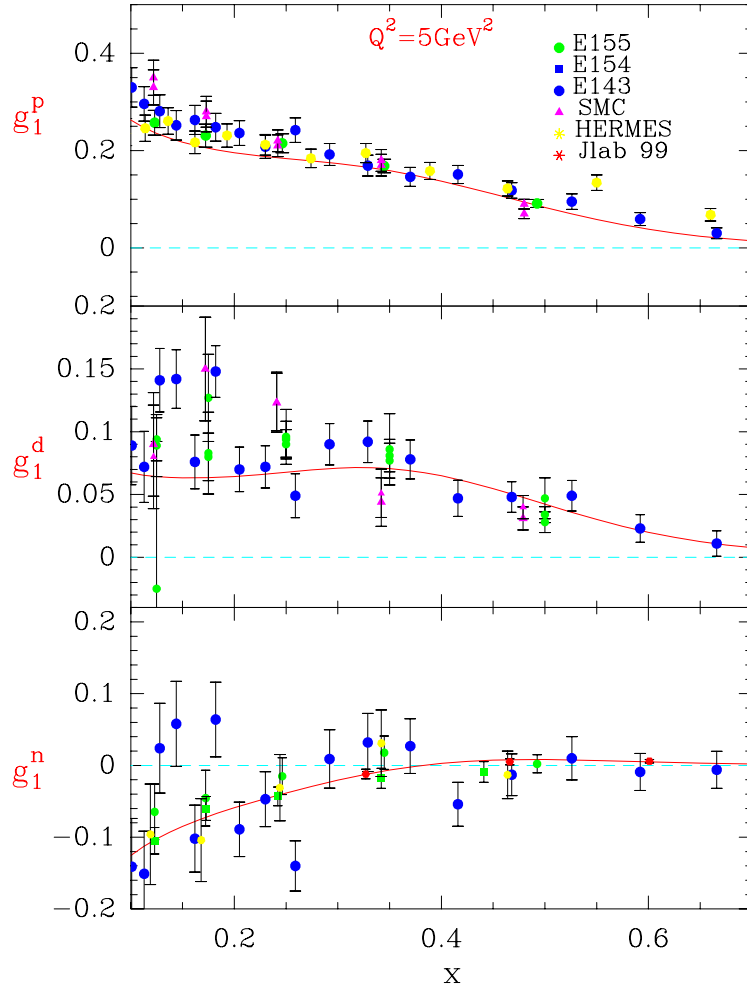


Figure 101: $g_1^{p,d,n}(x, Q^2)$ at large x values for different Q^2 values, from E155, E154, E143, SMC, HERMES, Jlab experiments. The curves correspond to our model predictions at $Q^2 = 5\text{GeV}^2$.

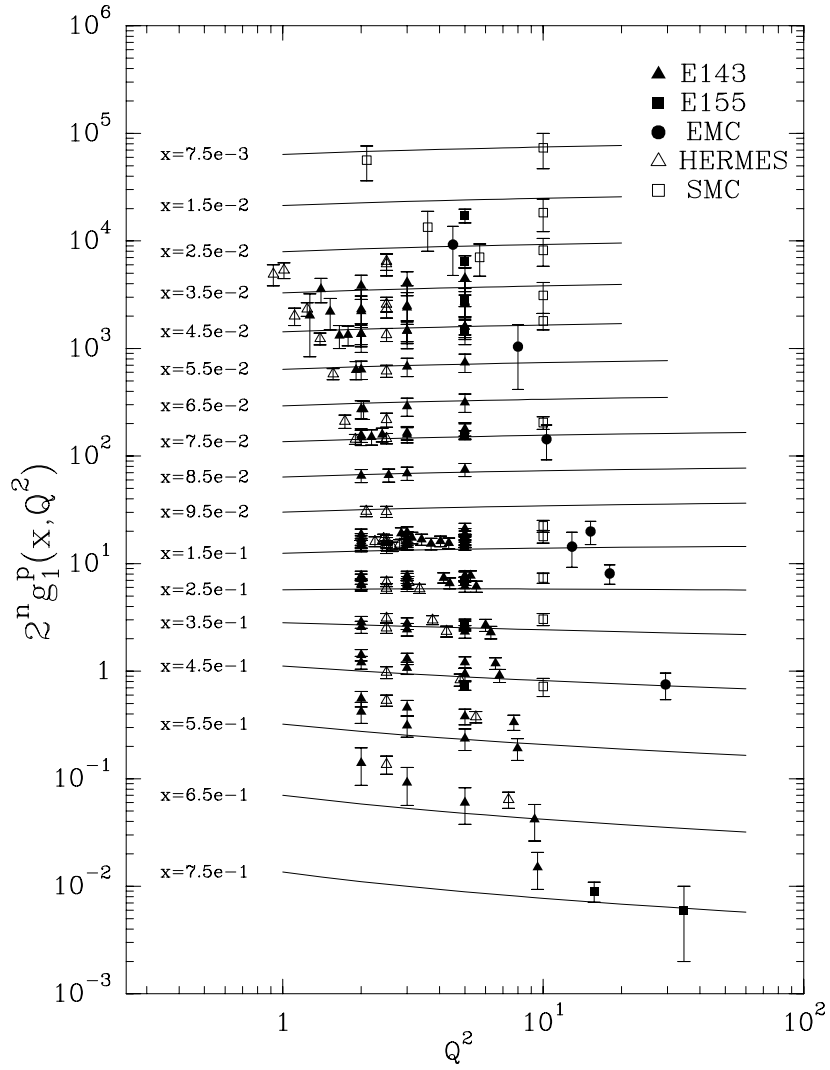


Figure 102: $2^n g_1^p(x, Q^2)$ as function of Q^2 for different x values. $n = 0$ corresponds to $x = 0.75$ and $n = 16$ to $x = 7.5 \cdot 10^{-3}$. Experimental data are rebinned to the nearest x values.

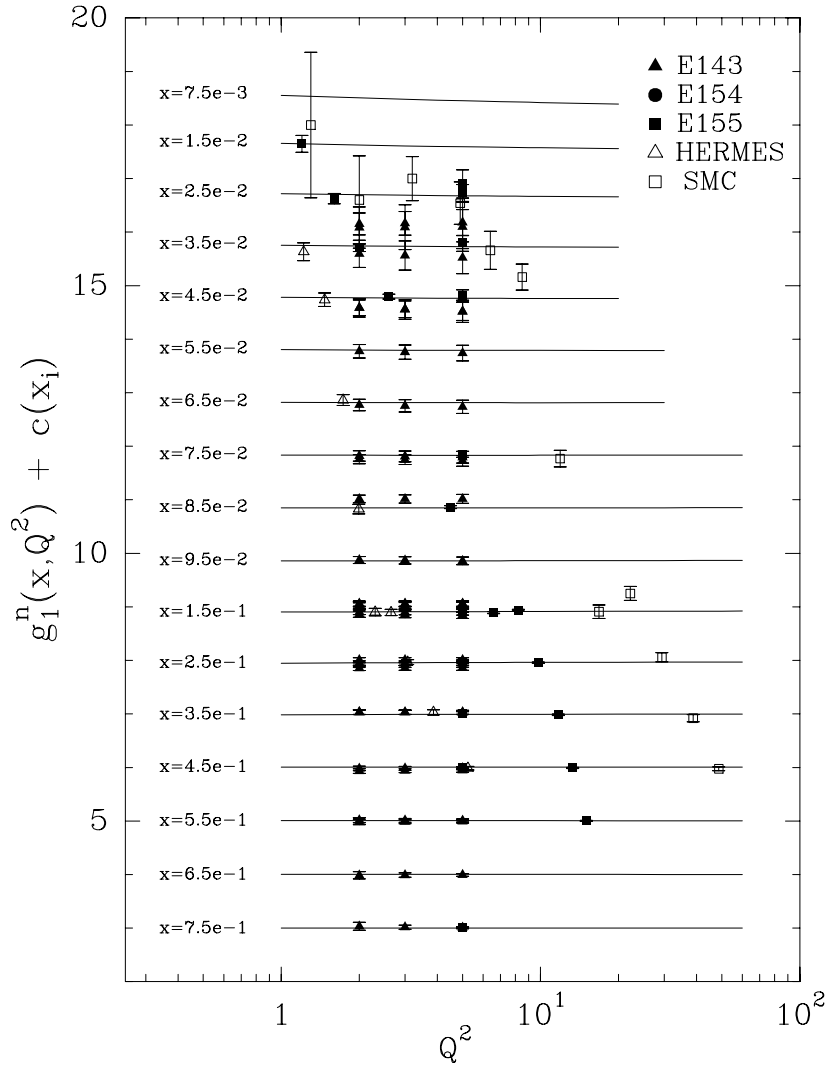


Figure 103: $g_1^n(x, Q^2)$ as function of Q^2 for different x values. The function $c(x_i) = 19 - i$, $i = 0$ corresponds to $x = 7.5 \cdot 10^{-3}$. Experimental data are rebinned to the nearest x values.

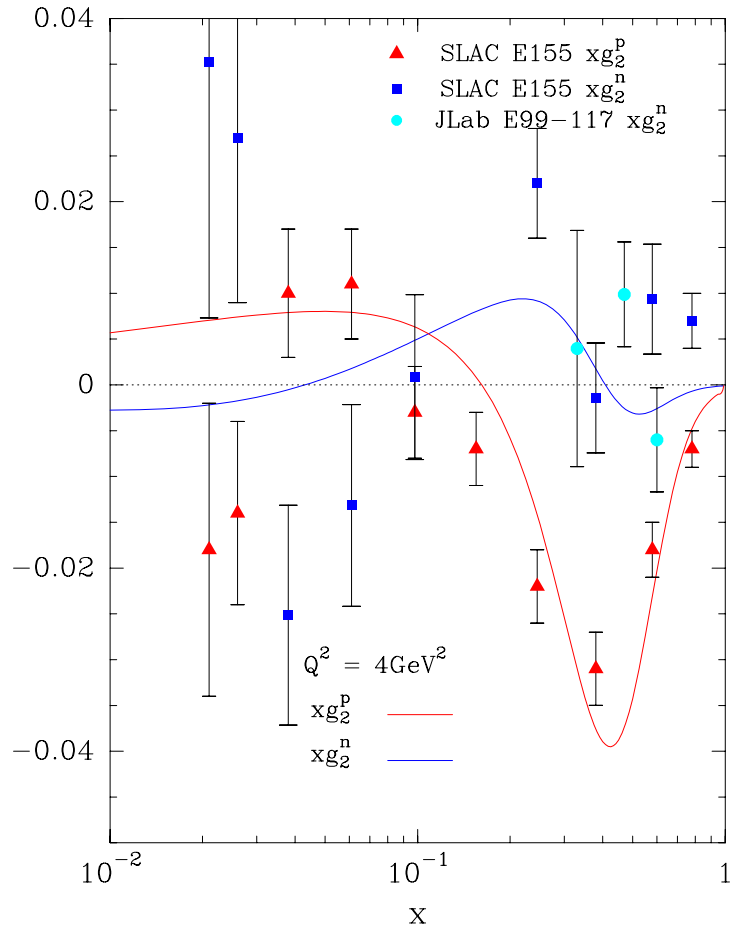


Figure 104: xg_2 for proton and neutron as a function of x , for $Q^2 = 4\text{GeV}^2$. Data from SLAC E155 [77], JLab E99-117 [54].

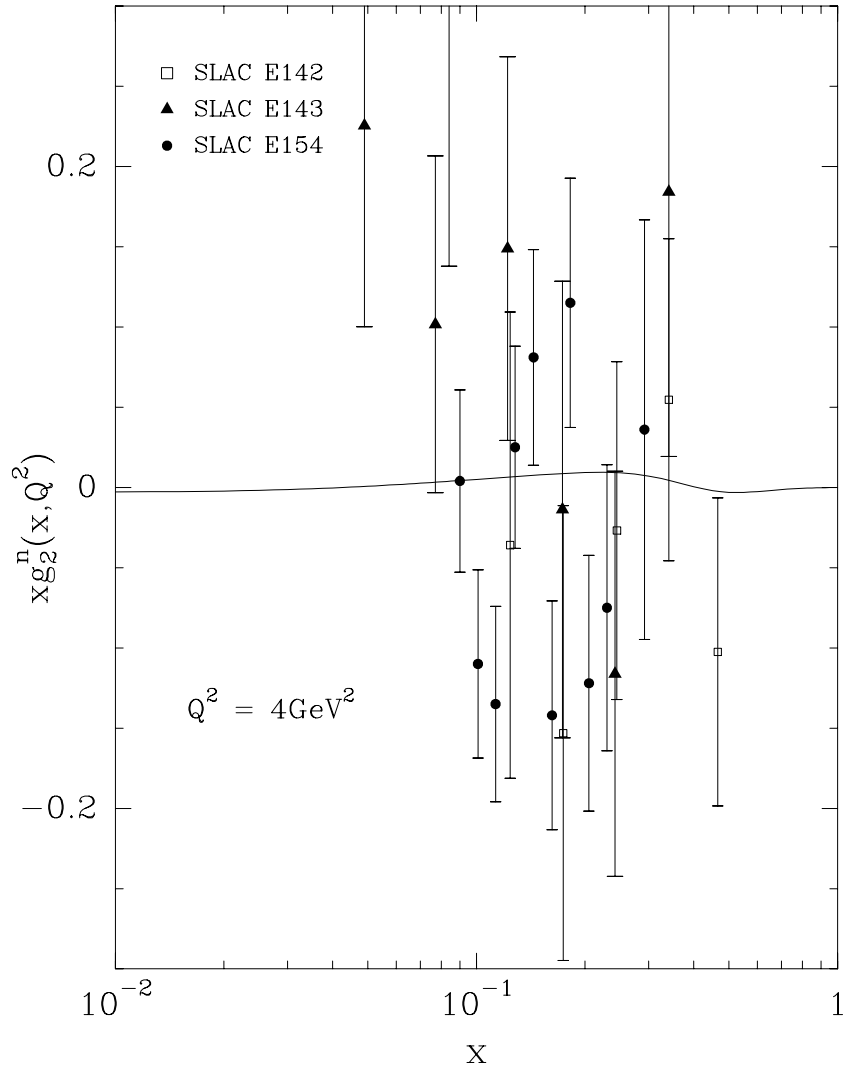


Figure 105: xg_2 for neutron as a function of x , for $Q^2 = 4\text{GeV}^2$. Data from E142, E143, E154 [66]-[72].

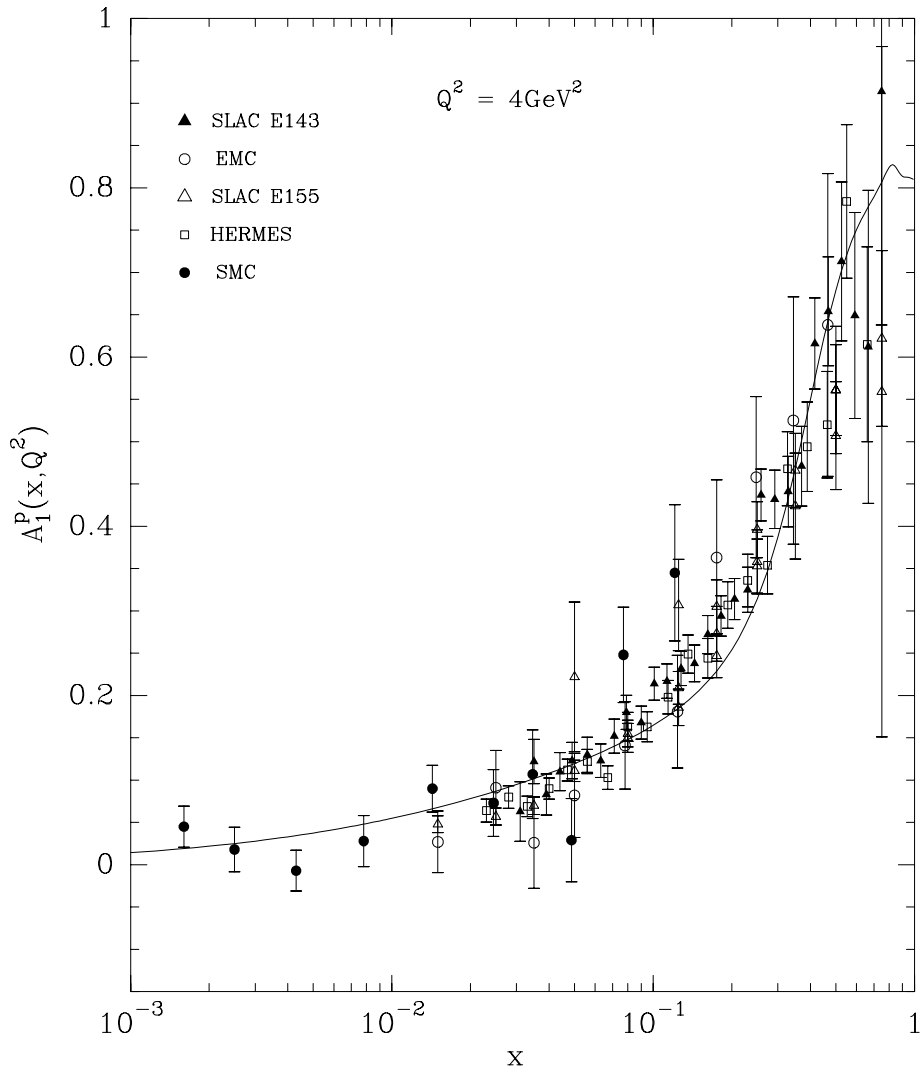


Figure 106: A_1^p as a function of x , for $Q^2 = 4\text{GeV}^2$. Data from E143[70], EMC[35], E155[76], HERMES[48], SMC[81].

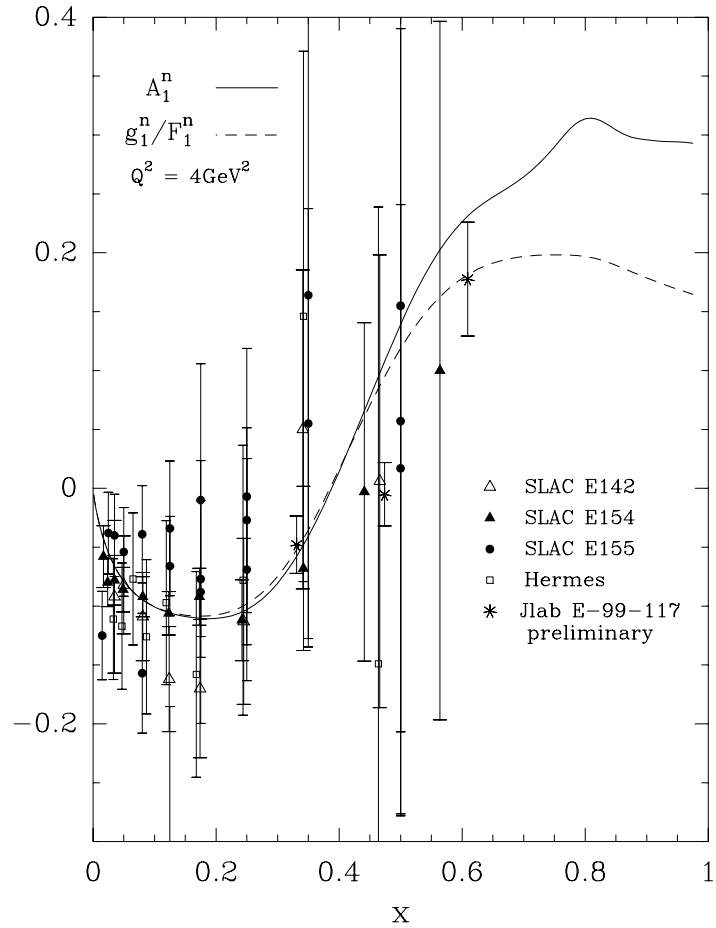


Figure 107: A_1^n as a function of x , for $Q^2 = 4\text{GeV}^2$ solid curve, g_1^n/F_1^n dashed curve. Data from E142[66], E155[76], E154[74], HERMES[49], Jlab E-99-117[53].

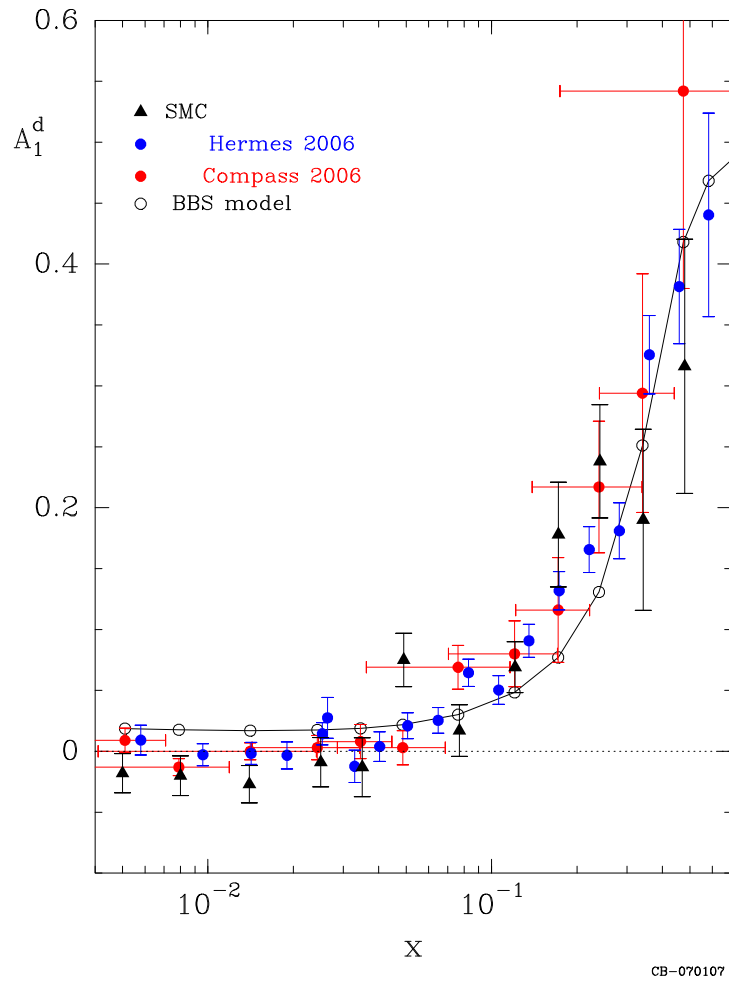


Figure 108: The longitudinal spin asymmetry A_1^d as a function of x . Data from Compass, Hermes, SMC Collaborations [113, 114, 115].

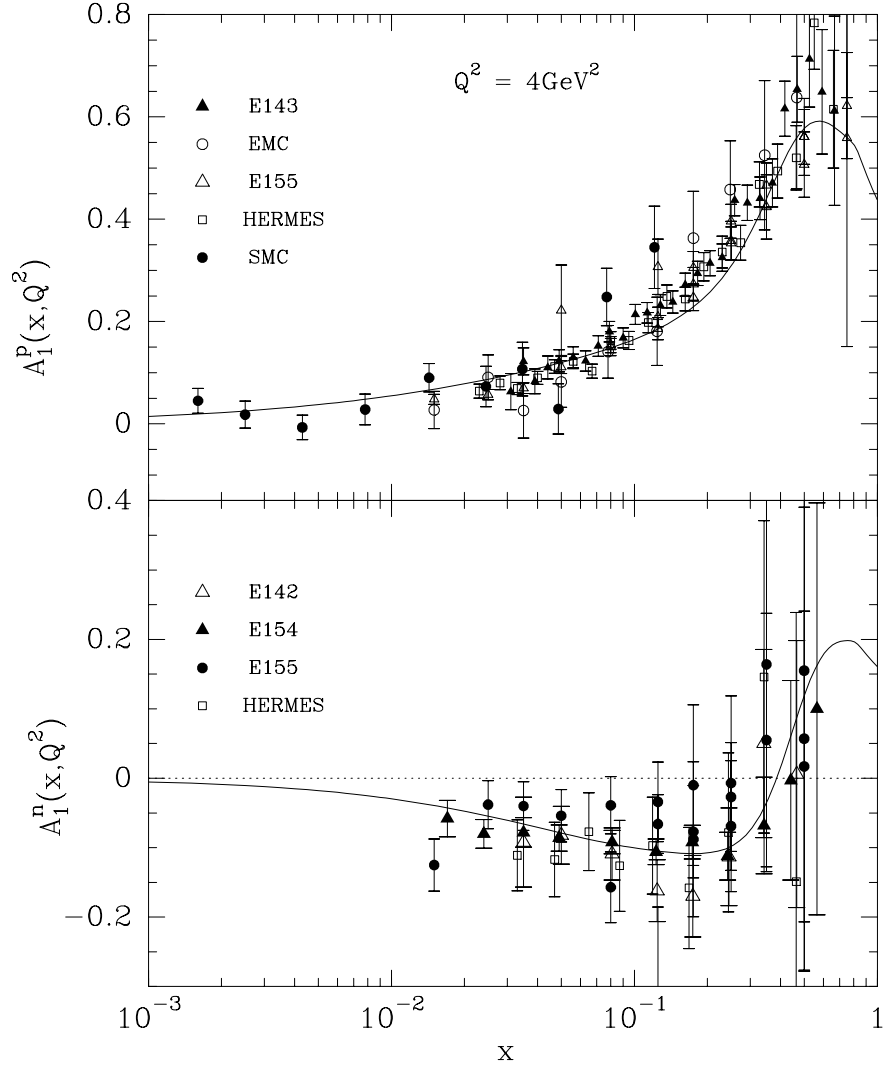


Figure 109: Compilation of the asymmetries A_1^p and A_1^n from E155, E154, E142, E143, EMC, SMC and HERMES experiments [33]-[69]. The curves correspond to our model predictions at $Q^2 = 4\text{GeV}^2$.

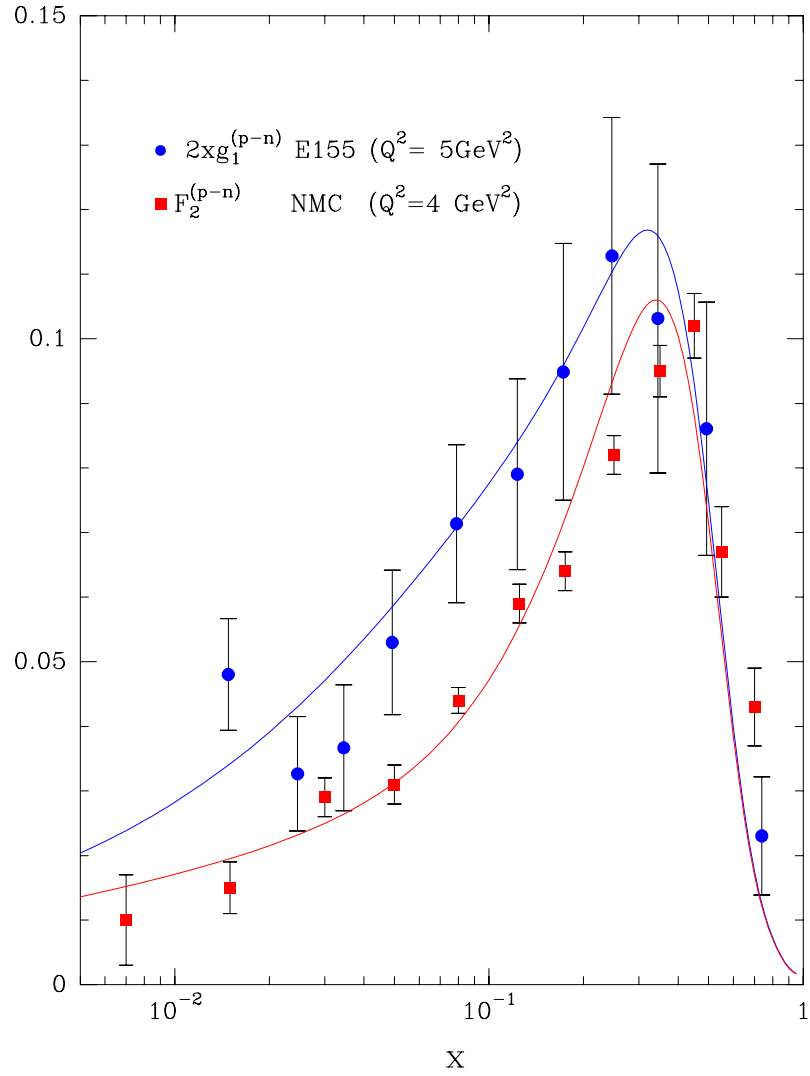


Figure 110: The quantities $2x(g_1^p - g_1^n)$ and $F_2^p - F_2^n$ as function of x at fixed $Q^2 = 4 - 5 \text{ GeV}^2$, calculated from E155, NMC Coll. Curves are model predictions.

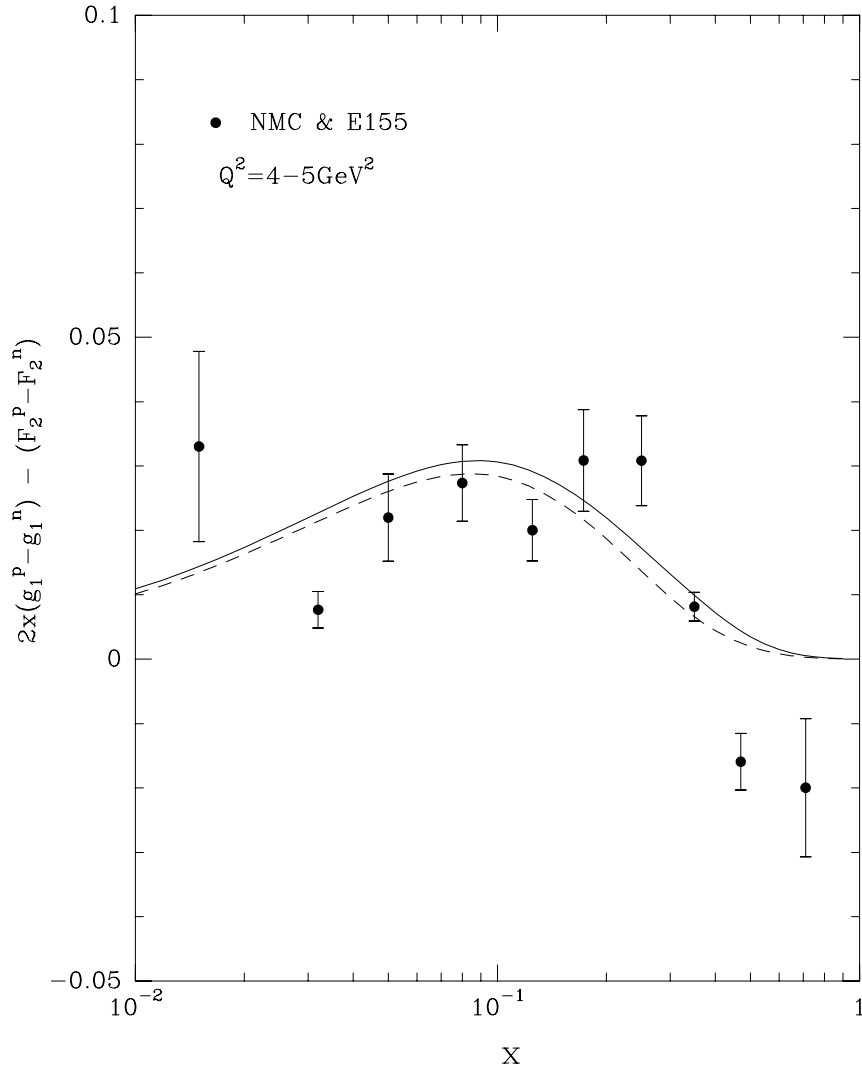


Figure 111: The quantity $2x(g_1^p - g_1^n) - (F_2^p - F_2^n)$ as function of x at fixed $Q^2 = 4 - 5 \text{ GeV}^2$, calculated from E155, NMC Coll. Comparison with the difference $d^- - u^-$ as a function of x , $Q^2 = 4 \text{ GeV}^2$. $2/3(d^- - u^- + \bar{d}^- - \bar{u}^-)$, solid curve, $2/3(\bar{d}^- - \bar{u}^-)$, dashed curve.

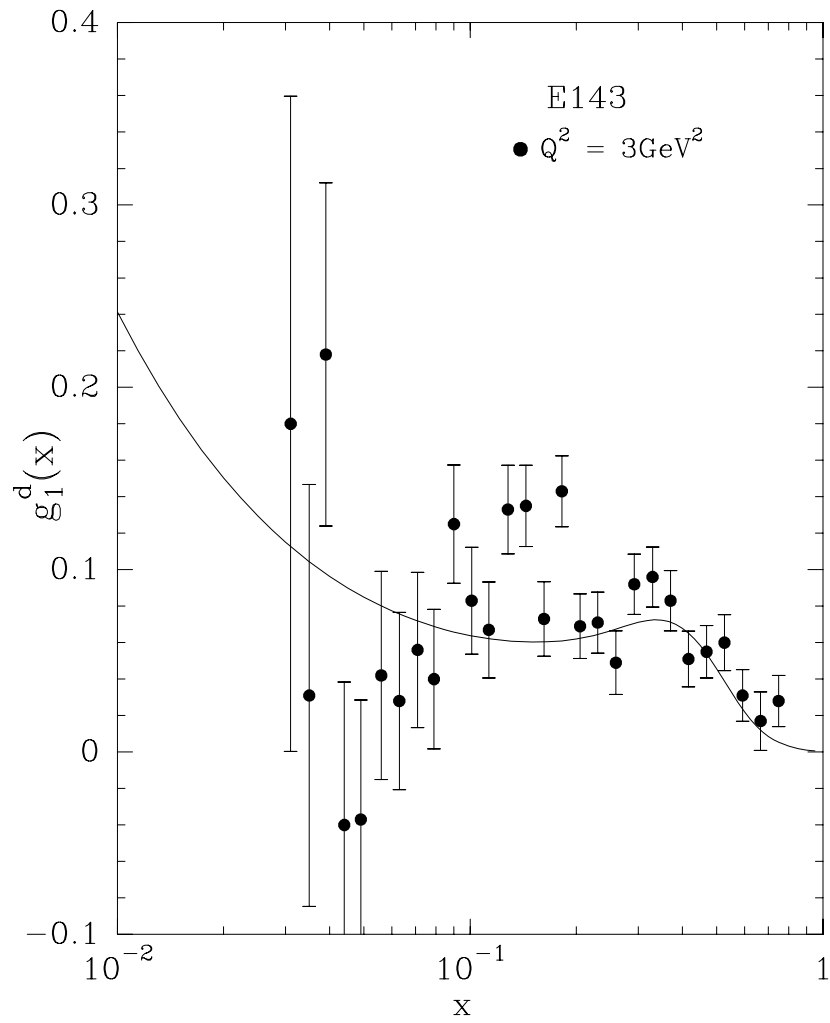


Figure 112: $g_1^d(x, Q^2)$ as function of x at fixed $Q^2 = 3\text{GeV}^2$, E143 Coll.

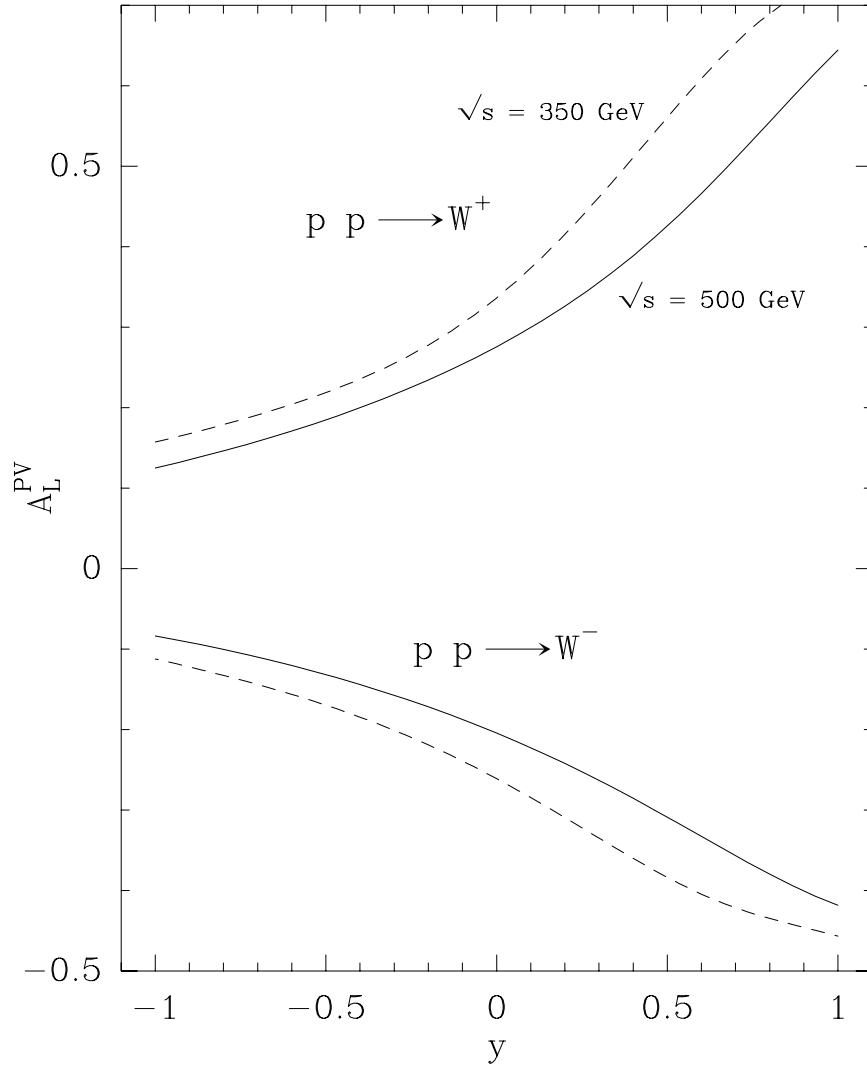


Figure 113: The parity violating asymmetry A_L^{PV} for $pp \rightarrow W^\pm$ production versus the rapidity y at $\sqrt{s} = 350, 500 \text{ GeV}$ (dashed, solid).

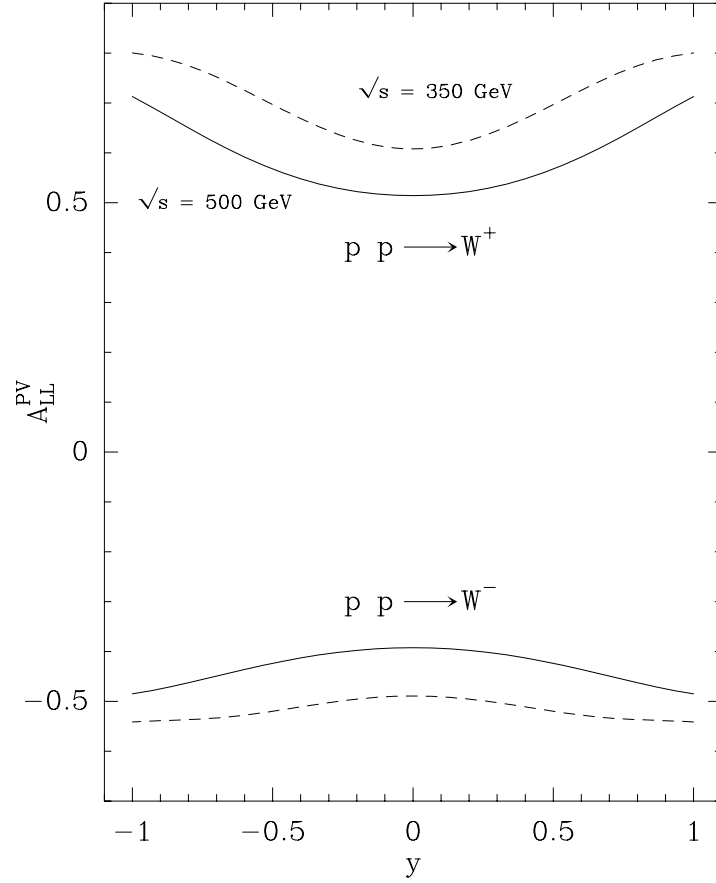


Figure 114: The parity violating asymmetry A_{LL}^{PV} versus the rapidity y for $pp \rightarrow W^{\pm}$ production at $\sqrt{s} = 350, 500$ GeV (dashed, solid).

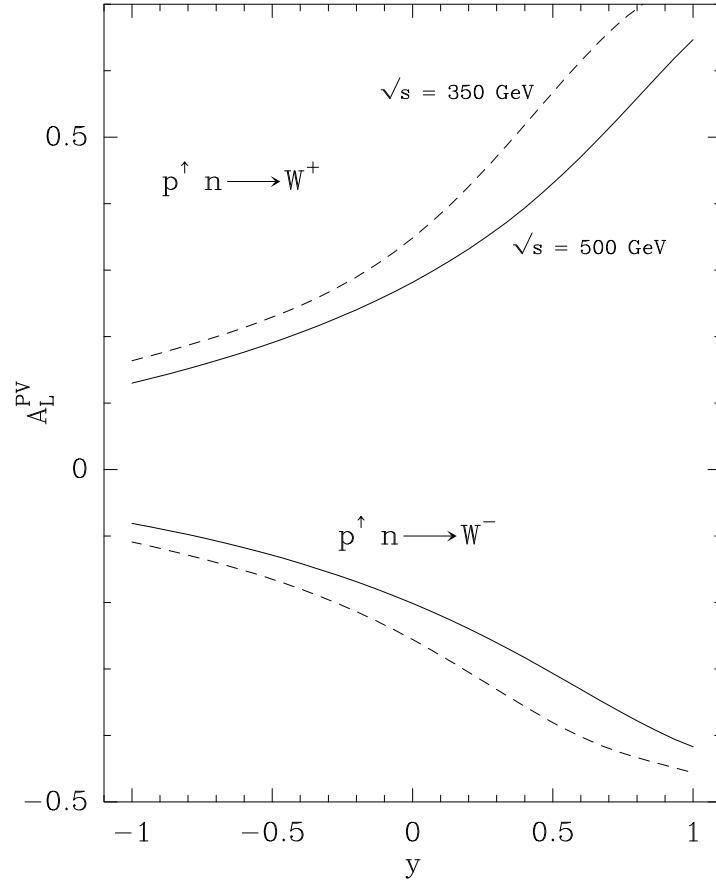


Figure 115: The parity violating asymmetry A_L^{PV} with polarized proton for $p^\uparrow n \rightarrow W^\pm$ production versus the rapidity y at $\sqrt{s} = 350, 500 \text{ GeV}$ (dashed, solid).

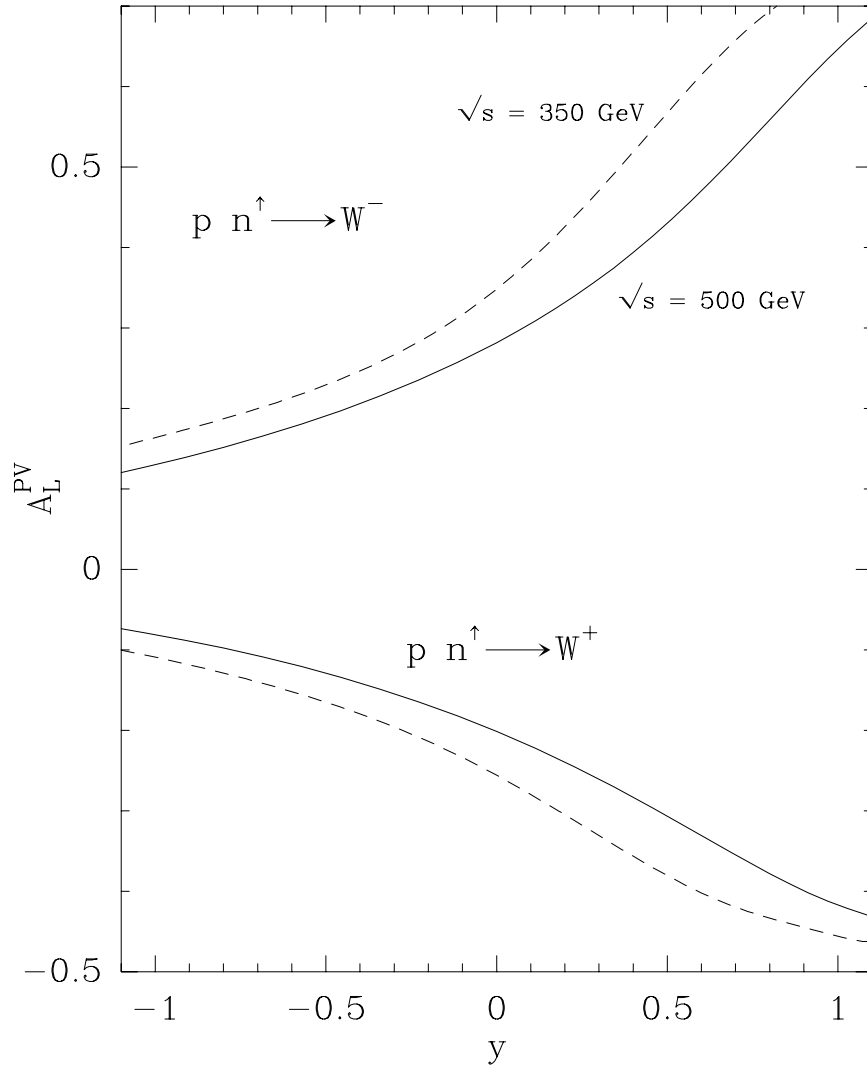


Figure 116: Parity violating asymmetry A_L^{PV} with a polarized neutron for $pn^\uparrow \rightarrow W^\pm$ production versus the rapidity y at $\sqrt{s} = 350, 500\text{GeV}$ (dashed, solid) .

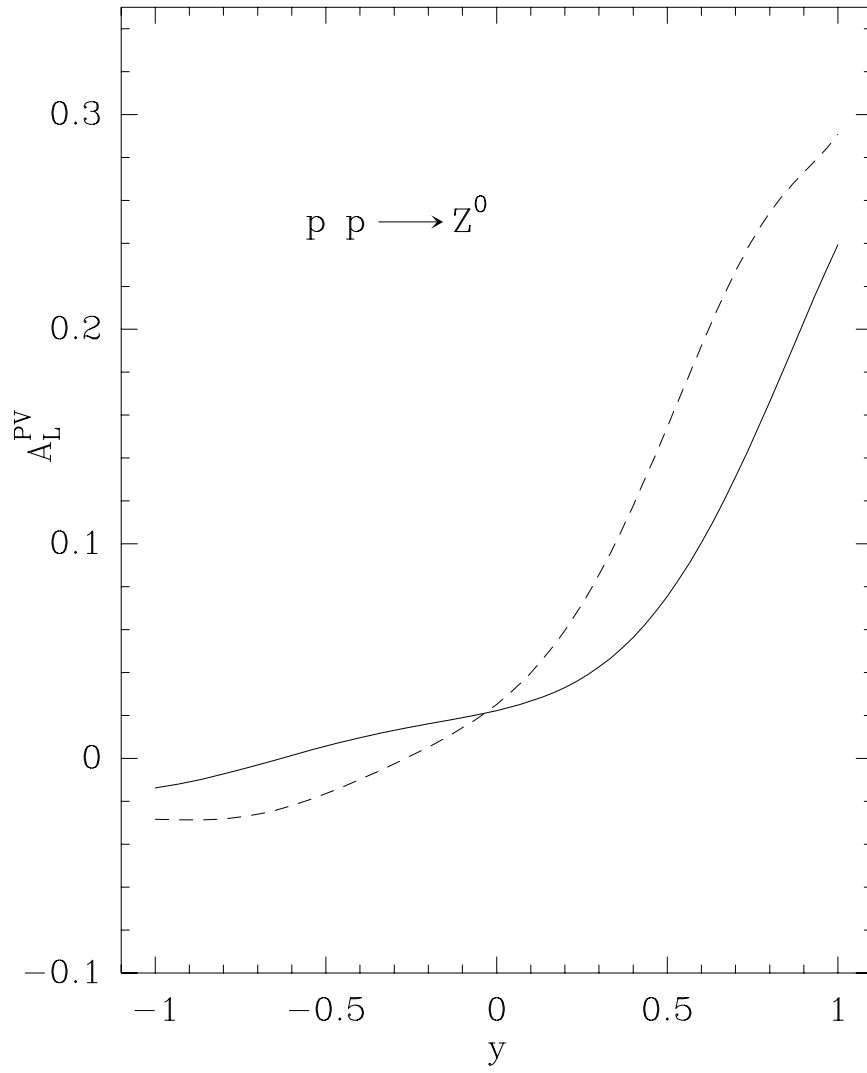


Figure 117: The parity violating asymmetry A_L^{PV} for $pp \rightarrow Z^0$ production versus the rapidity y at $\sqrt{s} = 350, 500\text{GeV}$ (dashed, solid).

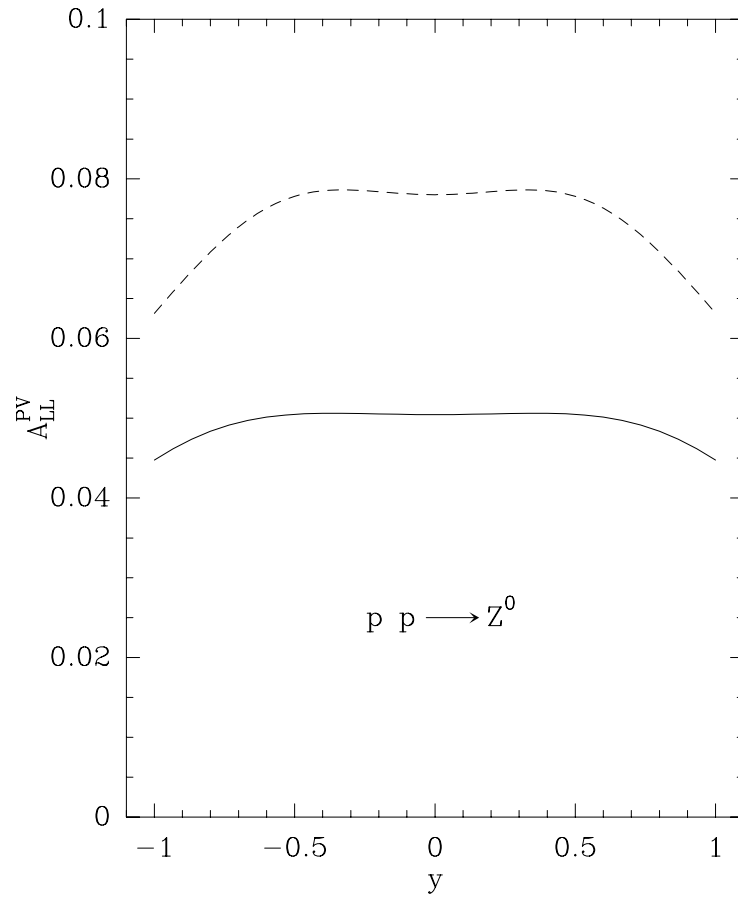


Figure 118: The parity violating asymmetry A_{LL}^{PV} versus the rapidity y for Z^0 production at $\sqrt{s} = 350, 500$ GeV (dashed, solid).

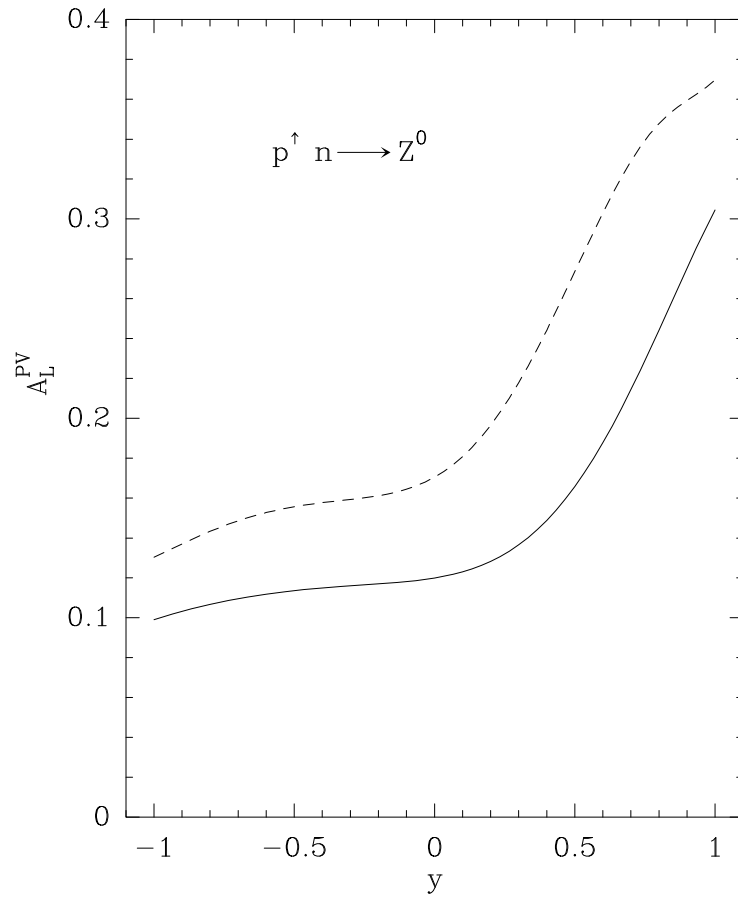


Figure 119: The parity violating asymmetry A_L^{PV} for $p^\uparrow n \rightarrow Z^0$ production versus the rapidity y at $\sqrt{s} = 350, 500\text{GeV}$ (dashed, solid).

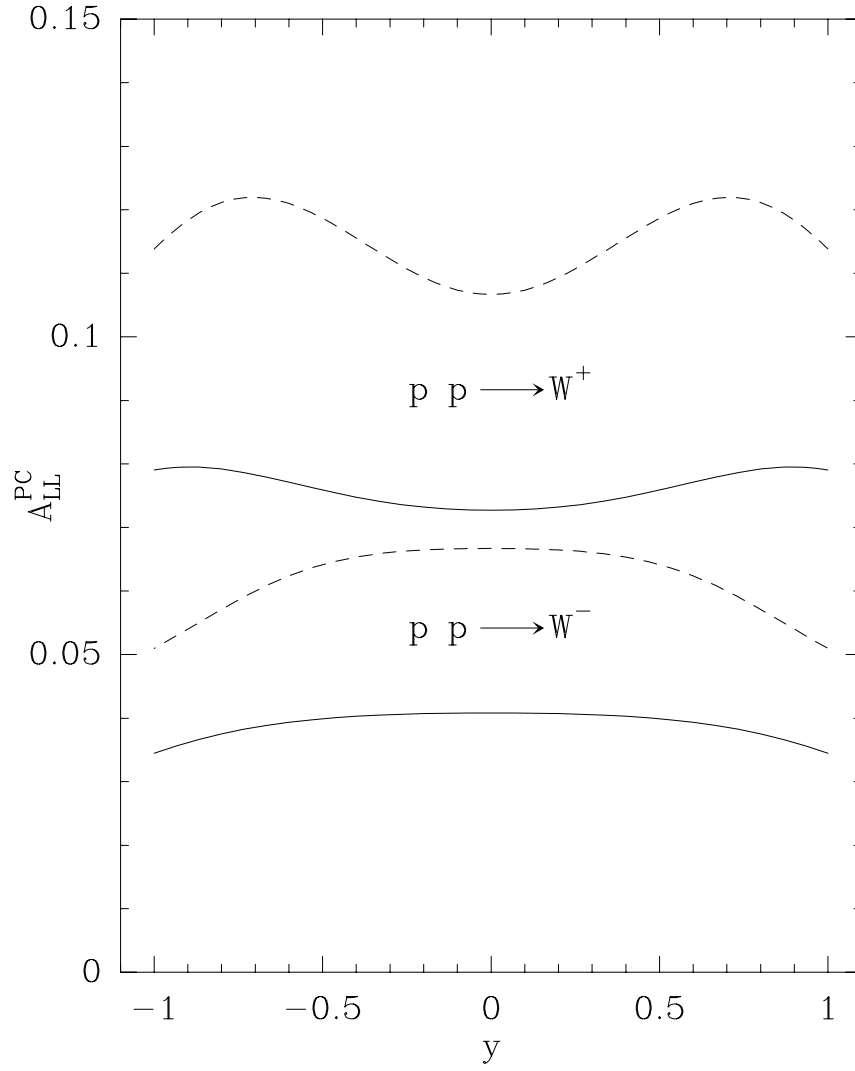


Figure 120: Parity conserving double helicity asymmetry A_{LL}^{PC} for $pp \rightarrow W^\pm$ production versus the rapidity y at $\sqrt{s} = 350, 500\text{GeV}$ (dashed, solid) .

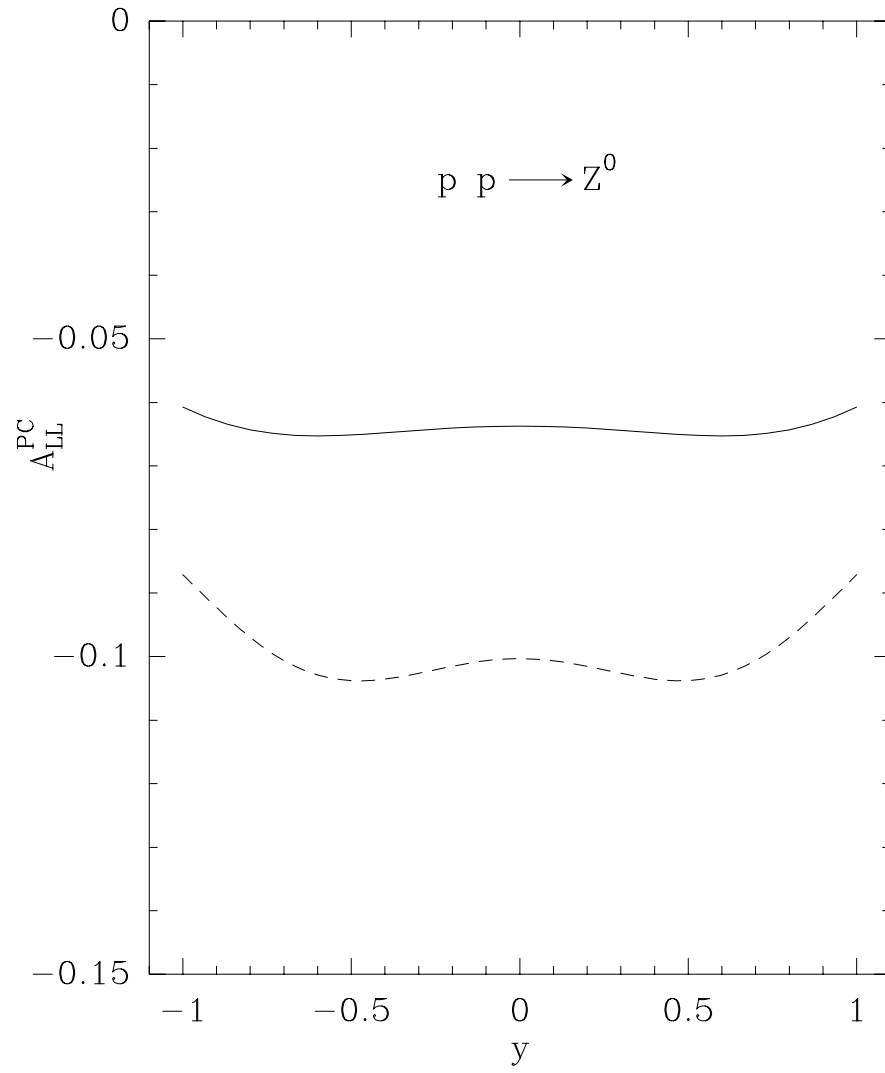


Figure 121: Parity conserving double helicity asymmetry A_{LL}^{PC} for $pp \rightarrow Z^0$ production versus the rapidity y at $\sqrt{s} = 350, 500\text{GeV}$ (dashed, solid) .

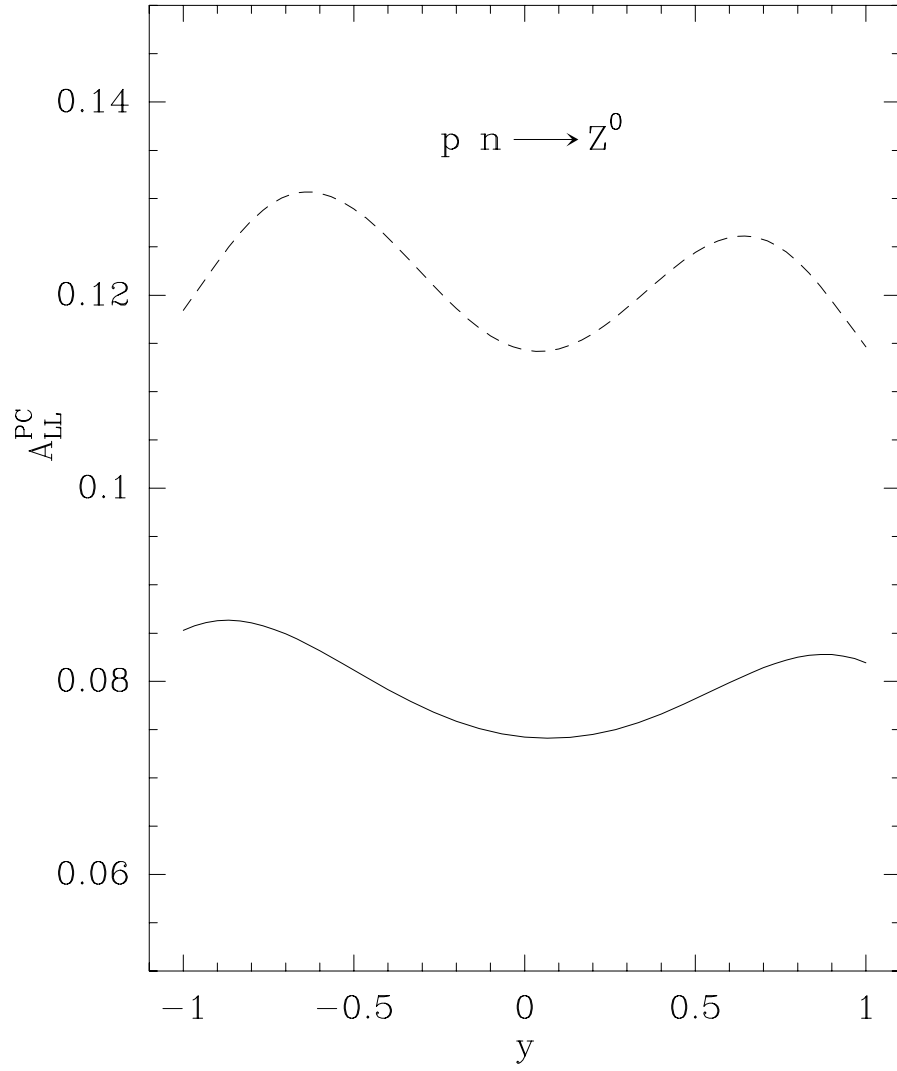


Figure 122: Parity conserving double helicity asymmetry A_{LL}^{PC} for $pn \rightarrow Z^0$ production versus the rapidity y at $\sqrt{s} = 350, 500\text{GeV}$ (dashed, solid) .

References

- [1] “A statistical approach for polarized parton distributions”
C. Bourrely, F. Buccella and J. Soffer, *Eur. Phys. J. C* **23** (2002) 487 (hep-ph/0109160).
- [2] “Recent tests for the statistical parton distributions”
C. Bourrely, F. Buccella and J. Soffer, *Mod. Phys. Lett. A* **18** (2003) 771 (hep-ph/0211389).
- [3] “Statistical approach for unpolarized fragmentation functions for the octet baryons”
C. Bourrely and J. Soffer, *Phys. Rev. D* **68** (2003) 014003 (hep-ph/0305070).
- [4] “The statistical parton distributions: status and prospects”
C. Bourrely, F. Buccella and J. Soffer, *Eur. Phys. J. C* **41** (2005) 327 (hep-ph/0502180).
- [5] “The extension to the transverse momentum of the statistical parton distributions”
C. Bourrely, F. Buccella and J. Soffer, *Mod. Phys. Lett. A* **21** (2006) 143 (hep-ph/0507328).
- [6] “Strangeness asymmetry of the nucleon in the statistical parton model”
C. Bourrely, F. Buccella and J. Soffer, *Phys. Lett. B* **648** (2007) 39 (hep-ph/0702221).
- [7] AFS Collaboration, E. Anassontzis *et al.*, *Sov. J. Nucl. Phys.* **51**, 836 (1990).
- [8] ALEPH Collaboration, D. Buskulic *et al.*, *Z. Phys. C* **66**, 355 (1995).
- [9] ALEPH Collaboration, R. Barate *et al.*, *Phys. Rep. C* **294**, 1 (1998).
- [10] P. Amaudruz *et al.*, *Nucl. Phys. B* **371**, 3 (1995).
- [11] BCDMS Collaboration, A. C. Benvenuti *et al.*, *Phys. Lett. B* **223**, 485 (1989).
- [12] BCDMS Collaboration, A. C. Benvenuti *et al.*, *Phys. Lett. B* **237**, 592 (1989) .

- [13] CCFR Collaboration, P. Z. Quintas *et al.*, Phys. Rev. Lett. **71**, 1307 (1993); W. C. Leung *et al.*, Phys. Lett. B **317**, 655 (1993); W. G. Seligman *et al.*, Phys. Rev. Lett. **79**, 1213 (1997); J. H. Kim *et al.*, Phys. Rev. Lett. **81**, 3595 (1998); U. K. Yang *et al.*, Phys. Rev. Lett. **86**, 2741 (2001).
- [14] CCFR Collaboration, A.O. Bazarko *et al.*, Z. Phys. C **65**, 189 (1995).
- [15] CELLO Collaboration, H. J. Behrend *et al.*, Z. Phys. C **46**, 397 (1990).
- [16] CLAS Collaboration, R. Fatemi *et al.*, Phys. Rev. Lett. **91**, 222002 (2003) [nucl-ex/0306019].
- [17] CDF Collaboration, T. Affolder *et al.*, Phys. Rev. D **64**, 032001 (2001).
- [18] D0 Collaboration, B. Abbott *et al.*, Phys. Rev. D **64**, 032003 (2001).
- [19] B. Dressler *et al.*, Eur. Phys. J. C **14**, 147 (2000).
- [20] DELPHI Collaboration, P. Abreu *et al.*, Nucl. Phys. B **444**, 3 (1995).
- [21] DELPHI Collaboration, P. Abreu *et al.*, Phys. Lett. B **318**, 249 (1993).
- [22] DELPHI Collaboration, P. Abreu *et al.*, Z. Phys. C **67**, 543 (1995).
- [23] FNAL E665 Collaboration, M. R. Adams *et al.*, Phys. Rev. D **54**, 3006 (1996)
- [24] FNAL E665 Collaboration, M. R. Adams *et al.*, Phys. Rev. Lett. **75**, 1466 (1996)
- [25] FNAL Nusea Collaboration, E. A. Hawker *et al.*, Phys. Rev. Lett. **80**, 3715 (1998); J. C. Peng *et al.*, Phys. Rev. D **58**, 092004 (1998); R. S. Towell *et al.*, Phys. Rev. D **64**, 052002 (2001)
- [26] FNAL E866/NuSea Collaboration, J.C. Webb *et al.*, submitted to Phys. Rev. Lett. [hep-ex/0302019].
- [27] FNAL E605 Collaboration, G. Moreno *et al.*, Phys. Rev. D **43**, 2815 (1991).
- [28] FNAL E772 Collaboration, P.L. McGaughey *et al.*, Phys. Rev. D **50**, 3038 (1994), D **60**, 119903 (1999).

- [29] CCFR Collaboration, U.K. Yang *et al.*, Phys. Rev. Lett. **87**, 251802 (2001); U.K. Yang Ph. D. Thesis, University of Rochester (2001).
- [30] NuTeVpack is available at www-nutev.phyast.pitt.edu/results_2004/nutev_sf.html
- [31] NuTeV Collaboration, D. Naples *et al.*, Proceedings from DIS03, St. Petersburg, Russia, April 2003. V. Radescu, XII International Workshop on Deep Inelastic Scattering, Slovakia (April 2004).
- [32] Experiment E94-110 at TJNAF, Z.-E. Meziani and P. Souder, update to E99-117, Z.-E. Meziani, J. P. Chen and P. Souder.
- [33] EMC Collaboration, J. Ashman *et al.*, Phys. Lett. B **206**, 364 (1988).
- [34] EMC Collaboration, J. Ashman *et al.*, Phys. Lett. B **206**, 364 (1988).
- [35] EMC Collaboration, Ashman *et al.*, Nuc. Phys. B **328**, 1 (1989).
- [36] EMC Collaboration, M. Arneodo *et al.*, Nucl. Phys. B **321**, 541 (1989).
- [37] H1 Collaboration, S. Aid *et al.*, Nucl. Phys. B **470**, 3 (1996); T. Ahmed *et al.*, Nucl. Phys. B **439**, 471 (1995); C. Adloff *et al.*, Nucl. Phys. B **497**, 3 (1996).
- [38] H1 Collaboration, C. Adloff *et al.*, Eur. Phys. J. C **13**, 609 (2000).
- [39] H1 Collaboration, S. Aid *et al.*, Nucl. Phys. B **449**, 3 (1995).
- [40] H1 Collaboration, C. Adloff *et al.*, Eur. Phys. J. C **19**, 269 (2001) [hep-ex/0012052].
- [41] H1 Collaboration, C. Adloff *et al.*, Eur. Phys. J. C **30**, 1 (2003) [hep-ex/0304003].
- [42] Z. Zhang, 'New insights into the proton structure with ep collider HERA', LAL 00-57 [hep-ph/0012249].
- [43] HERMES Collaboration, S. Belostotski, O. Grebenyuk and Yu. Naryshkin, Acta Physica Polonica B **33**, 3785 (2002).

- [44] HERMES Collaboration, K. Ackerstaff *et al.*, Phys. Lett. B **404**, 383 (1997); Phys. Lett. B **464**, 123 (1999); A. Airapetian *et al.*, Phys. Lett. B **442**, 484 (1998).
- [45] Jefferson Lab Hall A Collaboration, X. Zheng *et al.*, Phys. Rev. Lett. **92**, 012004 (2004).
- [46] HERMES Collaboration, A. Airapetian *et al.*, Phys. Rev. Lett. **92**, 012005 (2004) [hep-ex/0307064].
- [47] HERMES Collaboration, H.E. Jakson, Int. J. Mod. Phys. A **17**, 3551 (2002).
- [48] HERMES Collaboration, A. Airapetian *et al.*, Phys. Lett. B **442**, 484 (1998).
- [49] HERMES Collaboration, K. Ackerstaff *et al.*, Phys. Lett. B **404**, 383 (1997).
- [50] HRS Collaboration, P. Baringer *et al.*, Phys. Rev. Lett. **56**, 1346 (1986).
- [51] HRS Collaboration, M. Derick *et al.*, Phys. Rev. D **45**, 2639 (1987).
- [52] HRS Collaboration, T. L. Geld *et al.*, Phys. Rev. D **45**, 3949 (1992).
- [53] Jlab E99-117 Collaboration, X. Zheng *et al.*, Phys. Rev. Lett. **92**, 012004 (2004) [nuc-ex/0308011].
- [54] JLab E99-117 Collaboration, X. Zheng *et al.*, Phys. Rev. C **70**, 065207 (2004) [nucl-ex/0405006].
- [55] L3 Collaboration, M. Acciari *et al.*, Phys. Lett. B **328**, 223 (1994).
- [56] NMC Collaboration, M. Arneodo *et al.* Phys. Rev. D **50**, R1 (1994) and references therein; P. Amaudruz *et al.*, Phys. Rev. Lett. **66**, 2712 (1991); Nucl. Phys. B **371**, 3 (1995)
- [57] NMC Collaboration, D. Allasia *et al.*, Phys. Lett. B **258**, 493 (1991)
- [58] NMC Collaboration, M. Arneodo *et al.*, Phys. Lett. B **364**, 107 (1995); Nucl. Phys. B **483**, 3 (1997)
- [59] NMC Collaboration, M. Arneodo *et al.*, Phys. Rev. D **50** (1994) R1.

- [60] NMC Collaboration, M. Arneodo *et al.*, Phys. Rev. D **50**, R1 (1994) and references therein; Phys. Lett. B **364**, 107 (1995).
- [61] OPAL Collaboration, G. Alexander *et al.*, Z. Phys C **73**, 569 (1997); *ibid.* **73**, 587 (1997).
- [62] PHENIX Collaboration, S.S. Adler *et al.*, Phys. Rev. Lett. **91**, 241803 (2003) [hep-ex/0304038].
- [63] R806 Collaboration, C. Kourkoumalis *et al.*, Z. Phys. C **5**, 95 (1980).
- [64] SLAC E80 Collaboration, M. J. Alguard *et al.*, Phys. Lett. **37**, 1261 (1976); *ibidem* **41**, 70 (1978).
- [65] SLAC E130 Collaboration, G. Baum *et al.*, Phys. Rev. Lett. **51**, 1135 (1983).
- [66] SLAC E142 Collaboration, P.L. Anthony *et al.*, Phys. Rev. D **54**, 6620 (1996).
- [67] SLAC E142 Collaboration, P. L. Anthony *et al.*, Phys. Rev. Lett. **71**, 959; Phys. Rev. D **54**, 6620 (1996).
- [68] SLAC E143 Collaboration, K. Abe *et al.*, Phys. Lett. B **452**, 194 (1999).
- [69] SLAC E143 Collaboration, K. Abe *et al.*, Phys. Rev. Lett. **75**, 25 (1995); Phys. Rev. D **58**, 112003 (1998).
- [70] SLAC E143 Collaboration, K. Abe *et al.*, Phys. Rev. D **58**, 112003 (1998).
- [71] SLAC E143 Collaboration, K. Abe *et al.*, Phys. Rev. Lett. **74**, 346 (1995).
- [72] SLAC E154 Collaboration, K. Abe *et al.*, Phys. Lett. B **404**, 377 (1997).
- [73] SLAC E154 Collaboration, K. Abe *et al.*, Phys. Lett. B **405**, 180 (1997); Phys. Rev. Lett. **79**, 26 (1997)
- [74] SLAC E154 Collaboration, K. Abe *et al.*, Phys. Rev. Lett. **79**, 26 (1997).
- [75] SLAC E154 Collaboration, K. Abe *et al.* Phys. Lett. B **405**, 180 (1997).

- [76] SLAC E155 Collaboration, P. L. Anthony *et al.*, Phys. Lett. B **493**, 19 (2000).
- [77] SLAC E155 Collaboration, P.L. Anthony *et al.*, Phys. Lett. B **553**, 18 (2003) [hep-ex/0204028].
- [78] SLAC E155 Collaboration, P.L. Anthony *et al.*, Phys. Lett. B **458**, 529 (1999).
- [79] SLD Collaboration, K. Abe *et al.*, Phys. Rev. D **59**, 052001 (1999).
- [80] SMC Collaboration, B. Adeva *et al.*, Phys. Rev. D **58**, 112001 (1998); Phys. Rev. D **60**, 072004 (1999)
- [81] SMC Collaboration, Adeva *et al.*, Phys. Rev. D **60**, 072004 (1999).
- [82] Spin Muon Collaboration, D. Adams *et al.*, Phys. Lett. B **329**, 339 (1994); Erratum, Phys. Lett. B **339**, 332 (1994); *ibidem* B **396**, 338 (1997); B. Adeva *et al.*, Phys. Lett. B **412**, 414 (1997).
- [83] Spin Muon Collaboration, D. Adams *et al.* 1995 Phys. Lett. B **357**, 248 (1995); Phys. Rev. D **56**, 5330 (1997); B. Adeva *et al.*, Phys. Rev. D **58**, 112001 (1998).
- [84] A. Daleo, C.A. García Canal, G.A. Navarro and R. Sassot, Int. J. Mod. Phys. A **17**, 269 (2002) [hep-ph/0106156].
- [85] TASSO Collaboration, R. Brandelik *et al.*, Phys. Lett. B **105**, 75 (1981).
- [86] TASSO Collaboration, M. Althoff *et al.*, Z. Phys C **17**, 5 (1983).
- [87] TASSO Collaboration, M. Althoff *et al.*, Z. Phys C **27**, 27 (1985).
- [88] TASSO Collaboration, W. Braunschweig *et al.*, Z. Phys. C **42**, 189 (1989).
- [89] TASSO Collaboration, W. Braunschweig *et al.*, Z. Phys. C **45**, 209 (1990).
- [90] TPC Collaboration, H. Aihara *et al.*, Phys. Rev. Lett. **61**, 1263 (1988).
- [91] ZEUS Collaboration, M. Derrick *et al.*, Phys. Lett. B **345**, 576 (1995).

- [92] ZEUS Collaboration, M. Derrick *et al.*, Phys. Lett. B **316**, 412 (1993); Z. Phys. C **65**, 379 (1995); Z. Phys. C **72**, 399 (1996).
- [93] ZEUS Collaboration, J. Breitweg *et al.*, Eur. Phys. J. C **7**, 609 (1999).
- [94] ZEUS Collaboration, XXX Int. Conf. High Energy Phys. Osaka (Japan) July 2000, abstract 1049; J. Breitweg *et al.*, Eur. Phys. J. C **11**, 427 (1999).
- [95] ZEUS Collaboration, S. Chekanov *et al.*, Eur. Phys. J. c **28**, 175 (2003) [hep-ex/0208040].
- [96] ZEUS Collaboration, S. Chekanov *et al.*, Phys. Lett. B **539**, 197 (2002), Err. B **552**, 308 (2003) [hep-ex/0205091].
- [97] ZEUS Collaboration, S. Chekanov *et al.*, Eur. Phys. J. C **32**, 1 (2003) [hep-ex/0307043].
- [98] J. Soffer and O. Teryaev, Phys. Lett. B **490**, 106 (2000).
- [99] F. Zomer, Nucl. Phys. B (Proc. Suppl.) **79**, 115 (1999).
- [100] B.A. Kniehl, G. Kramer and B. Potter, Nucl. Phys. B **582**, 514 (2000).
- [101] J. Binnewies, B.A. Kniehl and B. Potter, Z. Phys. C **65**, 471 (1995).
- [102] COMPASS Collaboration, V.Y Alexakhin *et al.*, hep-ex/0609038.
- [103] M. Goncharov *et al.*, Phys. Rev. D **64** (2001) 112006.
- [104] M. Hirai, S. Kumano and N. Saito, Phys. Rev. D **74**, 014015 (2006).
- [105] D. de Florian, A. Navarro and R. Sassot, Phys. Rev. D **71**, 094018 (2005).
- [106] E. Leader, A.V. Sidorov and D.B. Stamenov, Phys. Rev. D **73**, 034023 (2006).
- [107] M. Glück, E. Reya, M. Stratmann and W. Vogelsang, Phys. Rev. D **63**, 094005 (2001).
- [108] A.D. Martin, R.G. Roberts, W.J. Stirling and R.S. Thorne, Eur. Phys. J. C **28**, 455 (2003).

- [109] V.Yu. Alexakhin *et al.* Compass Collaboration, Phys. Lett. B to be published, hep-ex/0609038.
- [110] A. Korzenev, Compass Collaboration, XV International Workshop on Deep-Inelastic Scattering and Related Subjects, April 2007, Munich, Germany. hep-ex/0704.3600.
- [111] C. Adloff *et al.*, H1 Collaboration, Eur. Phys. J. C **21**, 33 (2001).
- [112] C. Adloff *et al.*, H1 Collaboration, Phys. Lett. B **520**, 183 (2001).
- [113] V.Yu. Alexakhin *et al.*, Compass Collaboration, Phys. Lett. B **647**, 8 (2007).
- [114] A. Airapetian *et al.*, Hermes Collaboration, Phys. Rev. D **75**, 012007 (2007).
- [115] B. Adeva *et al.*, SMC Collaboration, Phys. Rev. D **58**, 112001 (1998).

List of Figures

1	The Fermi-Dirac functions for quarks $F_q^h = X_{0q}^h / (\exp[(x - X_{0q}^h)/\bar{x}] + 1)$ at the input energy scale $Q_0^2 = 4\text{GeV}^2$, as a function of x	8
2	The Fermi-Dirac functions for antiquarks $F_{\bar{q}}^h = 1/X_{0\bar{q}}^h (\exp[(x + X_{0\bar{q}}^h)/\bar{x}] + 1)$ at the input energy scale $Q_0^2 = 4\text{GeV}^2$, as a function of x	9
3	The different unpolarized parton distributions ($f = u, d, \bar{u}, \bar{d}, s, c$ and G) after NLO evolution, at $Q^2 = 20\text{GeV}^2$, as a function of x	10
4	Variation of d/u at large x , for $Q^2 = 4, 100\text{GeV}^2$	11
5	$xu(x, Q^2)$ as function of x for $Q^2 = 3000, 8000\text{GeV}^2$, data from H1 collaboration [41, 42].	12
6	$xd(x, Q^2)$ as function of x for $Q^2 = 3000, 8000\text{GeV}^2$, data from H1 collaboration [41, 42].	13
7	$c \cdot xu(x, Q^2)$ as function of Q^2 for different x bins, data from H1 collaboration [41, 42].	14
8	$c \cdot xd(x, Q^2)$ as function of Q^2 for different x bins, data from H1 collaboration [41, 42].	15
9	Comparison of the data on $\bar{d}/\bar{u}(x, Q^2)$ from E866/NuSea at $Q^2 = 54\text{GeV}^2$ [25], with the prediction of the statistical model (solid curve) and the set 1 of the parametrization proposed in Ref. [84] (dashed curve).	16
10	Difference $\bar{d} - \bar{u}$ as a function of x , $Q = 7.35\text{GeV}$, experimental results from FNAL-E866.	17
11	The strange quark distribution $xs(x, Q^2)$ determined at NLO as a function of x for different Q^2 values. Data from CCFR Collaboration [14].	18
12	The unpolarized and polarized strange quark and antiquark distributions determined at NLO as a function of x for $Q^2 = 4\text{GeV}^2$	19
13	The difference $s - \bar{s}$ quark distributions determined at NLO as a function of x for $Q^2 = 4, 20, 100\text{GeV}^2$	20
14	The different polarized parton distributions after NLO evolution, at $Q^2 = 20\text{GeV}^2$, as a function of x	21

15	The different helicity components of the light quark distributions after NLO evolution, at $Q^2 = 20\text{GeV}^2$, as a function of x	22
16	The different helicity components of the light antiquark distributions after NLO evolution, at $Q^2 = 20\text{GeV}^2$, as a function of x	23
17	Details of the polarized parton distributions g, s, c , after NLO evolution, at $Q^2 = 20\text{GeV}^2$, as a function of x	24
18	Quark helicity distributions at $\langle Q^2 \rangle = 2.5\text{GeV}^2$, as a function of x . Data from HERMES Coll. [46].	25
19	Flavor asymmetry $\Delta\bar{u} - \Delta\bar{d}$ of the light sea quark as a function of x , for $Q^2 = 2.5\text{GeV}^2$. Data from HERMES Coll. [46].	26
20	Flavor asymmetry $\Delta\bar{u} - \Delta\bar{d}$ of the light sea quark as a function of x , for $Q^2 = 4\text{GeV}^2$	27
21	$x\Delta u_v, x\Delta d_v, x\Delta\bar{q}$ as function of x at fixed $Q^2 = 10\text{GeV}^2$, experiment SMC Coll..	28
22	The sum of polarized valence quark distributions determined at NLO as a function of x for $Q^2 = 10\text{GeV}^2$, data from Compass Collaboration [109, 110].	29
23	Prediction for the integral $\Delta u_v + \Delta d_v$ determined at NLO as a function of the lower limit x for $Q^2 = 10\text{GeV}^2$	30
24	HERMES [44] and E99-117 [54] data on $(\Delta u + \Delta\bar{u})/(u + \bar{u})$, $(\Delta d + \Delta\bar{d})/(d + \bar{d})$, $\Delta q_s/q_s$ as function of x at fixed $Q^2 = 2.5\text{GeV}^2$. The curves are our model calculations. For the sea quarks $\Delta\bar{u}/\bar{u}$ (solid curve), $\Delta\bar{d}/\bar{d}$ (dashed curve) and $\Delta s/s$ (dotted curve).	31
25	Ratios $(\Delta u + \Delta\bar{u})/(u + \bar{u})$ and $(\Delta d + \Delta\bar{d})/(d + \bar{d})$ as a function of x for $Q^2 = 2.5\text{GeV}^2$. Data from Hermes [44] and JLab experiments [45].	32
26	Prediction of BBS PDF for the difference asymmetry $A^{h^+h^-}$ determined at NLO as a function of x for $Q^2 = 10\text{GeV}^2$, data from Compass Collaboration.	33
27	Ratio polarized/unpolarized quark distributions for u, d, s , at $Q^2 = 4\text{GeV}^2$	34
28	Ratio polarized/unpolarized antiquark distributions for $\bar{u}, \bar{d}, \bar{s}$ and G , at $Q^2 = 4\text{GeV}^2$	35
29	Spin components of gluon density	36

30	Comparison of $xG(x, Q^2)$ at $Q^2 = 20 - 30\text{GeV}^2$ (dashed-solid) with experimental determination from NMC [57], H1 [39] and ZEUS [91] experiments.	37
31	Positivity constraints between polarized and unpolarized distributions according to the inequality of Soffer-Teryaev [98].	38
32	The u quark to proton fragmentation function $D_u^p(x, Q^2)$ as a function of x at $Q^2 = 25\text{GeV}^2$. The experimental data are from Ref. [36].	39
33	The fragmentation function for u quark to Λ , $D_u^\Lambda(x, Q^2)$, as a function of x at $Q^2 = 2.5\text{GeV}^2$. The experimental data are from Ref. [43].	40
34	The quark to octet baryons fragmentation functions $D_q^B(x, Q^2)$ and $D_Q^B(x, Q^2)$ ($B = p, \Lambda, \Sigma^\pm, \Xi^-$, $q = u, d, s$ and $Q = c, b, t$), as a function of x at $Q = 91.2\text{GeV}$. Note that we used different vertical scales in the upper and lower parts of the figure.	41
35	$F_2^p(x, Q^2)$ as function of Q^2 for fixed x , E665 data [23]. The function $c(x_i) = 0.6(19 - i)$, $i = 1$ corresponds to $x = 8.9 \cdot 10^{-4}$	43
36	$F_2^p(x, Q^2)$ as function of Q^2 for fixed x , H1 data [37, 38]. The function $c(x_i) = 0.6(19 - i)$, $i = 1$ corresponds to $x = 1.78 \cdot 10^{-4}$	44
37	$F_2^p(x, Q^2)$ as function of Q^2 for fixed x , H1 Coll. The function $c(x_i) = 0.6(19 - i)$, $i = 1$ corresponds to $x = 0.003$	45
38	$F_2^p(x, Q^2)$ as function of Q^2 for fixed x , ZEUS data [92, 93]. The function $c(x_i) = 0.6(19 - i)$, $i = 1$ corresponds to $x = 6.3 \cdot 10^{-5}$	46
39	$F_2^p(x, Q^2)$ as function of Q^2 for fixed x , BCDMS Coll. [11, 12]. The function $c(x_i) = 0.6(19 - i)$, $i = 1$ corresponds to $x = 0.07$	47
40	$F_2^p(x, Q^2)$ as function of Q^2 for fixed x , NMC Coll. The function $c(x_i) = 0.6(19 - i)$, $i = 1$ corresponds to $x = 4.5 \cdot 10^{-3}$	48
41	$F_2^p(x, Q^2)$ as function of Q^2 for fixed x , NMC Coll. The function $c(x_i) = 0.6(19 - i)$, $i = 1$ corresponds to $x = 9 \cdot 10^{-2}$	49
42	$F_2^p(x, Q^2)$ as function of Q^2 for fixed x , $c(x) = 0.6(i_x - 0.4)$, $i_x = 1 \rightarrow x = 0.32$, rebinned data H1, ZEUS, E665, NMC, BCDMS. (Presentation of data, courtesy of R. Voss).	50
43	Ratio F_2^n/F_2^p as a function of x for different Q^2 values, data are from NMC and E665 Coll. Difference $F_2^p - F_2^n$ as a function of x for $Q^2 = 4\text{GeV}^2$, data are from NMC Coll.. The curves are shown for $Q^2 = 4\text{GeV}^2$	51

44	$F_2^d(x, Q^2)$ as function of Q^2 for fixed x , NMC data [58]. The function $c(x_i) = 0.6(19 - i)$, $i = 1$ corresponds to $x = 4.5 \cdot 10^{-3}$.	52
45	$F_2^d(x, Q^2)$ as function of Q^2 for fixed x , BCDMS data [12]. The function $c(x_i) = 0.6(19 - i)$, $i = 1$ corresponds to $x = 7 \cdot 10^{-2}$.	53
46	$F_2^d(x, Q^2)$ as function of Q^2 for fixed x , E665 data [23]. The function $c(x_i) = 0.6(19 - i)$, $i = 1$ corresponds to $x = 8.9 \cdot 10^{-4}$.	54
47	Prediction of the partial derivative $\partial F_2^p(x, Q^2)/\partial \ln(Q^2)$ for fixed x as a function of Q^2 . Data from H1 Collaboration [111].	55
48	Prediction of the partial derivative $\partial F_2^p(x, Q^2)/\partial \ln(Q^2)$ for $Q^2 = 10 \text{ GeV}^2$ as a function of x . Data from H1 Collaboration [111].	56
49	Prediction of the partial derivative $-\partial \ln F_2^p(x, Q^2)/\partial \ln(x)$ for fixed Q^2 as a function of x . Data from H1 Collaboration [112].	57
50	F_2^p partial derivative $\lambda(x, Q^2)$ as a function of Q^2 , the shaded surface represents the allowed domain for $10^{-4} \leq x \leq 10^{-2}$, predicted by the statistical model. Data from H1 Collaboration [112].	58
51	Prediction of the structure function F_L for different Q^2 as a function of x . Data from H1 Collaboration [111].	59
52	$x F_3^{\nu N}(x, Q^2)$ as function of x for low Q^2 values, CCFR Coll. The curves are for $Q^2 = 4, 12.6 \text{ GeV}^2$, solid, dashed respectively.	60
53	$x F_3^{\nu N}(x, Q^2)$ as function of Q^2 for fixed x , CCFR data [13]. The function $c(x_i) = 0.6(19 - i)$, $i = 1$ corresponds to $x = 7.5 \cdot 10^{-3}$.	61
54	The structure function $x F_3^{NC}$ as a function of x , for different Q^2 . Data from ZEUS Coll. [95], H1 Coll. [40].	62
55	Charged-current total cross section νN for an isoscalar nucleon as a function of the neutrino energy.	63
56	Theoretical calculations for the ratio $R_W(y) = (d\sigma^{W^+}/dy)/(d\sigma^{W^-}/dy)$ for pp versus the W rapidity, at two RHIC-BNL energies. Solid curve ($\sqrt{s} = 500 \text{ GeV}$) and dashed curve ($\sqrt{s} = 200 \text{ GeV}$) are the statistical model predictions. Dotted curve ($\sqrt{s} = 500 \text{ GeV}$) and dashed-dotted curve ($\sqrt{s} = 200 \text{ GeV}$) are the predictions obtained using the $\bar{d}(x)/\bar{u}(x)$ ratio from Ref. [84].	64
57	Cross sections for proton production in e^+e^- annihilation at several energies as function of x_E . The experimental data are from Refs. [8, 20, 79, 86, 90, 88].	65

58	Cross sections for Λ production in e^+e^- annihilation at several energies, as function of x_E . The experimental data are from Refs. [15, 9, 21, 61, 55, 79, 85, 87, 89, 50, 51, 52].	66
59	Cross sections for Σ^\pm production in e^+e^- annihilation at the Z-pole as function of x_E . The experimental data are from Ref. [61].	67
60	Cross sections for Ξ^- production in e^+e^- annihilation at the Z-pole as function of x_E . The experimental data are from Refs. [9, 61, 22].	68
61	Drell-Yan cross sections per nucleon at $\sqrt{s} = 38.8\text{GeV}$ for pp , pd , and pCu as a function of M for selected x_F bins. Experimental data are from Refs. [26, 27, 28].	69
62	Drell-Yan cross sections per nucleon at $\sqrt{s} = 38.8\text{GeV}$ for pp and pd as a function of M for selected x_F bins. Experimental data are from Refs. [26, 27].	70
63	Drell-Yan cross sections ratios experiment vs theory at $\sqrt{s} = 38.8\text{GeV}$ for pp , pd , and pCu as a function of M for selected x_F bins. Experimental data are from Refs. [26, 27, 28].	71
64	Drell-Yan cross sections per nucleon at $\sqrt{s} = 38.8\text{GeV}$ for pp and pd as a function of x_F for selected M bins. Experimental data are from Ref. [26].	72
65	Drell-Yan cross sections per nucleon at $\sqrt{s} = 38.8\text{GeV}$ for pp and pd as a function of x_F for selected M bins. Experimental data are from Ref. [26].	73
66	Cross section for single jet production in $\bar{p}p$ at $\sqrt{s} = 1.8\text{TeV}$ as a function of E_T . Data from CDF [17] and D0 [18] collaborations.	74
67	Inclusive π^0 production in pp reaction at $\sqrt{s} = 63\text{GeV}$ as a function of p_T . Data from AFS [7] and R806 [63] Collaborations. Solid curve scale $\mu = p_T/2$, dashed $\mu = p_T$, fragmentation functions from KKP [100].	75
68	Inclusive π^0 production in pp reaction at $\sqrt{s} = 63\text{GeV}$ as a function of p_T . Data from AFS [7] and R806 [63] Collaborations. Solid curve scale $\mu = p_T/2$, dashed $\mu = p_T$, fragmentation functions BKP [101].	76
69	Inclusive π^0 production in pp reaction at $\sqrt{s} = 200\text{GeV}$ as a function of p_T , scale $\mu = p_T$. Data from Phenix Collaboration [62]. Solid curve fragmentation functions from KKP [100], dashed curve BKP [101].	77

70	The reduced charged current cross section, $\tilde{\sigma}$, in e^-p reaction as a function of x , for different fixed values of Q^2 . Data from H1 Coll. [40].	78
71	The reduced charged current cross section, $\tilde{\sigma}$, in e^-p reaction as a function of Q^2 , for different fixed values of x . Data from H1 Coll. [40].	79
72	The reduced charged current cross section, $\tilde{\sigma}$, in e^+p reaction as a function of x , for different fixed values of Q^2 . Data from H1 Coll. [41].	80
73	The reduced charged current cross section, $\tilde{\sigma}$, in e^+p reaction as a function of Q^2 , for different fixed values of x . Data from H1 Coll. [41].	81
74	The reduced charged current cross section, $\tilde{\sigma}$, in e^-p reaction as a function of x , for different fixed values of Q^2 . Data from ZEUS Coll. [96].	82
75	The reduced charged current cross section, $\tilde{\sigma}$, in e^-p reaction as a function of Q^2 , for different fixed values of x . Data from ZEUS Coll. [96].	83
76	The reduced charged current cross section, $\tilde{\sigma}$, in e^+p reaction as a function of x , for different fixed values of Q^2 . Data from ZEUS Coll. [97].	84
77	The reduced charged current cross section, $\tilde{\sigma}$, in e^+p reaction as a function of Q^2 , for different fixed values of x . Data from ZEUS Coll. [97].	85
78	The reduced neutral current cross section $\tilde{\sigma}$, in e^-p reaction as a function of x , for different fixed values of Q^2 and $\sqrt{s} = 320\text{GeV}$. Data from H1 Coll [40]	86
79	The reduced neutral current cross section $\tilde{\sigma}$, in e^+p reaction as a function of x , for different fixed values of Q^2 and $\sqrt{s} = 319\text{GeV}$. Data from H1 Coll [40]	87
80	The reduced neutral current cross section $\tilde{\sigma}$, in $e^\pm p$ reaction as a function of Q^2 , for different fixed values of x . Solid line e^-p , dashed line e^+p . Data from H1 Coll [40]	88
81	The reduced neutral current cross section $\tilde{\sigma}$, in e^-p reaction as a function of x , for different fixed values of Q^2 and $\sqrt{s} = 318\text{GeV}$. Data from Zeus Coll [97]	89

82	The reduced neutral current cross section $\tilde{\sigma}$, in e^+p reaction as a function of x , for different fixed values of Q^2 and $\sqrt{s} = 318\text{GeV}$. Data from Zeus Coll [97]	90
83	The reduced neutral current cross section $\tilde{\sigma}$, in $e^\pm p$ reaction as a function of Q^2 , for different fixed values of x . Solid line e^-p , dashed line e^+p . Data from Zeus Coll [97]	91
84	Differential cross section νN proton for $E_\nu = 85\text{GeV}$ as a function of y for different x bins. Data from CCFR [29] and NuTeV collaboration [31, 30].	92
85	Differential cross section νN proton for $E_\nu = 85\text{GeV}$ as a function of y for different x bins. Data from CCFR [29] and NuTeV collaboration [31, 30].	93
86	The reduced harged current cross section νN , for different x bins as a function of Q^2 . The data points are obtained from the differential cross section [31, 30], they are not a direct measurement	94
87	Comparison of the CCFR ν data [103] to the result of the fit for $d\sigma/dxdy$, in units of charged-current σ , for various kinematic ranges in energy, x and y	95
88	Comparison of the CCFR $\bar{\nu}$ data [103] to the result of the fit for $d\sigma/dxdy$ in units of charged-current σ , for various kinematic ranges in energy, x and y	96
89	Comparison of the NuTeV ν data [103] to the result of the fit for $d\sigma/dxdy$, in units of charged-current σ , for various kinematic ranges in energy, x and y	97
90	Comparison of the NuTeV $\bar{\nu}$ data [103] to the result of the fit for $d\sigma/dxdy$, in units of charged-current σ , for various kinematic ranges in energy, x and y	98
91	$g_1^p(x, Q^2)$ as function of x at for a range $1.1 \leq Q^2 \leq 1.64\text{GeV}^2$, CLAS Coll [16]. The two curves represent the extreme Q^2 values.	100
92	$g_1^p(x, Q^2)$ as function of x at fixed $Q^2 = 3\text{GeV}^2$, E143 Coll. . .	101
93	$g_1^p(x, Q^2)$ as function of x at fixed $Q^2 = 5\text{GeV}^2$, E155 Coll. . .	102
94	$g_1^p(x, Q^2)$ as function of x at fixed $Q^2 = 10\text{GeV}^2$, evolved SMC data.	103
95	Behavior of $g_1^p(x, Q^2)$ at low x and fixed $Q^2 = 5\text{GeV}^2$,	104
96	$g_1^n(x, Q^2)$ as function of x at fixed $Q^2 = 3\text{GeV}^2$, E143 Coll. . .	105
97	$g_1^n(x, Q^2)$ as function of x at fixed $Q^2 = 5\text{GeV}^2$, E154, E155, JLab Coll.	106

98	$g_1^d(x, Q^2)$ as function of x at fixed $Q^2 = 10\text{GeV}^2$, evolved SMC data.	107
99	$g_1^p(x, Q^2) - g_1^n(x, Q^2)$ as function of x at fixed $Q^2 = 5\text{GeV}^2$, E155 Coll..	108
100	$g_1^{p,d,n}(x, Q^2)$ as function of x for different Q^2 values, from E155, E154, E143, SMC, HERMES experiments. The curves correspond to our model predictions at $Q^2 = 5\text{GeV}^2$	109
101	$g_1^{p,d,n}(x, Q^2)$ at large x values for different Q^2 values, from E155, E154, E143, SMC, HERMES, Jlab experiments. The curves correspond to our model predictions at $Q^2 = 5\text{GeV}^2$	110
102	$2^n g_1^p(x, Q^2)$ as function of Q^2 for different x values. $n = 0$ corresponds to $x = 0.75$ and $n = 16$ to $x = 7.5 \cdot 10^{-3}$. Experimental data are rebined to the nearest x values.	111
103	$g_1^n(x, Q^2)$ as function of Q^2 for different x values. The function $c(x_i) = 19 - i$, $i = 0$ corresponds to $x = 7.5 \cdot 10^{-3}$. Experimental data are rebined to the nearest x values.	112
104	xg_2 for proton and neutron as a function of x , for $Q^2 = 4\text{GeV}^2$. Data from SLAC E155 [77], JLab E99-117 [54].	113
105	xg_2 for neutron as a function of x , for $Q^2 = 4\text{GeV}^2$. Data from E142, E143, E154 [66]-[72].	114
106	A_1^p as a function of x , for $Q^2 = 4\text{GeV}^2$. Data from E143[70], EMC[35], E155[76], HERMES[48], SMC[81].	115
107	A_1^n as a function of x , for $Q^2 = 4\text{GeV}^2$ solid curve, g_1^n/F_1^n dashed curve. Data from E142[66], E155[76], E154[74], HERMES[49], Jlab E-99-117[53].	116
108	The longitudinal spin asymmetry A_1^d as a function of x . Data from Compass, Hermes, SMC Collaborations [113, 114, 115].	117
109	Compilation of the asymmetries A_1^p and A_1^n from E155, E154, E142, E143, EMC, SMC and HERMES experiments [33]-[69]. The curves correspond to our model predictions at $Q^2 = 4\text{GeV}^2$	118
110	The quantities $2x(g_1^p - g_1^n)$ and $F_2^p - F_2^n$ as function of x at fixed $Q^2 = 4 - 5\text{GeV}^2$, calculated from E155, NMC Coll. Curves are model predictions.	119
111	The quantity $2x(g_1^p - g_1^n) - (F_2^p - F_2^n)$ as function of x at fixed $Q^2 = 4 - 5\text{GeV}^2$, calculated from E155, NMC Coll. Comparison with the difference $d^- - u^-$ as a function of x , $Q^2 = 4\text{GeV}^2$. $2/3(d^- - u^- + \bar{d}^- - \bar{u}^-)$, solid curve, $2/3(\bar{d}^- - \bar{u}^-)$, dashed curve.	120
112	$g_1^d(x, Q^2)$ as function of x at fixed $Q^2 = 3\text{GeV}^2$, E143 Coll.	121

113	The parity violating asymmetry A_L^{PV} for $pp \rightarrow W^\pm$ production versus the rapidity y at $\sqrt{s} = 350, 500\text{GeV}$ (dashed, solid). . .	122
114	The parity violating asymmetry A_{LL}^{PV} versus the rapidity y for $pp \rightarrow W^\pm$ production at $\sqrt{s} = 350, 500\text{GeV}$ (dashed, solid). . .	123
115	The parity violating asymmetry A_L^{PV} with polarized proton for $p^\uparrow n \rightarrow W^\pm$ production versus the rapidity y at $\sqrt{s} = 350, 500\text{GeV}$ (dashed, solid).	124
116	Parity violating asymmetry A_L^{PV} with a polarized neutron for $pn^\uparrow \rightarrow W^\pm$ production versus the rapidity y at $\sqrt{s} = 350, 500\text{GeV}$ (dashed, solid)	125
117	The parity violating asymmetry A_L^{PV} for $pp \rightarrow Z^0$ production versus the rapidity y at $\sqrt{s} = 350, 500\text{GeV}$ (dashed, solid). . .	126
118	The parity violating asymmetry A_{LL}^{PV} versus the rapidity y for Z^0 production at $\sqrt{s} = 350, 500\text{GeV}$ (dashed, solid).	127
119	The parity violating asymmetry A_L^{PV} for $p^\uparrow n \rightarrow Z^0$ production versus the rapidity y at $\sqrt{s} = 350, 500\text{GeV}$ (dashed, solid). . .	128
120	Parity conserving double helicity asymmetry A_{LL}^{PC} for $pp \rightarrow W^\pm$ production versus the rapidity y at $\sqrt{s} = 350, 500\text{GeV}$ (dashed, solid)	129
121	Parity conserving double helicity asymmetry A_{LL}^{PC} for $pp \rightarrow Z^0$ production versus the rapidity y at $\sqrt{s} = 350, 500\text{GeV}$ (dashed, solid)	130
122	Parity conserving double helicity asymmetry A_{LL}^{PC} for $pn \rightarrow Z^0$ production versus the rapidity y at $\sqrt{s} = 350, 500\text{GeV}$ (dashed, solid)	131